UNIVERSITY OF OKLAHOMA

GRADUATE COLLEGE

# ACTIVE VIBRATION CONTROL SYSTEMS IN THE FREQUENCY AND SUB-BAND DOMAIN

A Dissertation

SUBMITTED TO THE GRADUATE FACULTY

in partial fulfillment of the requirement for the

degree of

Doctor of Philosophy

By

LONGJI WANG
Norman, Oklahoma
2001

Downloaded from SHAREOK. Persistent Handle URL: https://hdl.handle.net/11244/776

UMI Number: 3139176

INFORMATION TO USERS

The quality of this reproduction is dependent upon the quality of the copy submitted. Broken or indistinct print, colored or poor quality illustrations and photographs, print bleed-through, substandard margins, and improper alignment can adversely affect reproduction.

In the unlikely event that the author did not send a complete manuscript and there are missing pages, these will be noted. Also, if unauthorized copyright material had to be removed, a note will indicate the deletion.

UMI®

UMI Microform 3139176

Copyright 2004 by ProQuest Information and Learning Company.

All rights reserved. This microform edition is protected against unauthorized copying under Title 17, United States Code.

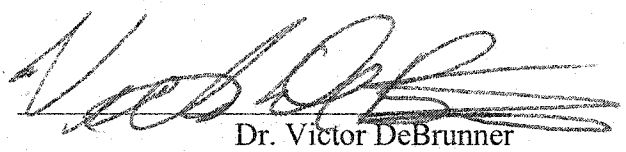
ProQuest Information and Learning Company
300 North Zeeb Road
P.O. Box 1346
Ann Arbor, MI 48106-1346

© Copyright by Longji Wang 2001
All Rights Reserved.

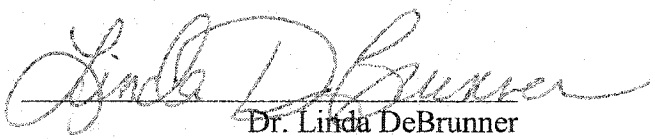
ACTIVE VIBRATION CONTROL SYSTEMS IN THE FREQUENCY AND SUB-BAND DOMAIN

A Dissertation APPROVED FOR THE
SCHOOL OF ELECTRICAL AND COMPUTER ENGINEERING

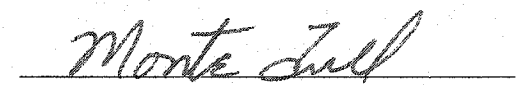
BY



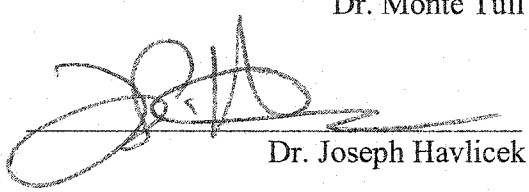
Dr. Victor DeBrunner



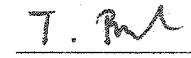
Dr. Linda DeBrunner



Dr. Monte Tull



Dr. Joseph Havlicek



Dr. Tomasz Przebinda

# Acknowledgements

This research was supported by Seagate Technology and Oklahoma Center for the Advancement Science and Technology (OCAST).

I am truly indebted to my advisors, Dr. Victor DeBrunner and Dr. Linda DeBrunner, for their guidance, support and encouragement. Words cannot adequately describe how much I appreciate their help throughout this work.

I would like to thank Dr. Monte Tull, Dr. Joseph Havlicek and Dr. Tomasz Przebinda for their assistance and time as members of my committee. Their insightful comments and suggestions have been most helpful.

I would also like to thank John Stricklin and the Acoustic Lab and LDV Lab at Seagate Technology for their assistance in the experiments.

I thank my parents for their sacrifice and support of my early education and their continued concern and confidence.

And most of all, I wish to express my deepest appreciation to my wife, Xiuhong, and my son, Xingyu, for their understanding and patience.

# Table of contents

Acknowledgements ..... iv

Table of contents ..... v

List of tables ..... viii

List of illustrations ..... ix

Abstract ..... xiv

**Chapter 1 Introduction** ..... **1**

**Chapter 2 Single-channel active control systems** ..... **5**

2.1 Adaptive feed-forward active control systems ..... 5

2.2 Adaptive feedback active control systems ..... 9

2.3 Identifying the secondary path transfer function ..... 13

2.4 Hybrid active control systems ..... 23

**Chapter 3 Implementing the FXLMS in the frequency domain** ..... **30**

3.1 Improving the convergence rate in the frequency domain ..... 31

3.1.1 Eigenvalue spread limits the convergence rate ..... 31

3.1.2 Deducing the eigenvalue spread in the frequency domain ..... 33

3.2 Simulations results of the frequency domain algorithm ..... 37

3.3 Reducing the constructive interference by selective adaptation ..... 45

**Chapter 4 Implementing the adaptive algorithm in sub-bands** ..... **53**

4.1 Sub-band adaptive filtering without signal path delay ..... 54

4.2 Increasing the convergence region of the step size ..... 61

4.3 Computer simulations ..... 64

4.3.1 Feed-forward active control system ..... 64

4.3.2 Feedback active control system with an AR(2) process ..... 70

4.3.3 Feedback active control system with the real vibration signals ..... 75

4.4 Combining the frequency domain technique with the sub-band architecture ... 80

4.5 Computational complexity ..... 84

**Chapter 5 Multiple-channel active control systems** ..... **87**

5.1 Multiple-channel FXLMS algorithm ..... 87

5.2 On-line identification of the multiple secondary paths ..... 91

5.3 Optimal performances of the multiple-channel control systems ..... 95

5.3.1 Regular control system ..... 95

5.3.2 Simplified control system ..... 100

5.3.3 Decentralized control system ..... 102

5.4 Computer simulations for a 2×2 system ..... 105

5.5 Improving the stability of the feedback control systems ..... 111

**Chapter 6 Summary and conclusion** ..... **115**

**References** ..... **120**

**Appendix A Experimental environment** ..... **129**

**Appendix B Frequency sampling method** ..... **133**

**Appendix C Proof of the non-equivalency of the direct swap** ..... **136**

**Vita** ..... **138**

# List of tables

Table 4.1 Comparison of the computational complexity of different algorithms ..... 86

Table A.1 Technical specifications of the M44 ..... 129

Table A.2 Technical specifications of the A4D4 ..... 130

Table A.3 Main features of the PCB 353B15 accelerometer ..... 131

Table A.4 Main features of PCB 713A01 patch actuator ..... 131

Table A.5 Specifications of the 482A04 line power supply ..... 132

Table A.6 Specifications of the 790A01 power amplifier ..... 132

# List of illustrations


Figure 2.1 Single-channel feed-forward active noise control system in duct. ..... 6

Figure 2.2 Block diagram of the feed-forward active control system. ..... 7

Figure 2.3 Block diagram of the feed-forward active control system using the FXLMS algorithm. ..... 9

Figure 2.4 Block diagram of a single-channel feedback control system. ..... 10

Figure 2.5 Broadband adaptive feedback active control system. ..... 12

Figure 2.6 Adaptive feedback control system takes the form of adaptive feed-forward control system if $\hat{S}(z)=S(z)$. ..... 12

Figure 2.7 Adaptive feedback control system with on-line $S(z)$ identification. ..... 15

Figure 2.8 Schematic diagram of the control system for the HDD. ..... 16

Figure 2.9 System setup for the vibration control of the HDD. ..... 16

Figure 2.10 Performance of the active vibration control in real time. ..... 17

Figure 2.11 Simulation result of the vibration reduction at a 16 *kHz* sampling rate. .... 19

Figure 2.12 Influences of the white noise levels on the performance. ..... 20

Figure 2.13 Crosscorrelation between the residual error and the white noises with different variances. ..... 21

Figure 2.14 Hybrid active control scheme using the FXLMS algorithm. ..... 25

Figure 2.15 Power spectral densities of the original vibration. ..... 26

Figure 2.16 Power spectral densities of the residual error signals. ..... 27

Figure 2.17 Power spectral densities of the residual error signals where all the original

vibration can be observed by the reference sensor. ..... 29

Figure 3.1 Block diagram of adaptive filtering in the frequency domain. ..... 35

Figure 3.2 Learning curves of the time domain LMS and the frequency domain LMS (eigenvalue spread = 1.22). ..... 39

Figure 3.3 Learning curves of the time domain LMS and the frequency domain LMS (eigenvalue spread = 3). ..... 40

Figure 3.4 Learning curves of the time domain LMS and the frequency domain LMS (eigenvalue spread = 10). ..... 41

Figure 3.5 Learning curves of the DWT-LMS with different wavelets. ..... 42

Figure 3.6 Vibration reduction in real time with the frequency domain algorithm. .... 44

Figure 3.7 Simulation result of vibration reduction with the time domain FXLMS and the frequency domain FXLMS. ..... 46

Figure 3.8 Selective adaptation of the adaptive algorithm in the frequency domain. ... 48

Figure 3.9 Effect of alleviating the constructive interference by the selective adaptation for the real HDD vibration signal. ..... 50

Figure 3.10 Effect of alleviating the constructive interference by the selective adaptation for an AR(2) process. ..... 51

Figure 3.11 Magnitude response of the $8^{th}$ transfer function of a 10-point DCT. .... 52

Figure 3.12 Magnitude response of the $8^{th}$ transfer function of a 16-point DCT. ..... 52

Figure 4.1 Block diagram of the active control

(a) feed-forward ..... 55

(b) feedback ..... 55

(c) unified diagram from the viewpoint of adaptive filtering. ..... 55

Figure 4.2 Sub-band adaptive filter structure used in the system identification or echo cancellation. ..... 57

Figure 4.3 Sub-band adaptive filter architecture without signal path delay. ..... 58

Figure 4.4 Trajectories of $\boldsymbol{w}$ using the FXLMS in full-band and in sub-band. ..... 66

Figure 4.5 Trajectories of $\boldsymbol{w}$ using the sub-band FXLMS without delay compensation and with delay compensation. ..... 66

Figure 4.6 Trajectories of the magnitude of the full-band error |e(n)| and the filter coefficients using the full-band FXLMS. ..... 68

Figure 4.7 Trajectories of the magnitude of the full-band error |e(n)| and the filter coefficients using the sub-band FXLMS (no delay compensation). ..... 68

Figure 4.8 Trajectories of the magnitude of the full-band error |e(n)| and the filter coefficients using the sub-band FXLMS (partial delay compensation). ... 69

Figure 4.9 Trajectories of the magnitude of the full-band error |e(n)| and the filter coefficients using the sub-band FXLMS (full delay compensation). ..... 69

Figure 4.10 Learning curves of the normalized FXLMS in full-band and in sub-band. 71

Figure 4.11 Learning curves of the FXLMS in full-band and in sub-band. ..... 72

Figure 4.12 Learning curves of the FXLMS in sub-band with delay compensation. .... 73

Figure 4.13 Learning curves of the FXLMS in sub-band without delay compensation and with delay compensation. ..... 74

Figure 4.14 Simulation result of vibration reduction using the full-band FXLMS and sub-band FXLMS. ..... 76

Figure 4.15 Magnitude responses of the *AR(N)* processes resulting from the controller vector when more weight is placed to the low frequency band. ..... 78

Figure 4.16 Magnitude responses of the *AR(N)* processes resulting from the controller vector when more weight is placed to the high frequency band. ..... 79

Figure 4.17 Simulation result of the sub-band FXLMS algorithm. ..... 81

Figure 4.18 Block diagram of the combined structure. ..... 82

Figure 4.19 Simulation result of the combined structure with the selective adaptation. 83

Figure 4.20 Learning curves of the combined frequency domain/sub-band LMS. .... 85

Figure 5.1 2×2 adaptive feedback active control system. ..... 91

Figure 5.2 On-line identification using one random noise generator. ..... 93

Figure 5.3 On-line identification using two random noise generators. ..... 94

Figure 5.4 Block diagram of the multiple-channel feedback control system. ..... 96

Figure 5.5 Simplified multiple-channel feedback control system. ..... 101

Figure 5.6 Simplified 2×2 adaptive feedback active control system. ..... 106

Figure 5.7 The averaged square errors achieved by the regular control system with $s_{11} = s_{22} = [0, \quad 0.5, \quad -0.5]^T$. ..... 107

Figure 5.8 The averaged square errors achieved by the simplified control system with $s_{11} = s_{22} = [0, \quad 0.5, \quad -0.5]^T$. ..... 107

Figure 5.9 The averaged square errors achieved by the regular control system with $s_{11} = s_{22} = [0, \quad 0.5, \quad 0.5]^T$. ..... 110

Figure 5.10 The averaged square errors achieved by the fully decentralized control system with $s_{11} = s_{22} = [0, \quad 0.5, \quad 0.5]^T$. ..... 110

Figure 5.11 The square errors achieved by the fully decentralized control system with $s_{12} = s_{21} = [0, \quad 0.45, \quad 0.45]^T$ and $s_{12} = s_{21} = [0, \quad 0.05, \quad 0.05]^T$ .. 111

Figure 5.12 Stability improvement of the decentralized system. ..... 114

Figure 5.13 The square error using the old cost function and the new cost function with $\boldsymbol{s}_{11} = \boldsymbol{s}_{22} = [0, \quad 0.5, \quad -0.5]^T$ and $\boldsymbol{s}_{12} = \boldsymbol{s}_{21} = [0, \quad 0.2, \quad 0.2]^T$ . ..... 114

# Abstract

Active noise and vibration control has been the subject of intense study in the last two decades due to the increased speed in digital signal processors and the technological development and manufacture of smart materials. This dissertation analyzes an active control system using adaptive digital signal processing techniques and applies it to the vibration reduction of hard disk drives (HDD). Specifically, this work focuses on the implementation of the adaptive algorithm in the frequency and sub-band domains for performance improvement.

In this dissertation, selective adaptation in the frequency domain is proposed to alleviate the constructive interference associated with a feedback active control system. A new sub-band adaptive filter architecture without a signal path delay is proposed, and the associated adaptive algorithm is derived. This delayless sub-band algorithm can be applied to the active control systems to improve the convergence rate and trade-off the performance from the various sub-bands. The resulting side effect of the error path delay of the analysis filter bank is analyzed, and two compensation methods are proposed to increase the performance. The frequency domain method and the sub-band decomposition technique are then combined to improve the overall performance. The single-channel active control system is extended to the multiple-channel active control system to reduce the vibration of complex mechanical structure. The optimal performances of three variants of the feedback control system have been derived in terms of the correlation coefficients of the primary disturbances and the impulse responses of the secondary paths. Real time and simulation results are performed to verify the efficiency of the proposed algorithms and techniques.

# Chapter 1

# Introduction

Sound and vibration have conventionally been controlled by passive methods that involve absorbing the disturbance or blocking its transmission. These passive methods generally do not work well at low frequencies. This is because at these low frequencies the wavelengths of the disturbance are large compared to the thickness of a typical acoustic absorber or structure. Paul Lueg first described the idea of active control in 1936 [1]. The basic idea of active control is to use a number of controllable "secondary" sources to produce an acoustic wave or vibration that is exactly out of phase with the primary disturbance and superimpose them, thereby resulting in destructive interference. Although the principle of active control dates back to the 1930's, and manually adaptive analogue active control systems were developed in 1950's [2], the modern era of active control was spurred by the availability of high speed digital signal processors which allow adaptive digital controllers to be implemented at a relatively low cost. Active noise and vibration control have been the subject of intense study and considerable research activity in the last two decades [3]-[8]. These methods have already found commercial application in active headsets and broadband sound control in ducts. With the technological development and manufacture of smart materials such as piezoceramic actuators and sensors, active vibration control also has some significant potential application in other areas. Active noise control and active vibration control share almost the same principles, algorithms, system structures and other main issues.

One of the main differences is that they generally use different sensors and actuators. Microphones and loud speakers are the common sensors and actuators for active noise control while smart materials are used for active vibration control. This dissertation aims to actively reduce the vibration of hard disk drive (HDD) and discusses the potential problems in such a system, as well as their possible solutions. Specifically, this dissertation proposes the "selective adaptation in the frequency domain" method to alleviate any constructive interference and a "sub-band adaptive algorithm" for active control systems that avoids unnecessary signal path delay. The proposed sub-band algorithm has the flexibility to trade-off the performance from the various sub-bands. It also achieves a better convergence compared to the full-band counterpart. The organization of this dissertation is as follows.

Chapter 2 reviews the basic technologies of single-channel active control systems. It introduces the principles and performance limitations of the feed-forward active control system and the feedback active control system. Next, the on-line identification of the secondary path transfer function and the effect of the estimate error are analyzed. These technologies are then applied to reduce the vibration of the HDD at a single position. A method that combines the feed-forward and feedback system to form a hybrid active control system is discussed last. Real-time and simulation results are presented throughout the discussion.

Chapter 3 discusses the implementation of the adaptive algorithm in the frequency domain to alleviate the constructive interference that might occur in the feedback active control systems. Another purpose of implementing the algorithm in the frequency domain is to increase the convergence rate. Theoretical analysis is performed to show

how the eigenvalue spread of the signal correlation limits the convergence rate and why the frequency domain algorithm can improve the convergence rate by reducing the eigenvalue spread of the input autocorrelation matrix. Simulation and real time results using the Discrete Cosine Transform (DCT) and the Discrete Wavelet Transform (DWT) are provided to demonstrate the efficiency of the frequency domain methods.

Chapter 4 contains a discussion of methods that implement the least-mean-square (LMS) algorithm in sub-band architecture. Since the ideal signal in the active control system is not directly available and since the active control system generally cannot tolerate extra delay along the signal path, the sub-band structure used in the system identification, or in echo cancellation, cannot be directly applied to the active control system. Instead, a new delayless sub-band filter architecture is derived in this chapter. The error path delay resulting from the analysis filter band will decrease the convergence performance in general. Methods that restore the convergence performance using error path delay compensation are proposed. A new structure of combining the frequency domain method and the sub-band decomposition technique is proposed and demonstrated in the last part of this chapter.

Chapter 5 extends the single-channel feedback control system to the multiple-channel feedback control system to reduce the vibration of complex mechanical structures and/or the acoustic noise inside the enclosures caused by the vibrations. The LMS algorithm for the multiple-channel system is developed. On-line identifications of the multiple secondary path transfer functions are discussed in detail. This chapter also derives the optimal performance of a multiple-channel feedback control system in terms of the correlation coefficients of the primary disturbances and the impulse responses of

the secondary paths. Three variants of the feedback control systems have been considered. Performance and robustness are two important aspects of the feedback control system. How to improve the stability of the feedback control system by penalizing the control effort in the cost function is discussed with the examples.

Chapter 6 consists of summary and conclusions followed by appendix A and B. Appendix A introduces the experimental environment of the active vibration control system for the HDD. Appendix B derives the frequency sampling structure to efficiently implement the discrete cosine transform.

# Chapter 2

# Single-channel active control systems

This chapter reviews the basic technologies of a single-channel active control system that has a single error sensor and a single secondary source. Active control systems can be classified as feed-forward active control systems and feedback active control systems depending on whether a reference signal that provides "early" information about the primary disturbance is available. Section 2.1 and Section 2.2 will discuss these two systems respectively. The existence of the secondary path transfer function in active control systems has a direct effect on the adaptive algorithm and the overall performance. Section 2.3 focuses on the identification of the secondary path transfer function, as well as related issues. Section 2.4 considers the combination of a feed-forward control system with a feedback control system for performance improvement. Real time and simulation results accompany the discussion.

## 2.1 Adaptive feed-forward active control systems

A single-channel feed-forward active noise control (ANC) system shown in Figure 2.1 is used to explain the principle of the feed-forward active control system. The basic ANC system shown in Figure 2.1 can be described in a system identification framework. Consider a noise source at the end of a duct. The undesired noise is measured by a reference microphone placed upstream from the point to be controlled. The reference signal $x(n)$ is filtered through an adaptive filter and used to drive a

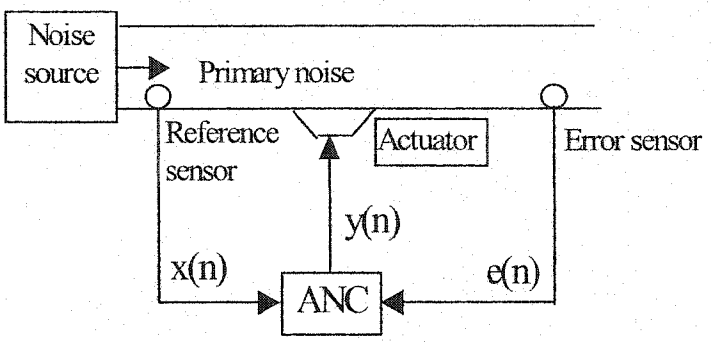



Figure 2.1 Single-channel feed-forward active noise control system in duct [14].

secondary source such as a loudspeaker to cancel the noise in the duct. The reference signal *x(n)* provides "early" information about the primary noise before it reaches the canceling loudspeaker. The residual noise is detected by an error sensor and is used to update the coefficients of the adaptive filter to minimize the residual noise. This active noise control system can be cast in an adaptive filtering problem shown in Figure 2.2. The control signal *y(n)* must be produced from the electrical output signal using a loudspeaker. Also, an electrical error signal must be obtained from the residual acoustic noise using an error microphone. Therefore, it is necessary to include the transfer function from the adaptive filter output to the summing junction, *S(z)*, and the transfer function from the summing junction to the error signal, *R(z)*, in the adaptive filtering problem in Figure 2.2. For the example of noise reduction in duct shown in Figure 2.1, *S(z)* generally represents the frequency responses of the D/A converter, the power amplifier, the actuator, and the acoustic path from the actuator to the summing junction. *R(z)* represents the frequency responses of the acoustic path from the summing junction to the error sensor, the preamplifier/signal conditional, and the A/D converter.

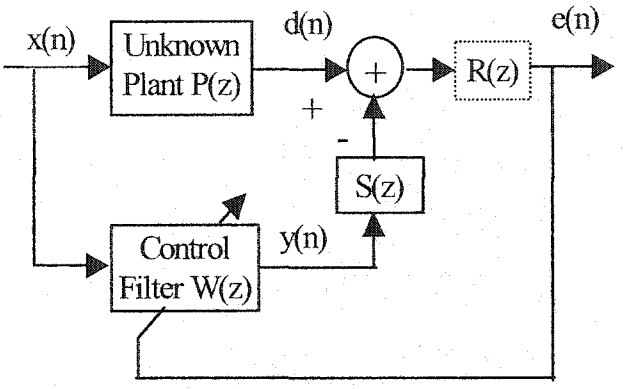



Figure 2.2 Block diagram of the feed-forward active control system.

It can be seen from Figure 2.2 that the Z-transform of the error signal is

$$E(z)=X(z)[P(z)-W(z)S(z)]R(z) \tag{2.1}$$

Therefore, the purpose of the control filter *W(z)* is to model the plant *P(z)* and invert the secondary path transfer function *S(z)* at the same time. When *P(z)* and/or *S(z)* are time-varying, we need *W(z)* to be adaptive. The overall limiting causality constraint in the broadband feed-forward control system is that the delay of the control path *W(z)S(z)* must be less than the delay of the primary path *P(z)*. When this criterion is met, the performance of the feed-forward control system primarily depends on the coherency of the reference signal *x(n)* and the primary disturbance at the summing point, *d(n)*. This is a measure of the noise and the relative linearity of *x(n)* and *d(n)*, or how well the physical plant can be modeled by a linear filter.

Since both the primary path and the secondary path have *R(z)* in common, it is convenient to absorb this term into the model *P(z)* as well as into the secondary path *S(z)*. Doing so is equivalent to redefining the summing junction to be in the electrical domain rather than in the acoustic domain. We call this new *S(z)* the secondary path

transfer function and it is this transfer function that needs to be identified in the active control system.

The LMS algorithm is a widely used adaptive algorithm because of its computational efficiency and simplicity. Since the secondary path transfer function *S(z)* follows the control filter *W(z),* the conventional LMS algorithm must be modified to ensure convergence. Otherwise, the result is likely to be an unstable system. This instability arises because the signal from the control filter *W(z)* suffers a phase shift in passing through the secondary path *S(z)*. The instantaneous measurement of the gradient of the mean square error with respect to the coefficient vector, $x(n)e(n)$, is thus no longer an unbiased estimate of the true gradient. To solve this problem, the so-called filter-X LMS (FXLMS) was proposed by Morgan [9] in 1980 and independently by Widrow [10] in 1981. The FXLMS algorithm introduces a similar phase shift into the reference signal path before the gradient is formed. This is achieved by an electrical filter $\hat{S}(z)$ which models the response of the secondary path *S(z)* to generate a filtered reference signal $x'(n)$. The filtered reference signal is then multiplied by the error signal to form the gradient estimate as shown in Figure 2.3. The control filter *W(z)* is then updated as

$$w(n+1) = w(n) + \mu x'(n)e(n), \tag{2.2}$$

$$x'(n) = \hat{s}(n) * x(n) \tag{2.3}$$

and

$$e(n) = d(n) - s(n) * [w^T(n)x(n)] \tag{2.4}$$

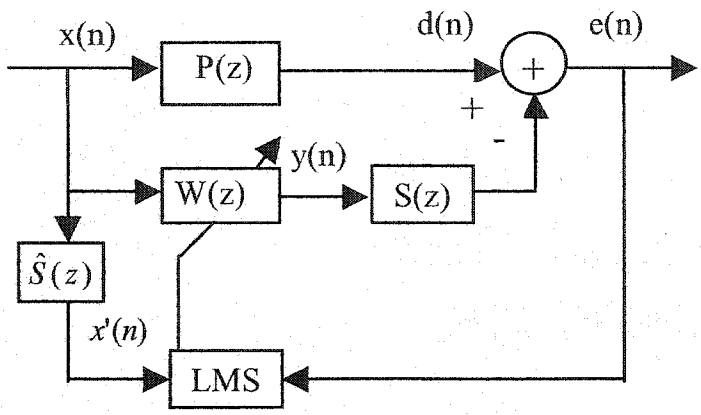



Figure 2.3 Block diagram of the feed-forward active control system using the FXLMS algorithm.

where $\hat{s}(n)$ is the estimated impulse response of the secondary path filter, $\hat{S}(z)$, and $*$ stands for the convolution operation.

## 2.2 Adaptive feedback active control systems

A feed-forward active control system requires a reference signal to provide advance information about the primary disturbance. In some situations, it is not practical to sense or internally generate a coherent reference signal, such as in the case of vibration reduction for the HDD, where only the residual error signal is available. Consequently, this kind of active control system falls into the framework of the conventional feedback control scheme (refer to Figure 2.4). The transfer function from the primary disturbance *D(z)* to the residual error E(z) is

$$\frac{E(z)}{D(z)} = \frac{1}{1 + W(z)S(z)}. \tag{2.5}$$

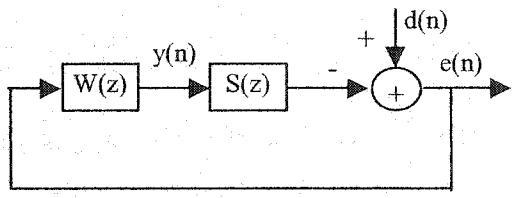



Figure 2.4 Block diagram of a single-channel feedback control system.

The response of *S(z)* can introduce a considerable phase shift that increases with frequency. As the phase shift in the secondary path approaches 180°, the desired negative feedback becomes positive feedback, and the control system can become unstable. If we define

$$W(e^{j\omega})S(e^{j\omega}) = G(e^{j\omega})e^{j\phi(\omega)} \tag{2.6}$$

where $G(e^{j\omega}) = \left|W(e^{j\omega})S(e^{j\omega})\right|$, then the design of a feedback active control system is to find a $W(e^{j\omega})$, such that the net gain $G(e^{j\omega})$ is maximized when the phase shift $\phi(\omega)$ is in the region

$$-180° < \phi(\omega) < 180° \tag{2.7}$$

for a given secondary path $S(e^{j\omega})$. When $S(e^{j\omega})$ and $D(e^{j\omega})$ are time-varying, the control systems need to be adaptive. The adaptive algorithms require a reference signal and a residual error signal for updating the weights. In the conventional feedback control systems shown in Figure 2.4, there is no reference signal and the primary disturbance *d(n)* is also not available during the operation of active control since it is intended to be canceled by the secondary source. Although *d(n)* is not directly available in feedback control systems, it can be synthesized or regenerated based on the residual

error *e(n)*, the control signal *y(n)* and knowledge of *S(z)*. This was first suggested by Newton in [46] and Eriksson [11] applied it to the adaptive feedback active control system, which estimates the primary disturbance *d(n)* and then uses it as the reference signal for the adaptive algorithm. This is also called the Youla transform in [6]. When *S(z)* is identified as $\hat{S}(z)$, the primary disturbance *d(n)* can be regenerated as

$$\hat{D}(z) = E(z) + Y(z)\hat{S}(z) \tag{2.8}$$

Using $\hat{d}(n)$ as the reference signal, a complete adaptive feedback active control system can be viewed as the adaptive feed-forward system that is illustrated in Figure 2.5.

If the secondary path transfer function can be identified accurately, *i.e.*, $\hat{S}(z)=S(z)$, then *x(n)=d(n)*. Consequently, the adaptive feedback control system shown in Figure 2.5 can be transformed into an equivalent adaptive feed-forward control system as shown in Figure 2.6. The overall transfer function from *d(n)* to *e(n)* is

$$\frac{E(z)}{D(z)} = 1 - W(z)S(z) \tag{2.9}$$

and the purpose of the adaptive filter, *W(z)*, is to try to invert *S(z)*.

If the step size of the LMS algorithm is small, the adaptive filter *W(z)* can be commuted with *S(z)* [12]. If we further assume that *S(z)* can be modeled as a pure delay, then the adaptive feedback control system of Figure 2.6 is identical to the standard adaptive forward prediction-error filter. Then, the performance of the adaptive feedback control system depends on the predictability of the primary disturbance *d(n)*. For a stationary discrete-time stochastic process, the adaptive forward prediction-error filter is

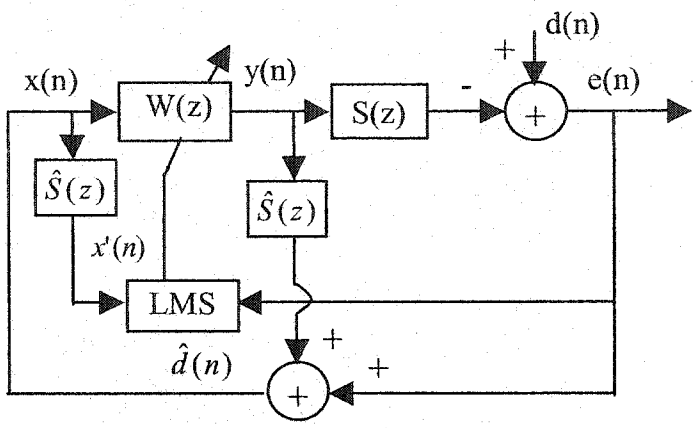



Figure 2.5 Broadband adaptive feedback active control system using the FXLMS algorithm.

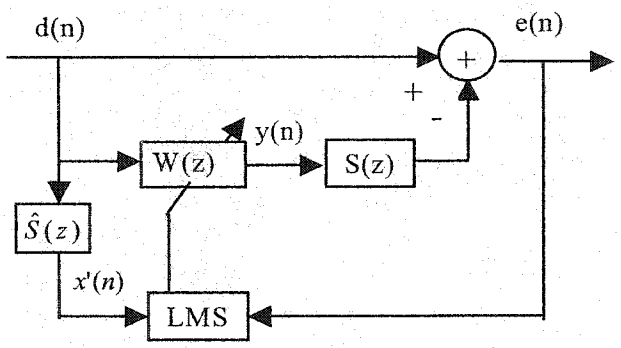



Figure 2.6 Adaptive feedback control system takes the form of adaptive feed-forward control system if $\hat{S}(z)=S(z)$.

intimately related to the autoregressive modeling of the process [13]. For a predictor of order $N$, the filter weight $w_k$ is related to the AR parameter $a_k$ as follows:

$$w_k = -a_k, k = 1,2,...,N. \tag{2.10}$$

In other words, what the adaptive feedback active control systems have reduced is that part of the primary disturbance that can be modeled as an *AR(N)* process. In the general

case where *S(z)* is not a pure delay and $S(z) \neq \hat{S}(z)$, the performance of the adaptive feedback control system depends on the accuracy of representing *S(z)* by $\hat{S}(z)$ and the predictability of the primary disturbance filtered by the estimated secondary path transfer function, $\hat{S}(z)$.

## 2.3 Identifying the secondary path transfer function

It can be seen from the previous discussion that the secondary path transfer function must be identified. For adaptive feed-forward control systems, we need to place $\hat{S}(z)$ into the weight updating path to compensate for *S(z)*. Then, the FXLMS replaces the LMS algorithm to ensure that the compensated system is stable. For adaptive feedback control systems, $\hat{S}(z)$ is required to regenerate the primary disturbance and to compensate for *S(z)* during the weight updating.

Estimation of *S(z)* can be performed either off-line or on-line, depending on whether *S(z)* is time invariant. The off-line identification of *S(z)* can be performed using a separate LMS adaptation process during an initial training stage. Because the *S(z)* in our HDD case is time-varying (probably due to changing temperatures and aging), we need on-line identification [14]. On-line identification of *S(z)* means the coefficients of the digital filter $\hat{S}(z)$ are adjusted on-line by one more adaptation processes to continuously model the secondary path transfer function *S(z)* during the active control.

There are two important, but mutually exclusive, requirements associated with the on-line secondary path modeling. The first is that *S(z)* should be estimated accurately regardless of the controller transfer function *W(z)*. This independence property will

ensure that the overall active control system is robust. In favor of the independent identification of *S(z)*, it would be preferable to use a separate excitation signal to drive *S(z)*. The second requirement is that the on-line identification should not intrude on the operation of the active control system. In favor of the intrusion requirement, it would be preferable to identify *S(z)* using the control signal *y(n)* which already exists in the system. If *y(n)* serves as the excitation signal for the modeling of *S(z)*, a signal-dependent solution results, and so *S(z)* is then biased [14]. To drive *S(z)* separately, we need an additional signal. White noise is an ideal broadband excitation signal, because it has a constant spectral density at all frequencies. Figure 2.7 shows the adaptive feedback control system with on-line *S(z)* identification using the additive white noise.

With the technologies discussed, we may implement a single-channel feedback control system for the HDD. Figure 2.8 gives the schematic diagram of the connection. Figure 2.9 is a photograph of the experimental setup for the single-channel control system. A TMS320C44 based DSP board is used as the controller in the experimental system, and an A4D4 Omnibus module is used to provide the A/D and D/A channels. Appendix A describes the details of the experimental environment.

The adaptive active control system requires the use of a sample-by-sample processing mode. Only a 10 *kHz* sampling rate can be achieved under the M44/A4D4 environment for an $8^{th}$ order controller and secondary path filter. Figure 2.10 shows the power spectral densities (PSD) of the original vibration (solid line) and the vibration after the active control is on (the dotted line) at the point where the error sensor is located. It can be seen that more than 5 *dB* of reduction is achieved around the 600 *Hz* and 800 *Hz* modes. It is mentioned in the previous section that the performance of the

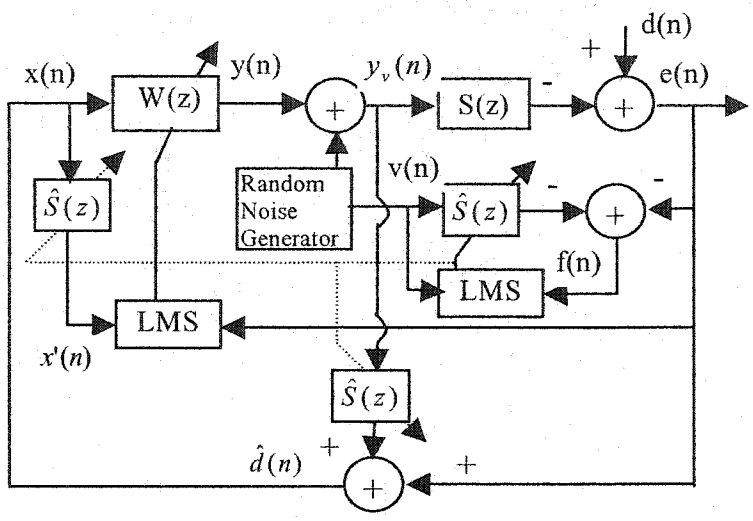



Figure 2.7 Adaptive feedback control system with on-line *S(z)* identification using the additive white noise as the excitation signal.

feedback active control system depends on the accuracy of representing *S(z)* by $\hat{S}(z)$ and the predictability of the primary disturbance filtered by the estimated secondary path transfer function, $\hat{S}(z)$. Specifically, the performance is determined by the following factors:

- The mode shape of the original vibration
- The frequency response of the secondary path transfer function
- The sampling rate
- Order of the controller
- Estimation error of representing *S(z)* by $\hat{S}(z)$
- The variance of the white noise used for on-line identification

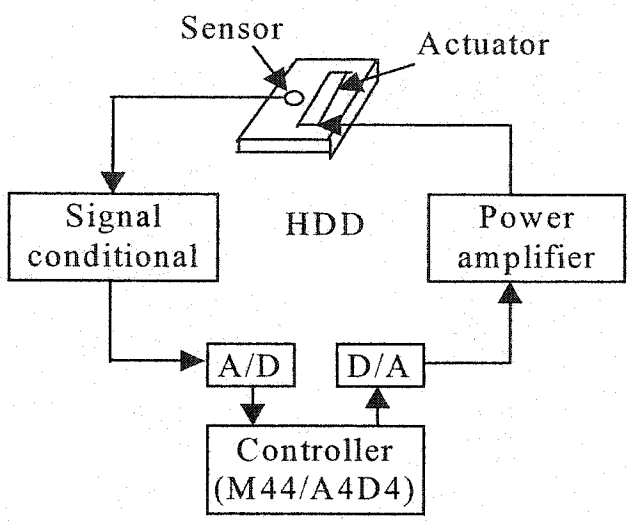



Figure 2.8 Schematic diagram of the single-channel feedback active control system for the HDD.

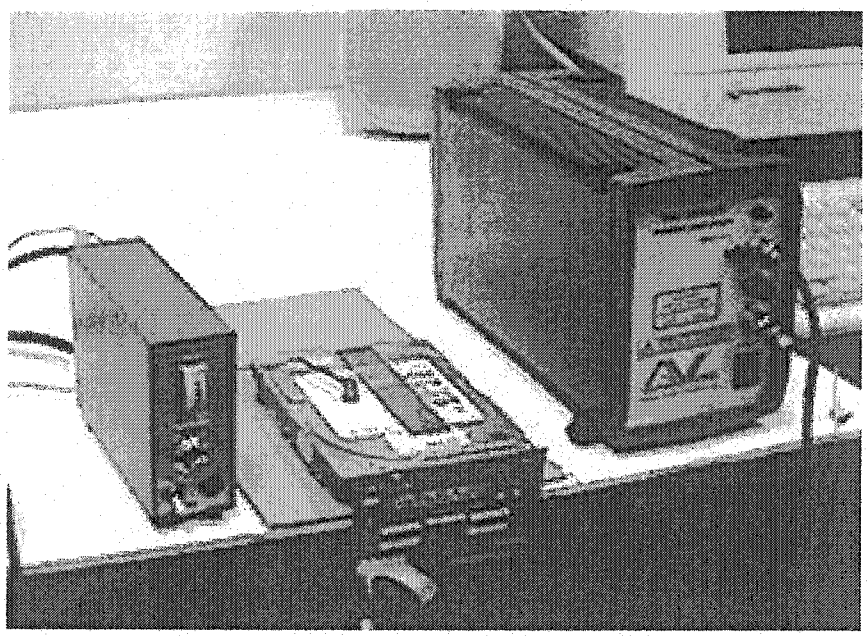


Figure 2.9 Single-channel feedback active control system setup for the vibration control of the HDD.

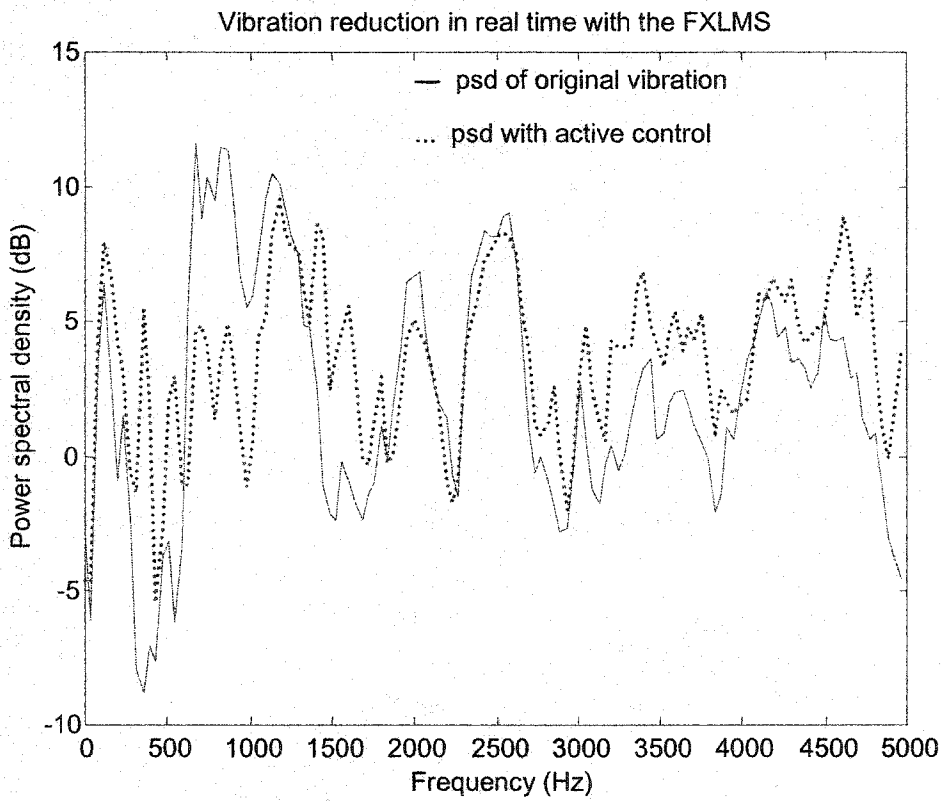



Figure 2.10 Performance of the active vibration control in real time using the FXLMS algorithm with an $8^{th}$-order controller and secondary path filter.

We cannot change the mode shape and the secondary path transfer function at will, but they are closely related to the sampling rate. Since the original vibration of the HDD has frequency components as high as 10 *kHz*, the aliasing resulting from the low sampling rate makes the sampled vibration more like white noise, hence degrading the performance of the prediction. Therefore, increasing the sampling rate will improve the performance of the feedback active control system. To look at the impact of the sampling rate on the performance, we sampled the same vibration at 16 *kHz* using the hardware trigger mode (not sample-by-sample processing). The solid line in Figure 2.11 shows the PSD of the original vibration. It can be seen that the vibration is less white at this high sampling rate, hence it can be better predicted. The dotted line is the simulated result of the PSD using active control under the same secondary path transfer function and the same controller order. This simulation demonstrates that a much better vibration reduction could be achieved if the sampling rate were to be increased.

The additive white noise used for on-line identification has a direct impact on the performance because it appears in the residual error. Hence, it degrades the overall performance. Theoretically, this intrusion can be made arbitrarily small by choosing a low-level excitation signal, but a very low-level white noise compared to the primary disturbance will result in the divergence of $\hat{S}(z)$ due to finite-word length effects and measurement error. In practice, a moderate level of white noise is required, which slightly increases the residual error *e(n)*. To see this experimentally, Figure 2.12 shows the impacts of different white noise levels on the performance of the active control system using the FXLMS algorithm, where the original vibration is in the range of –10 *mV* to 10 *mV*, and the white noise is in the range of –0.25 *mV* to 0.25 *mV*, -1 *mV* to 1

*mV*, -4 *mV* to 4 *mV*, respectively. Figure 2.13 shows the crosscorrelation between the residual error and the white noise with different levels. It can be seen that the white noise with a level 10 *dB* down from the original disturbance, *i.e.*, in the range of –1 *mV* to 1 *mV*, does not degrade the performance very much while it is quite distinguishable in the residual error.

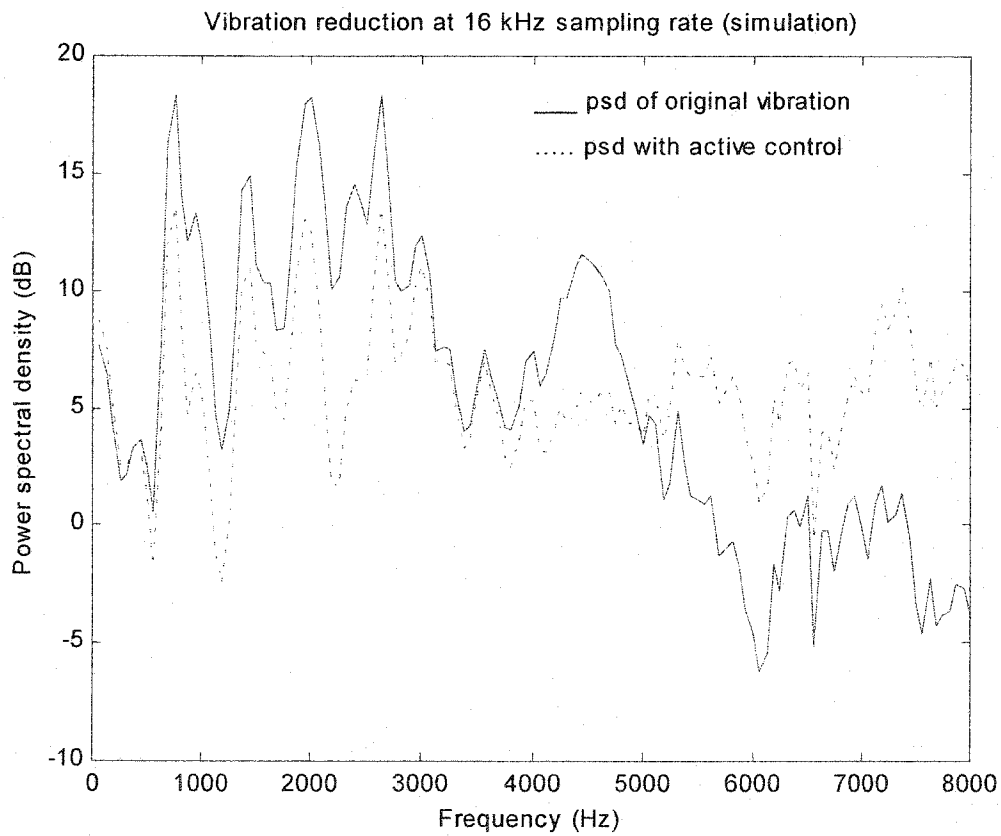



Figure 2.11 Simulation result of the vibration reduction at a 16 *kHz* sampling rate.

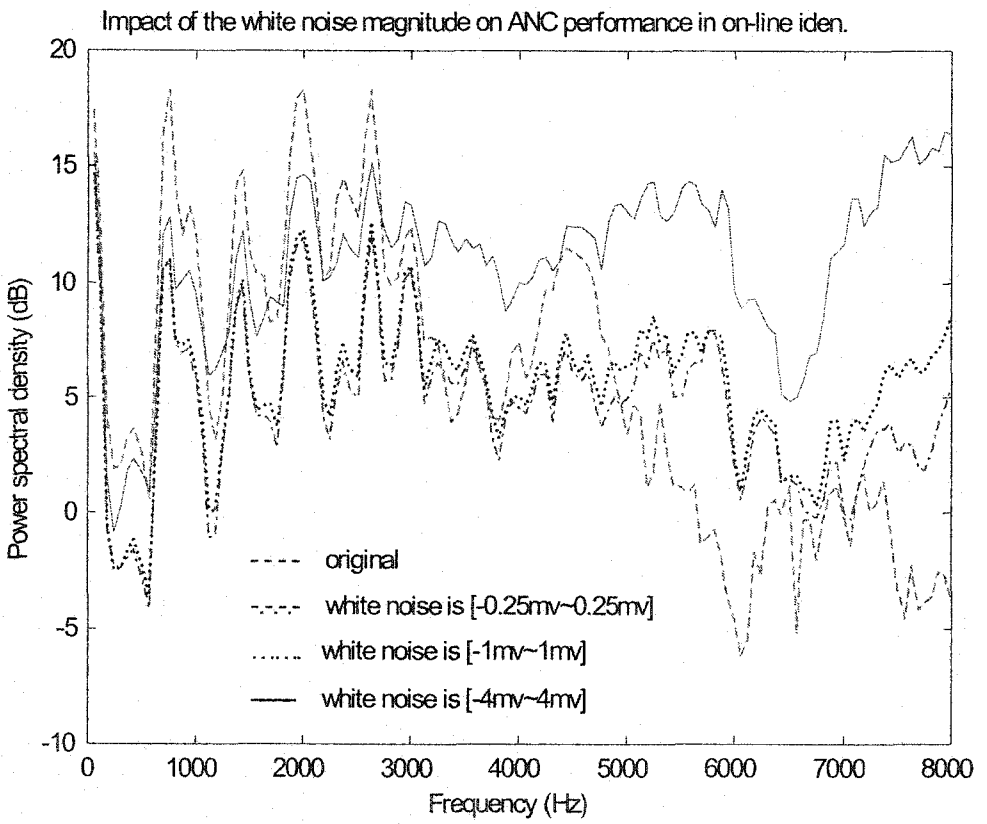



Figure 2.12 Influences of the white noise levels on the performance of the active control.

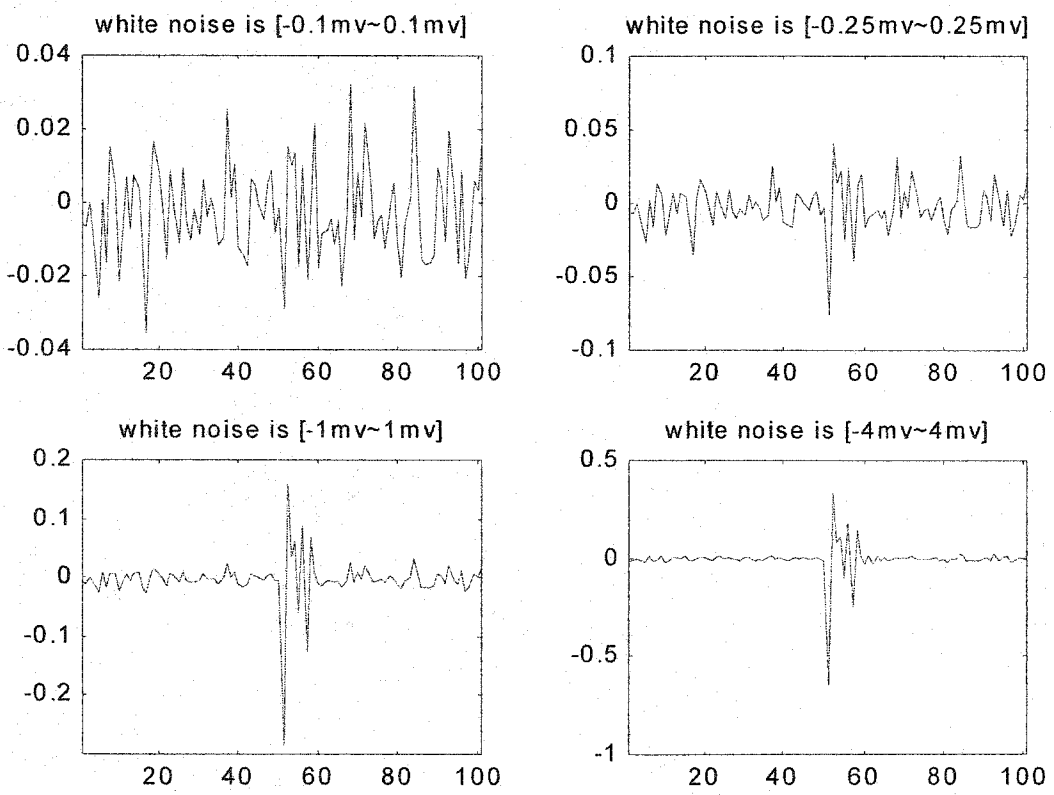



Figure 2.13 Crosscorrelation between the residual error and the white noises with different variances.

The estimation error of *S(z)* affects the maximum stable value of the step size of the FXLMS algorithm. This can be shown from the FXLMS algorithm itself [14]. Taking the expected value of Equation (2.2) results in the mean adaptive weight difference equation

$$\overline{\boldsymbol{w}}(n+1) = (\boldsymbol{I} - \mu\boldsymbol{R})\overline{\boldsymbol{w}}(n) + \mu\boldsymbol{p}, \tag{2.11}$$

where

$$\boldsymbol{R} \equiv E[\boldsymbol{x}'(n)\boldsymbol{x}'^{T}(n)] \tag{2.12}$$

is the filtered reference autocorrelation matrix, and

$$\boldsymbol{p} \equiv E[d(n)\boldsymbol{x}'(n)]. \tag{2.13}$$

If $\hat{S}(Z) \neq S(Z)$, then the mean weight vector difference equation, Equation (2.11), is modified to

$$\overline{\boldsymbol{w}}(n+1) = [\boldsymbol{I} - \mu(\boldsymbol{R} - \widetilde{\boldsymbol{R}})]\overline{\boldsymbol{w}}(n) + \mu\boldsymbol{p} \tag{2.14}$$

where

$$\widetilde{\boldsymbol{R}} \equiv E[\boldsymbol{x}'(n)\widetilde{\boldsymbol{x}}^{T}(n)] \tag{2.15}$$

is the correlation matrix between the filtered reference signal vector $\boldsymbol{x}'(n)$ defined in Equation (2.3) and the differential filtered reference signal vector

$$\widetilde{\boldsymbol{x}}(n) \equiv \widetilde{s}(n) * \boldsymbol{x}(n), \tag{2.16}$$

where

$$\widetilde{s}(n) \equiv \hat{s}(n) - s(n) \tag{2.17}$$

is the difference between the estimated and actual secondary-path filter. If $\hat{s}(n) = s(n)$, $\widetilde{\boldsymbol{R}} = \boldsymbol{0}$ and the original FXLMS stability bounds apply. However, errors in the estimation of *s(n)* will alter the eigenmodes of Equation (2.14), thus affecting the

stability bound of the step size $\mu$. Equations (2.15)-(2.17) show that any error in the estimation of the magnitude of the transfer function will proportionately change the magnitude of the autocorrelation matrix, and hence will simply scale the ideal stability bound accordingly. It has been shown [15] that stability is assured for phase errors θ in the range of $-90^\circ \le \theta \le 90^\circ$. However, there is no simple relationship between the modeling error and stability within this stable region.

A final issue associated with the on-line identification using a separate white noise is its slow convergence rate. It is derived in [14] that it would take 100 times longer for $\hat{S}(z)$ to converge in the on-line method as it would take to converge using the off-line one. Therefore, some supplemental measures, such as identifying *S(z)* off-line first and using the result as the initial value for on-line identification might be required for some applications where convergence speed is important.

## 2.4 Hybrid active control systems

It was mentioned in Section 2.2 that the feedback active control system can only cancel the part of the primary disturbance that can be predicted after it has been filtered by the secondary path transfer function. On the other hand, the feed-forward active control system can only cancel the part of the primary disturbance that is correlated with the reference signal. In some applications only part of the disturbance is correlated with the reference signal. Then, only this part can be reduced by the feed-forward active control system. In these situations, we can combine the feedback control system and the feed-forward control system to get a "hybrid algorithm" with improved performance.

This section describes the performance of the "hybrid" algorithm compared with the pure feed-forward algorithm and the feedback algorithm.

Figure 2.14 illustrates the hybrid active control system that is composed of a feed-forward system using the FXLMS algorithm and a feedback system using the FXLMS algorithm. The secondary signal (or control signal) *y(n)* is generated using the output of both the feed-forward controller *F(z)* and the feedback controller *B(z)*. The combined controller *W(z)* has two reference signals: the reference signal *x(n)* and the estimated primary disturbance $\hat{d}(n)$. Filtered versions of the reference signals $x'(n)$ and $\hat{d}'(n)$ are used to adapt the coefficients of the filters *F(z)* and *B(z)*.

To simulate the performance improvement of the hybrid system, it is assumed that the original vibration *d(n)* consists of two parts. The first part is called the observable part that can be observed by a reference sensor in advance. In Figure 2.14, *x(n)* is the reference signal, and *x(n)*p(n)* is the observable part in the original disturbance *d(n)*. Here, *p(n)* is the impulse response of the transfer function from the reference sensor to the error sensor. The second part of the original disturbance is called the unobservable part that is not observed by (or correlated to) the reference sensor. *u(n)* is used to denote the unobservable part in Figure 2.14. In the simulation, the real vibration signal of the Seagate Technology Inc. Barracuda18LP disc drive sampled at 10 *kHz* is used as the reference signal *x(n)* and the real vibration signal of the Barracuda9LP disc drive sampled at 10 *kHz* is used as the signal *u(n)* (Seagate Technology Inc. gave us these two models of HDD for experiments). Figure 2.15 shows the power spectral densities of *x(n)*p(n)*, *u(n)* and their summation *d(n)*, respectively. With these assumptions, the

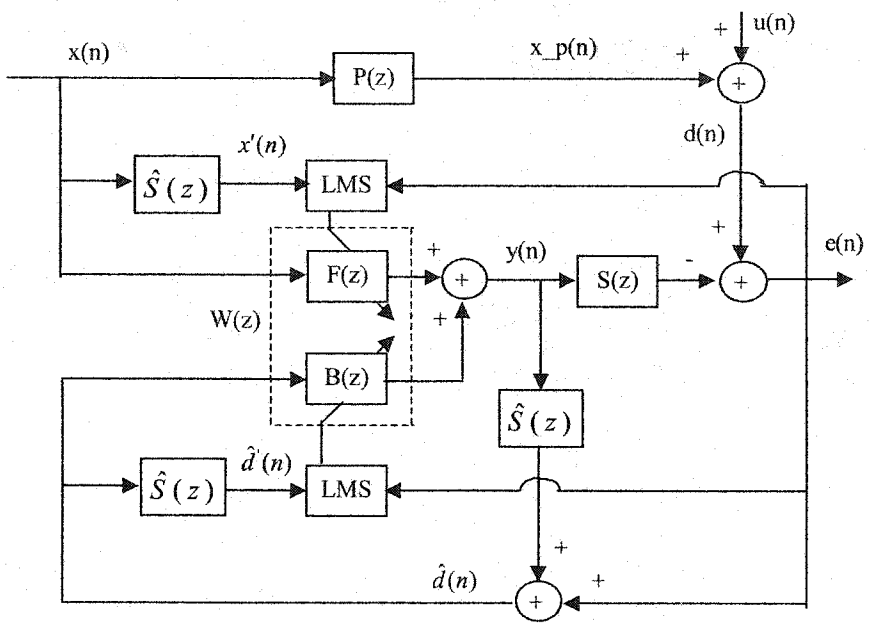



Figure 2.14 Hybrid active control scheme using the FXLMS algorithm.

feedback control system, the feed-forward control system and the hybrid control system are used to cancel the original vibration *d(n)* separately.

Figure 2.16 shows the power spectral densities of the residual error signals achieved by these three control systems. To compare the performance fairly, all the parameters in these three algorithms remain the same. It can be seen from Figure 2.16 that the feed-forward control system can only reduce the part in the original that is observed by the reference sensor. The feedback control system can only reduce the part that can be predicted (the predictable components come from both *x(n)* and *u(n)* because the restored vibration $\hat{d}(n)$ serves as the reference signal in the feedback control system). On the other hand, the hybrid control system greatly outperforms both

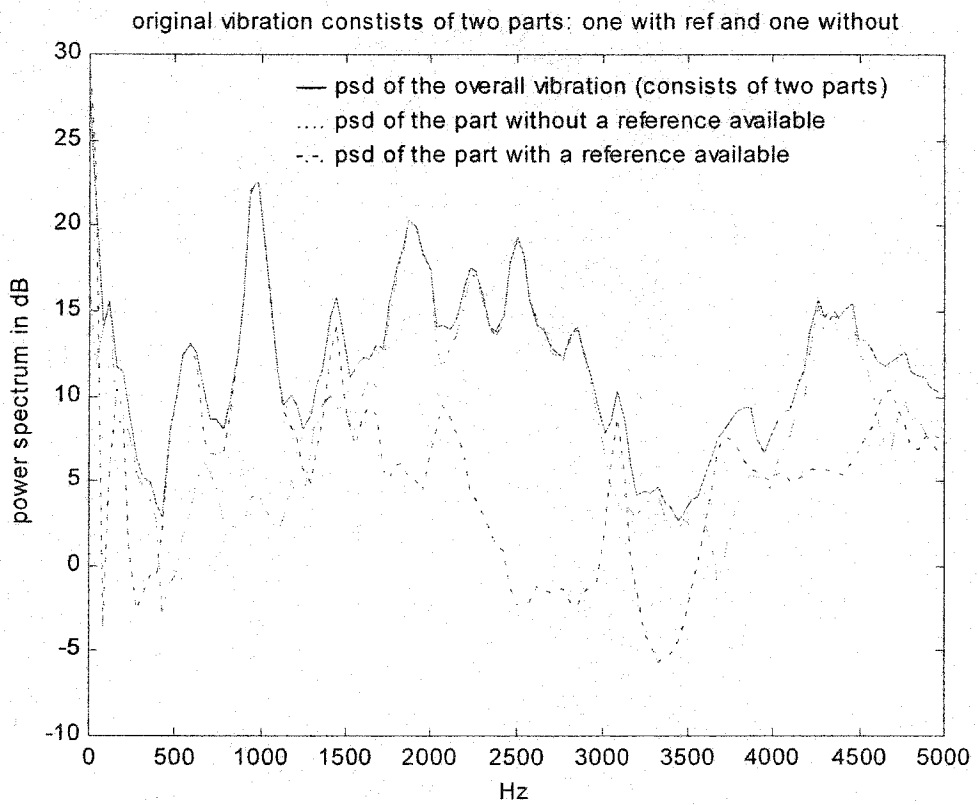



Figure 2.15 Power spectral densities of the original vibration *d(n)* (solid line) and its two components – *x(n)*p(n)* ( dashdot line) and *u(n)* (dotted line).

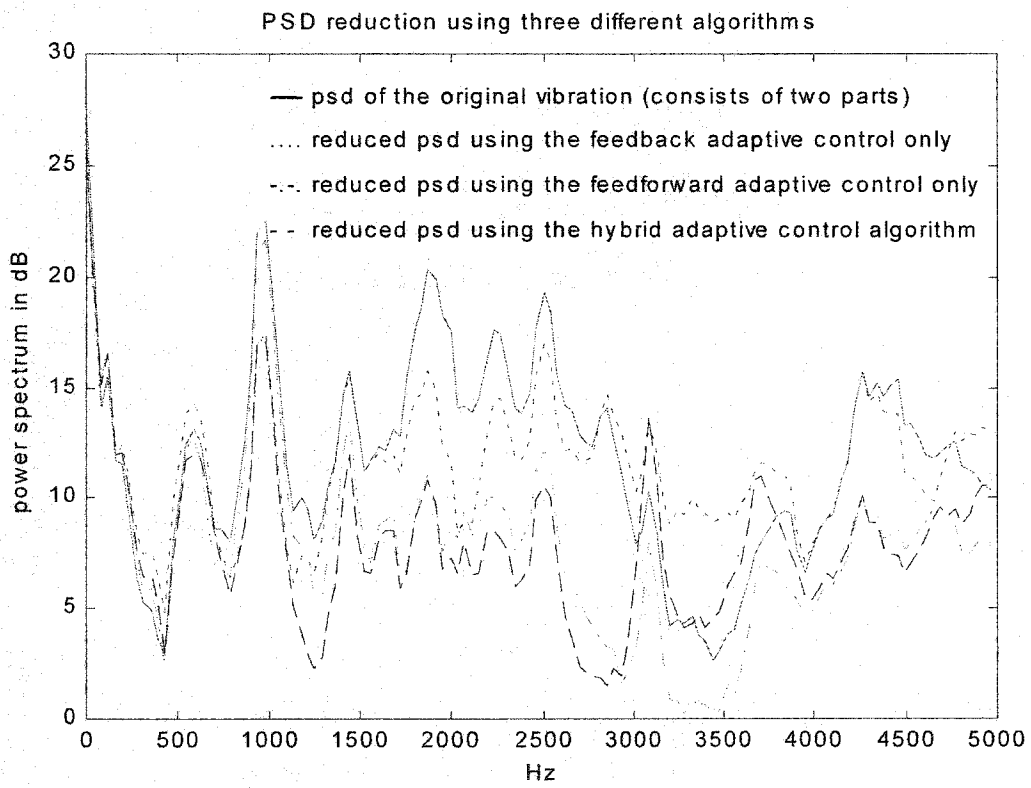



Figure 2.16 Power spectral densities of the residual error signals using the feed-forward control, the feedback control and the hybrid control, respectively.

the feed-forward system and the feedback system. It reduces both the predictable components and the part that is observed by the reference sensor. It should be noted that the actual performance that can be achieved by the hybrid control system depends on the amount of the disturbance that can be observed by the reference sensor as well as the transfer functions *P(z)* and *S(z)*. A randomly set $P(z) = 0.88 - .44z^{-1} - .22z^{-2} - .11z^{-3} + .33z^{-4}$ and the real identified $S(z) = 1.15 - .577z^{-1} - .161z^{-2} - .205z^{-3} - .189z^{-4} - .347z^{-5} + .446z^{-6} - .249z^{-7}$ are used in the simulation. The order of the feed-forward controller *F(z)* is set to 4 and the order of the feedback controller *B(z)* is set to 6, because our current hardware environment can only support such a short controller order for a reasonable sampling rate (*i.e.,* 10 kHz).

Another simulation is done to see the performance differences of the hybrid, feed-forward and feedback algorithms when all of the original vibration is observed by the reference sensor, that is, when *u(n)* does not exist in Figure 2.14. It is expected that the hybrid algorithm would not outperform the feed-forward algorithm greatly since all the original disturbance is correlated with the reference signal. Consequently, the feed-forward controller contributes more vibration reduction in the hybrid algorithm. Figure 2.17 shows the power spectral density of the original vibration (*x_p(n)* only) and the power spectral densities of the residual errors achieved by these three algorithms. It is shown that the hybrid algorithm does not outperform the feed-forward algorithm too much as it does in Figure 2.16, but it still outperforms the feed-forward algorithm. This is because the residual signal generated by the feed-forward controller is not a white noise and it can still be predicted in some degree. It can be concluded that the hybrid

algorithm is superior to the pure feed-forward algorithm when computational complexity is not at issue.

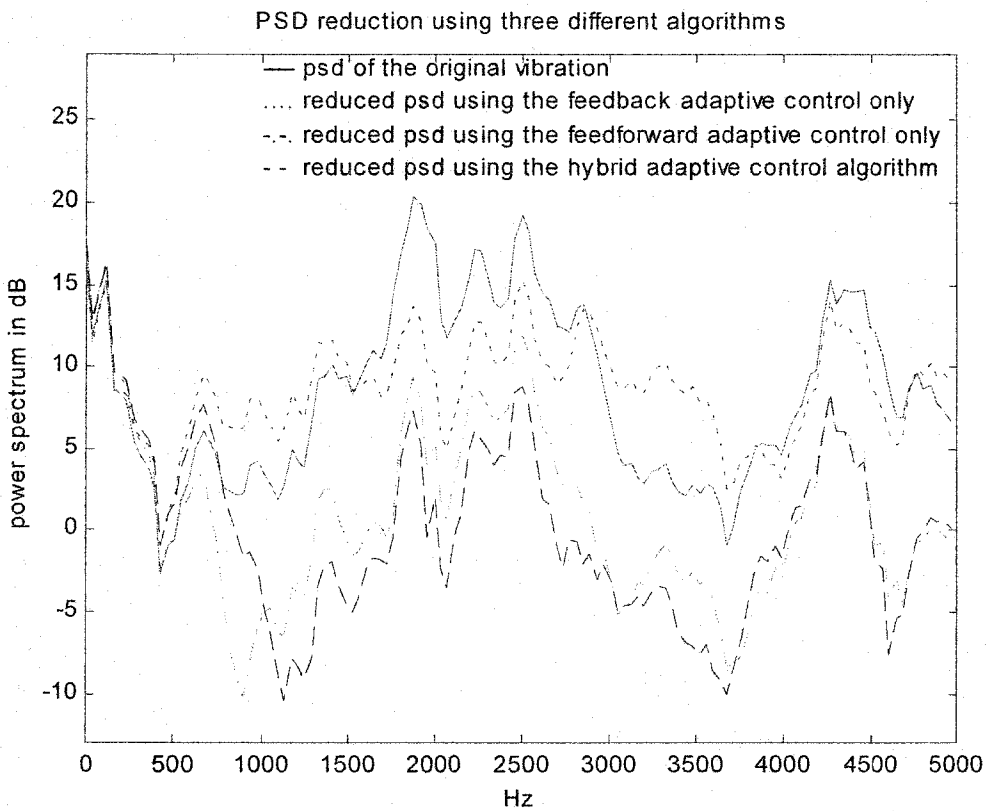



Figure 2.17 Power spectral densities of the residual error signals using the feed-forward control, the feedback control and the hybrid control, respectively, where all the original vibration can be observed by the reference sensor.

# Chapter 3

# Implementing the FXLMS in the frequency domain

Even though different adaptive algorithms exist that can be used for active control systems, the LMS algorithm is the one most widely used because of its computational efficiency and robustness. One of the main drawbacks of the LMS algorithm is its low convergence rate. If the convergence rate of the adaptive algorithm can be increased, the overall performance of the active control systems can be improved accordingly. Section 3.1 analyzes how the eigenvalue spread limits the convergence rate and shows why implementing the FXLMS in the frequency domain can improve the convergence rate. Section 3.2 compares the convergence properties of the algorithms implemented in the time domain method and in the frequency domain using the discrete cosine transform (DCT) and the discrete wavelet transform (DWT).

Another problem in the adaptive feedback control systems is the constructive interference due to the modeling error. Section 3.3 explains why the constructive interference occurs in the feedback control systems and proposes our selective adaptation in the frequency domain to alleviate the constructive interference while keeping the destructive interference at other frequencies.

## 3.1 Improving the convergence rate in the frequency domain

### 3.1.1 Eigenvalue spread limits the convergence rate

For steepest decent algorithms such as LMS, let $\boldsymbol{R}$ be the autocorrelation matrix of the input signal to an adaptive filter of order $N$, $W(z)$. $\boldsymbol{R}$ can be decomposed as

$$\boldsymbol{R} = \boldsymbol{Q}\,\boldsymbol{\Lambda}\,\boldsymbol{Q}^{H} \quad . \tag{3.1}$$

The matrix $\boldsymbol{Q}$ has as its columns $\boldsymbol{q}_i$, an orthogonal set of eigenvectors associated with the eigenvalues of the matrix $\boldsymbol{R}$. The matrix $\boldsymbol{\Lambda}$ is a diagonal matrix and has as its diagonal elements the eigenvalues of the autocorrelation matrix $\boldsymbol{R}$. These eigenvalues, denoted as $\lambda_1, \lambda_2, ..., \lambda_N$, must all be positive and real. Let $w$ be the tap-weight vector and define $c(n) = w(n) - w_0$ as the weight error vector at time instant $n$, where $w_0$ is the optimal value of the tap-weight vector, as defined by the Wiener-Hopf equation

$$\boldsymbol{R}\boldsymbol{w}_0 = \boldsymbol{p} \, . \tag{3.2}$$

The vector $\boldsymbol{p}$ is the cross-correlation vector between the tap-input vector $x(n)$ and the desired response $d(n)$. It can be easily shown that $w$ is updated along the negative gradient vector as

$$w(n+1) = w(n) + \mu[\,\boldsymbol{p} - \boldsymbol{R}w(n)], \quad n = 0,1,2,... \tag{3.3}$$

Eliminating $\boldsymbol{p}$ between Equation (3.2) and (3.3) and rewriting the result in terms of $c(n)$, we get

$$c(n+1) = (\boldsymbol{I} - \mu\boldsymbol{R})c(n) \, . \tag{3.4}$$

Substituting Equation (3.1) into Equation (3.4), we get

$$c(n+1) = (\boldsymbol{I} - \mu\boldsymbol{Q}\Lambda\boldsymbol{Q}^{H})c(n) \, . \tag{3.5}$$

Defining a new set of coordinates as

$$\boldsymbol{v}(n) = \boldsymbol{Q}^H \boldsymbol{c}(n) = \boldsymbol{Q}^H [\boldsymbol{w}(n) - \boldsymbol{w}_0] \tag{3.6}$$

and premultiplying both sides of Equation (3.5) by $\boldsymbol{Q}^H$, we get

$$\boldsymbol{v}(n+1) = (\boldsymbol{I} - \mu\boldsymbol{\Lambda})\boldsymbol{v}(n). \tag{3.7}$$

Assuming that the initial tap-weight vector $\boldsymbol{w}(0)$ is zero, then the initial value of $\boldsymbol{v}(0)$ equals

$$\boldsymbol{v}(0) = \boldsymbol{Q}^H [\boldsymbol{w}(0) - \boldsymbol{w}_0] = -\boldsymbol{Q}^H \boldsymbol{w}_0. \tag{3.8}$$

For the $k^{th}$ natural mode of the steepest descent algorithm, we have

$$v_k(n+1) = (1-\mu\lambda_k)v_k(n) = (1-\mu\lambda_k)^n v_k(0), k = 0,1,...,N-1. \tag{3.9}$$

To formulate the transient behavior of the original tap-weight vector $\boldsymbol{w}(n)$, we premultiply both sides of Equation (3.6) by $\boldsymbol{Q}$ and solve for $\boldsymbol{w}(n)$

$$\boldsymbol{w}(n) = \boldsymbol{w}_0 + \boldsymbol{Q}\boldsymbol{v}(n) = \boldsymbol{w}_0 + \sum_{k=0}^{N-1} \boldsymbol{q}_k v_k(n), \tag{3.10}$$

where $\boldsymbol{q}_i$ is the eigenvector associated with the eigenvalue $\lambda_i$ of the correlation matrix $\boldsymbol{R}$. Substituting Equation (3.9) into Equation (3.10), the transient behavior of the $i^{th}$ tap weight is described by [13]

$$w_i(n) = w_{oi} + \sum_{k=0}^{N-1} q_{ki} v_k(0)(1-\mu\lambda_k)^n, i = 0,1,...,N-1, \tag{3.11}$$

where $w_{oi}$ is the optimum value of the $i^{th}$ tap weight, and $q_{ki}$ is the $i^{th}$ element of the $k^{th}$ eigenvector $\boldsymbol{q}_k$.

Equation (3.11) shows that each tap weight in the steepest descent algorithms converges as the weighted sum of the exponential of the form $(1-\mu\lambda_k)^n$. Two observations can be made from Equation (3.11). First, provided $-1 < 1-\mu\lambda_k < 1$ for all

$k$, all the natural modes of the steepest decent algorithms approach zero as $n$ approaches infinity. This gives the convergence condition for the step size $\mu$, which must satisfy

$$0 < \mu < \frac{2}{\lambda_{\max}}. \tag{3.12}$$

Second, define the time constant $\tau_k$ as the time required for each term to reach *1/e* of its initial value, *i.e.*,

$$\tau_k = \frac{-1}{\ln(1-\mu\lambda_k)}. \tag{3.13}$$

The overall time constant, $\tau_a$, defined as the time required for the summation term in Equation (3.11) to decay to 1/e of its initial value, cannot be expressed in a simple closed form, but is bounded as

$$\frac{-1}{\ln(1-\mu\lambda_{\max})} \le \tau_a \le \frac{-1}{\ln(1-\mu\lambda_{\min})}. \tag{3.14}$$

Therefore, when the eigenvalues of the autocorrelation matrix $\boldsymbol{R}$ are widely spread, the settling time of the steepest decent algorithms is limited by the smallest eigenvalues or the slowest modes. So, if we could reduce the eigenvalue spread of the input autocorrelation matrix, the convergence rate could be correspondingly improved.

### 3.1.2. Reducing the eigenvalue spread in the frequency domain

Equation (3.14) shows that the eigenvalue spread of the input autocorrelation matrix restricts the convergence rate. One approach to accelerate the convergence rate is to somehow transform the input signal *x(n)* into another signal whose corresponding

autocorrelation matrix has a smaller eigenvalue spread. This can be achieved by performing the adaptive filtering in some orthogonal transform domain.

A block diagram of the transform domain adaptive filter is shown in Figure 3.1. The input time domain vector ***x(n)*** is first transformed into a transform domain vector $\boldsymbol{X}_n = [X_0, X_1, ..., X_{N-1}]$ by the orthogonal transform

$$\boldsymbol{X}_n = \boldsymbol{T}\boldsymbol{x}(n) \tag{3.15}$$

where $\boldsymbol{T}$ is a unitary matrix of rank $N$.

Now, the transform domain vector $\boldsymbol{X}_n$ is multiplied by the transform domain weight vector

$$\boldsymbol{W}(n) = [W_0(n), W_1(n), ..., W_{N-1}(n)]^T \tag{3.16}$$

to form the adaptive output $y(n)$. The output and the residual error signal are

$$y(n) = \boldsymbol{X}_n^T \boldsymbol{W}(n) \tag{3.17}$$

and

$$e(n)=d(n)-y(n) \tag{3.18}$$

respectively. The weight updating equation is

$$W_i(n+1) = W_i(n) + 2\mu_i e(n) X_i,\ i = 0,1,...,N-1 \tag{3.19}$$

where

$$\mu_i = \frac{\mu}{E(X_i^2)},\ i = 0,1,...,N-1 \tag{3.20}$$

is the adaptive step size for the $i^{th}$ transform component. Let $\boldsymbol{\Lambda}^2$ be an N×N diagonal matrix whose $(i,i)^{th}$ element is equal to the power estimate of $X_i$. The weight vector equation can be written in matrix form as

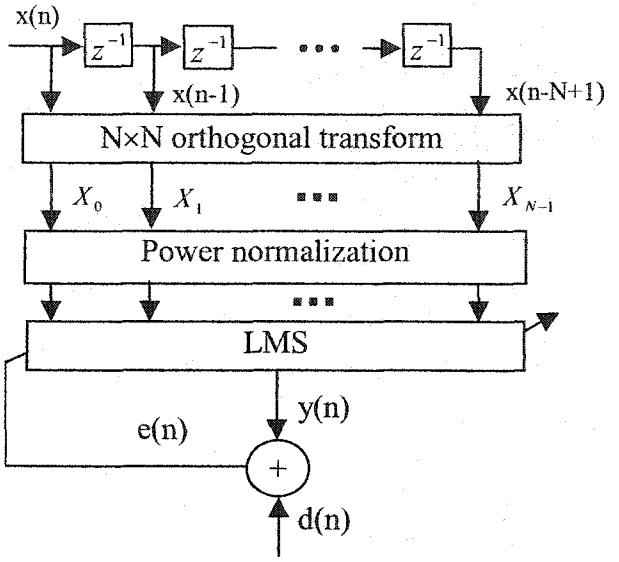



Figure 3.1 Block diagram of adaptive filtering in the frequency domain.

$$W(n+1) = W(n) + 2\mu\Lambda^{-2}e(n)X_n . \tag{3.21}$$

Let $R_{xx}$ be the autocorrelation matrix of the time domain input signal $x(n)$, *i.e.*,

$$R_{xx} = E[x(n)x^T(n)] \tag{3.22}$$

and let $R_{XX}$ be the autocorrelation matrix of the transform domain signal $X_n$, *i.e.*,

$$R_{XX} = E[X_n X_n^T] . \tag{3.23}$$

The speed of the convergence of the weight vector $W(n)$ in the frequency domain now depends on the eigenvalue spread of the matrix $\Lambda^{-2}R_{XX}$. If it can be shown that the condition number, *i.e.*, the eigenvalue spread of $\Lambda^{-2}R_{XX}$, is less than the condition number of $R_{xx}$, then the convergence rate of the adaptive algorithm implemented in the transform domain can be improved relative to the time domain implementation.

Without loss of generality, assume that the input signal power is unity, *i.e.*,

$$E(x^2(n)) = 1. \tag{3.24}$$

Let *tr(A)* denote the trace and *det(A)* denote the determinant of a square matrix $A$. Then,

$$\lambda_{\max} \le tr(A). \tag{3.25}$$

For $N > 2$, it can be generally shown that [16]

$$\lambda_{\min} \ge \det(A). \tag{3.26}$$

Therefore, the ratio

$$\gamma(A) = \frac{tr(A)}{\det(A)} \tag{3.27}$$

can be used as an upper bound for $\lambda_{\max} / \lambda_{\min}$. Now,

$$\det(\Lambda^{-2} \boldsymbol{R}_{XX}) = det(\Lambda^{-2}) \det(\boldsymbol{R}_{XX}) = \det(\Lambda^{-2}) \det(\boldsymbol{R}_{xx}) \tag{3.28}$$

and

$$tr(\Lambda^{-2} \boldsymbol{R}_{XX}) = tr(\boldsymbol{R}_{xx}) = N. \tag{3.29}$$

Therefore,

$$\gamma(\Lambda^{-2} \boldsymbol{R}_{XX}) = \frac{tr(\boldsymbol{R}_{xx})}{\det(\Lambda^{-2}) \det(\boldsymbol{R}_{xx})} = \det(\Lambda^2) \gamma(\boldsymbol{R}_{xx}). \tag{3.30}$$

Since $tr(\Lambda^2) = N$, *i.e.*, the smallest eigenvalue of $\Lambda^2$ is less than or equal to unity, $\det(\Lambda^2)$ is always assured to be less than or equal to unity. Hence,

$$\gamma(\Lambda^{-2} \boldsymbol{R}_{XX}) \le \gamma(\boldsymbol{R}_{xx}) \tag{3.31}$$

That is, for a properly chosen orthogonal transform $\boldsymbol{T}$, some reduction in the eigenvalue spread might be expected.

## 3.2 Simulation results of the frequency domain algorithm

A unitary transform $\boldsymbol{T}$ is required to implement the transform domain algorithm. If $\boldsymbol{T}$ can be chosen such that $\boldsymbol{R}_{XX}$ is completely diagonal, the eigenvalue spread of $\boldsymbol{\Lambda}^{-2}\boldsymbol{R}_{XX}$ is equal to unity, which implies that the adaptive filter implementation in that domain will have the best convergence properties. The corresponding $\boldsymbol{T}$ is generally known as Karhunen-Loeve transform (KLT) [13]. The KLT is a signal-dependent transform, the implementation of which requires the estimation of the correlation matrix of the input vector, the diagonalization of this matrix, and the construction of the required basis vector. These computations make the KLT impractical for real-time applications. In practice, other transforms such as the discrete Fourier transform (DFT), the discrete cosine transform (DCT), the Walsh-Hadamard transform (DHT), the discrete Hartley transform (DHT) and the Powers-Of-Two (PO2) transform are used as the approximation to the KLT [17]-[19]. Recently, the discrete Wavelet transform (DWT) was also used as the transform algorithm [20]. In this section, we simulate the performance of the DCT and the DWT due to their effectiveness and popularity.

The DCT matrix elements are given by [21]

$$t_{mn} = \begin{cases} \dfrac{1}{\sqrt{N}}, m = 0; n = 0,1,\ldots,N-1, \\ \sqrt{\dfrac{2}{N}}\cos\dfrac{\pi(2n+1)m}{2N}, m = 1,2,\ldots,N-1; n = 0,1,\ldots,N-1. \end{cases} \tag{3.32}$$

The DWT transforms the time domain signal $x(n)$ to the transform domain coefficients by [20]

$$X_i^n(j) = \sum_{k=0}^{m-1} h_i(k)x(Mj-k+n) \tag{3.33}$$

where $m$ is the wavelet filter length, $M$ is the number of sub-bands in the wavelet filter bank, and $n$ stands for time instant, $i=0,1,...,M-1$ and $j=-(N/M)+1, ...,-1,0$. For a two-band filter bank, *i.e.*, $M=2$, if the order of the adaptive filter $N=8$ and we also use $8^{th}$-order wavelet filters, the transform matrix can be written as

$$\boldsymbol{T} = \begin{bmatrix} h_0(0) & h_0(1) & h_0(2) & h_0(3) & h_0(4) & h_0(5) & h_0(6) & h_0(7) \\ h_0(6) & h_0(7) & h_0(0) & h_0(1) & h_0(2) & h_0(3) & h_0(4) & h_0(5) \\ h_0(4) & h_0(5) & h_0(6) & h_0(7) & h_0(0) & h_0(1) & h_0(2) & h_0(3) \\ h_0(2) & h_0(3) & h_0(4) & h_0(5) & h_0(6) & h_0(7) & h_0(0) & h_0(1) \\ h_1(0) & h_1(1) & h_1(2) & h_1(3) & h_1(4) & h_1(5) & h_1(6) & h_1(7) \\ h_1(6) & h_1(7) & h_1(0) & h_1(1) & h_1(2) & h_1(3) & h_1(4) & h_1(5) \\ h_1(4) & h_1(5) & h_1(6) & h_1(7) & h_1(0) & h_1(1) & h_1(2) & h_1(3) \\ h_1(2) & h_1(3) & h_1(4) & h_1(5) & h_1(6) & h_1(7) & h_1(0) & h_1(1) \end{bmatrix} \tag{3.34}$$

where $h_0(k)$ is the $8^{th}$-order low-pass wavelet filter and $h_1(k)$ is the $8^{th}$ order high-pass wavelet filter.

Figures 3.2, 3.3, and 3.4 plot the ensemble-averaged learning curves of the time domain LMS and the frequency domain LMS using the DCT and the DWT with the Daubechies wavelet for three different eigenvalue spreads. Three *AR(2)* processes are generated such that the eigenvalue spreads are 1.22, 3, and 10, respectively [13], so that we can compare the performance for different eigenvalue spreads. Figure 3.5 plots the ensemble-averaged learning curves of frequency domain LMS using the DWT with three different wavelets. Each algorithm runs for 100 times and the learning curves in these three figures are the average over the 100 runs. The following observations can be made from these simulations:

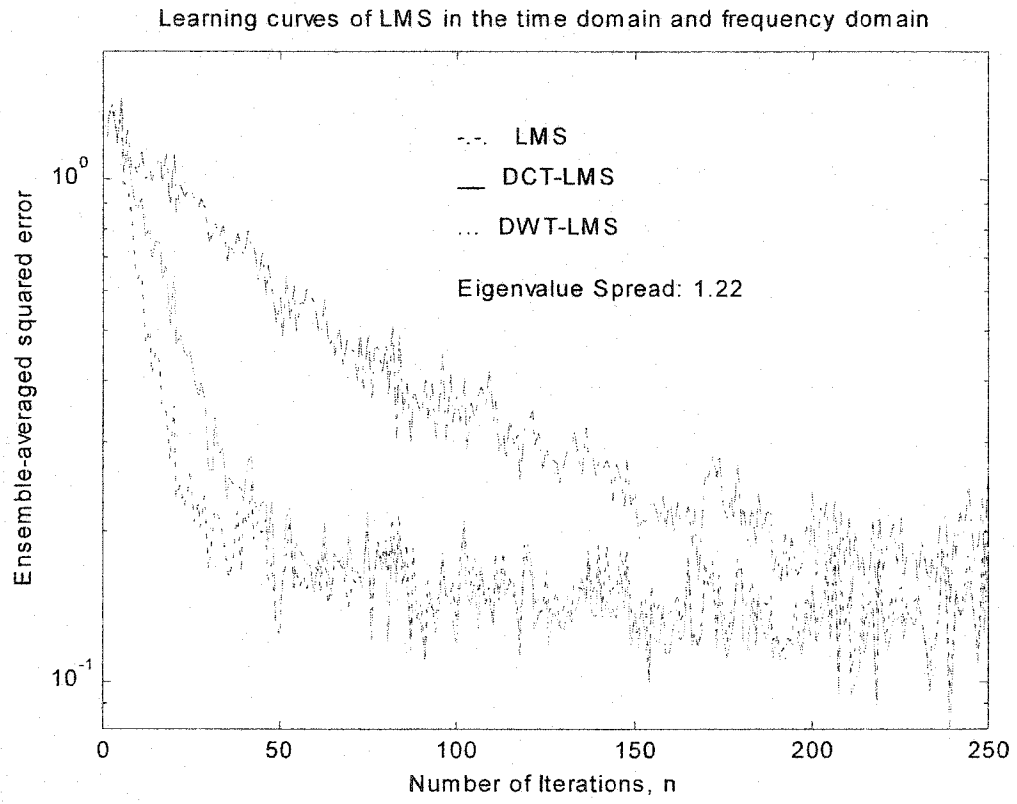



Figure 3.2 Learning curves of the time domain LMS and the frequency domain LMS using the DCT and the DWT as the transform matrix (eigenvalue spread = 1.22).

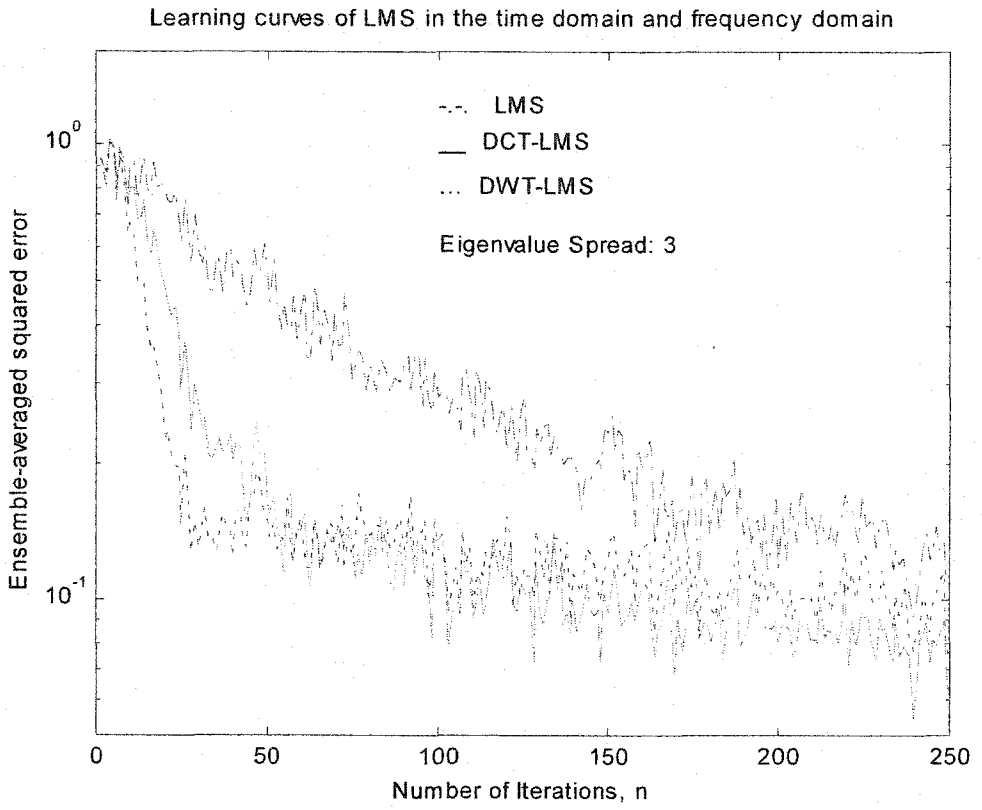



Figure 3.3 Learning curves of the time domain LMS and the frequency domain LMS using the DCT and the DWT as the transform matrix (eigenvalue spread = 3).

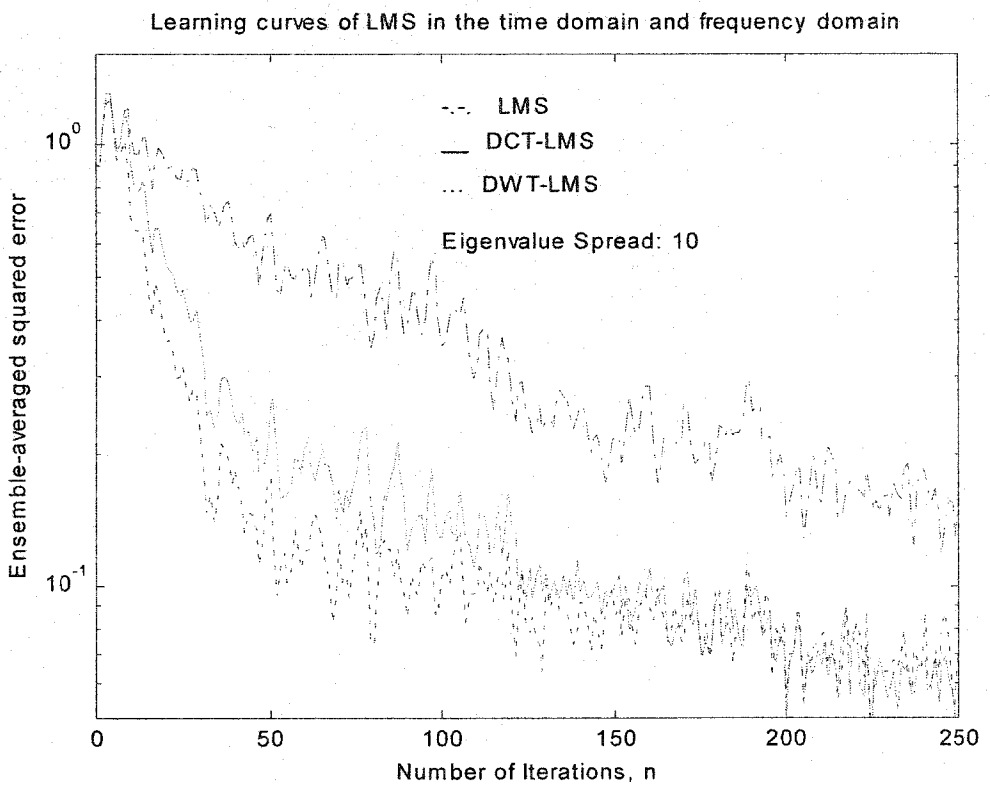



Figure 3.4 Learning curves of the time domain LMS and the frequency domain LMS using the DCT and the DWT as the transform matrix (eigenvalue spread = 10).

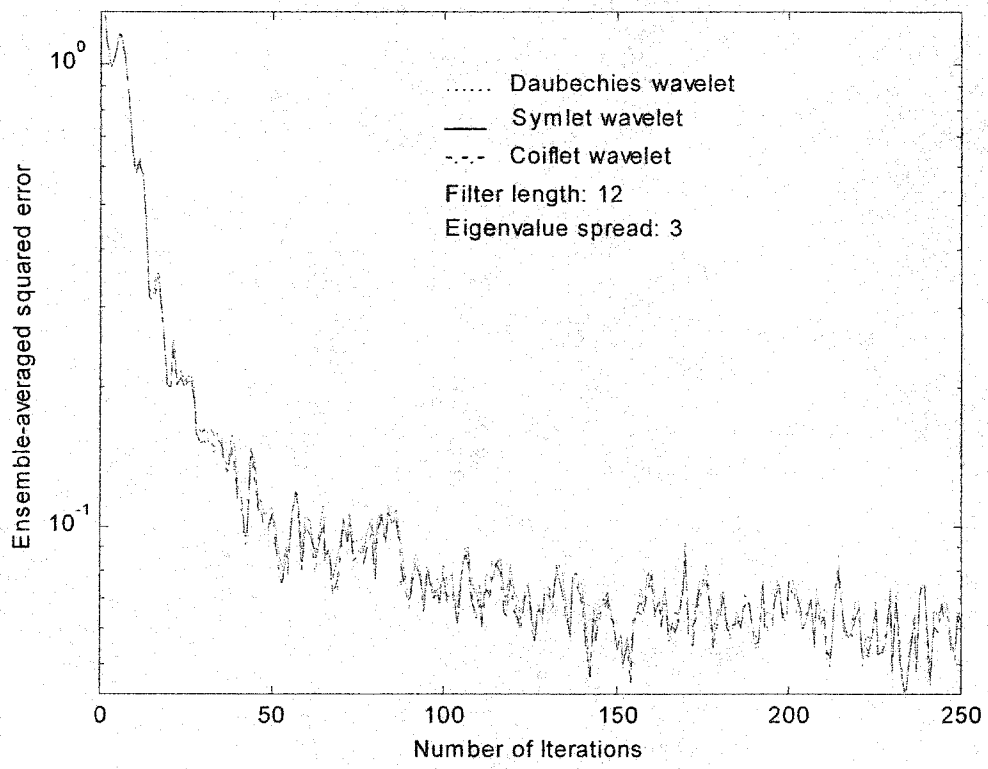



Figure 3.5 Learning curves of the frequency domain LMS using the DWT as the transform matrix but with different wavelets (eigenvalue spread = 3).

- The time domain LMS algorithm consistently behaves worst, in that it exhibits the slowest rate of convergence and the greatest sensitivity to variations in the eigenvalue spread.
- Both the DCT-LMS and the DWT-LMS consistently achieve faster convergence rates than the time domain LMS. The DWT-LMS slightly outperforms the DCT-LMS.
- The selection of different wavelet does not make a big difference in the DWT-LMS.
- The convergence rate of the frequency domain LMS is relatively insensitive to the variations in the eigenvalue spread.

When the frequency domain LMS is applied to HDD vibration control, the extra computational requirements associated with the transform consequently reduce the possible sampling rate. This decrease in the sampling rate depends on the implementation method. For the discrete cosine transform, even with the most efficient implementation called the frequency sampling structure [22] (refer to Appendix B for the derivation), only an 8.4 *kHz* sampling rate can be achieved for an $8^{th}$-order controller. Figure 3.6 shows the vibration reduction achieved by the frequency domain FXLMS using the discrete cosine transform (DCT-FXLMS algorithm) with an 8.4 *kHz* sampling rate in real time.

It is difficult to fairly compare the performances of the time domain algorithm with the frequency domain algorithm using the real time setup because the vibration of the HDD is time-varying and the sampling rate cannot be adjusted to precisely the same for the system with control on and the system with control off. Instead, simulations are

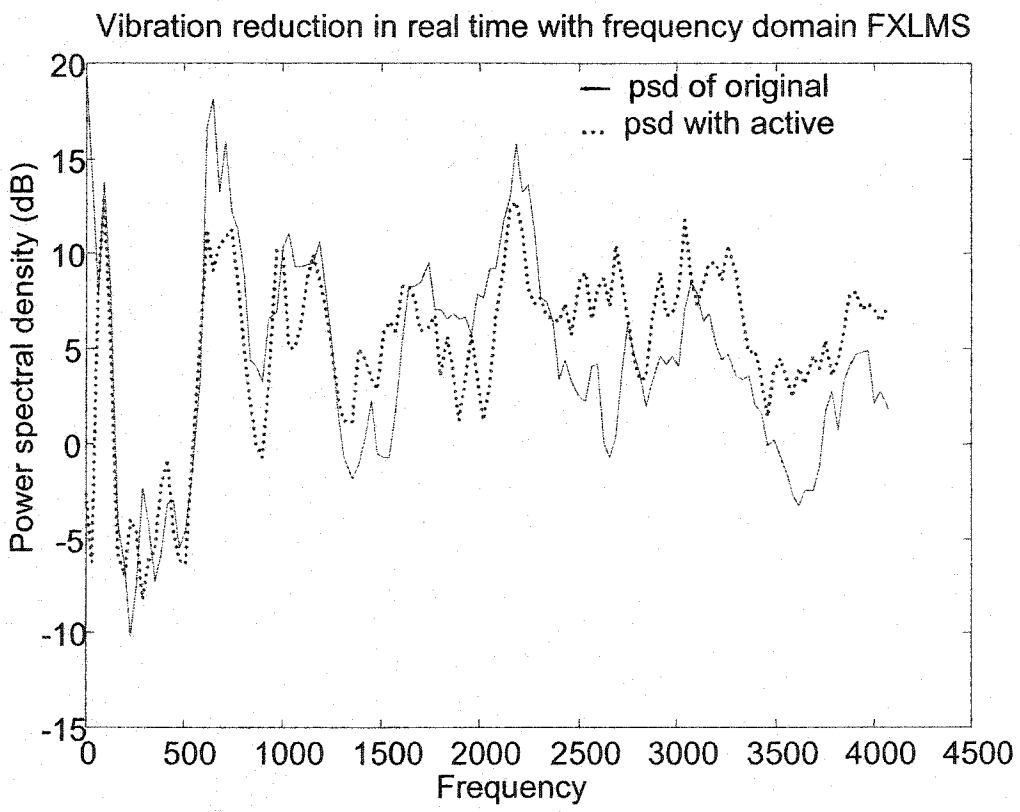



Figure3.6 Vibration reduction in real time with the frequency domain FXLMS algorithm using the discrete cosine transform.

performed to compare the performances of the time domain FXLMS and the DCT-FXLMS on reducing the vibration sampled at 16 *kHz*. Figure 3.7 gives the average power spectral density of the original vibration in 0.5 second (*i.e.*, 8000 samples) and the power spectral densities when the active control systems using both the time domain FXLMS and the DCT-FXLMS are operating. This simulation shows that the power spectral density of the residual error achieved by the DCT-FXLMS is slightly flatter. In other words, the frequency domain method achieves better vibration reduction in the destructive interference range while the constructive interference is also enhanced. The next section will discuss the constructive interference.

## 3.3 Reducing the constructive interference by selective adaptation

It was mentioned in Chapter 2 that the performance of the adaptive feedback control system depends on the accuracy of representing *S(z)* by a MA process $\hat{S}(z)$, and the predictability of the primary disturbance filtered by the secondary path. The predictability of the primary disturbance filtered by the secondary path in turn depends on the primary disturbance itself and on the order of the predictor, *i.e.*, on the order of the control filter. Also, some random processes may require a very long adaptive filter to predict the process accurately. Some random processes simply cannot be predicted very well. The more of the primary disturbance that "leaks" through the predictor, the poorer the performance [13]. The modeling error due to insufficient length of the adaptive filter or the primary disturbance may result in the presence of constructive interference in some frequency bands. It can be seen from Figure 3.6 and Figure 3.7 that

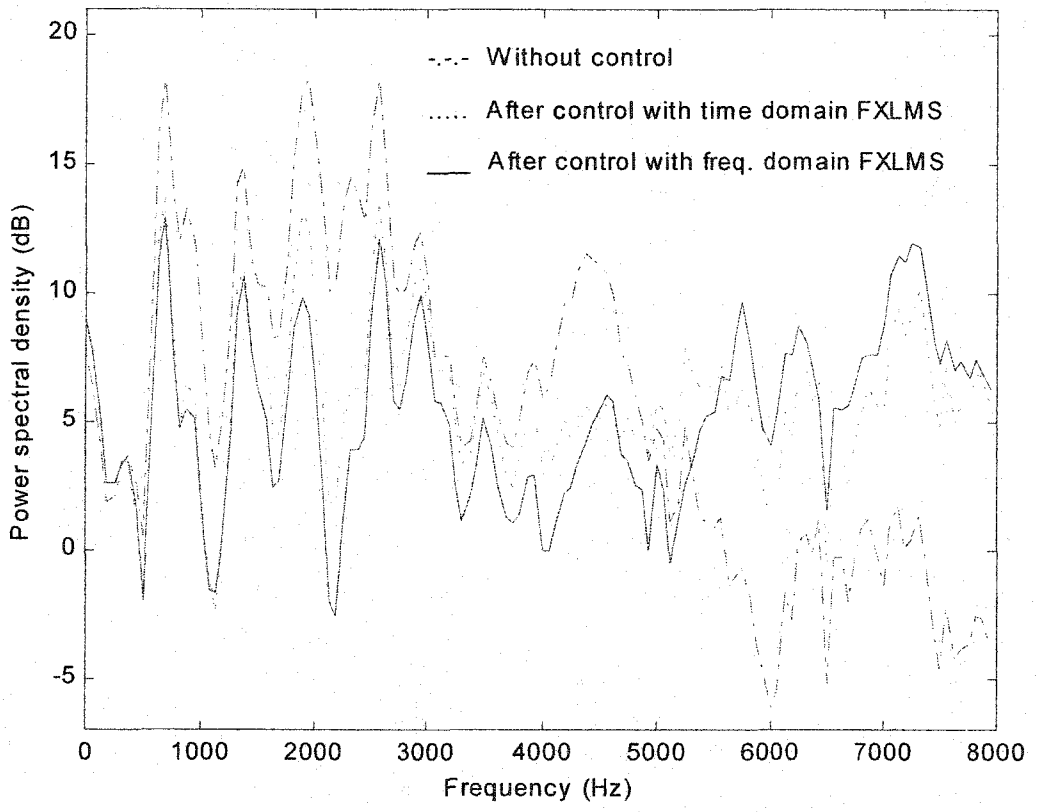



Figure 3.7 Simulation result of vibration reduction with the time domain FXLMS (dotted line) and the frequency domain FXLMS (solid line) using the discrete cosine transform.

the constructive interference occurs at high frequencies while the desired destructive interference is achieved at the lower frequencies.

It is desirable to reduce or alleviate the constructive interference while simultaneously keeping the destructive interference that can be achieved by the active control systems. Since the extra vibration in the constructive interference band(s) comes from the control signal, low-pass or band-pass filtering (depending on where the constructive interference occurs) of the control signal before feeding it to the actuator may help somewhat. However, the sample delay associated with the causal, real-time low-pass or band-pass filtering increases the requirements on the adaptive forward predictor, and hence reduces the effectiveness of the predictor. This dissertation proposes a technique called selective adaptation in the frequency domain [23]. The basic idea of the selective adaptation is to generate the control signal in such a way that it does not contain energy in the frequency bands where the constructive interference occurs. Then, the constructive interference can be avoided without adding extra delay in the control path. The selective adaptation requires the adaptive algorithm to be implemented in the frequency domain.

Figure 3.8 shows the idea of the selective adaptation in the frequency domain, where DCT is used as the transform. We only update those $M$ filter weights in Equation (3.16) that correspond to the destructive interference bands. Then, the control signal $y(n)$, which is inversely transformed from the $M$ frequency coefficients corresponding to the destructive interference bands, will not include the frequency components corresponding to the constructive interference bands. Consequently, the constructive

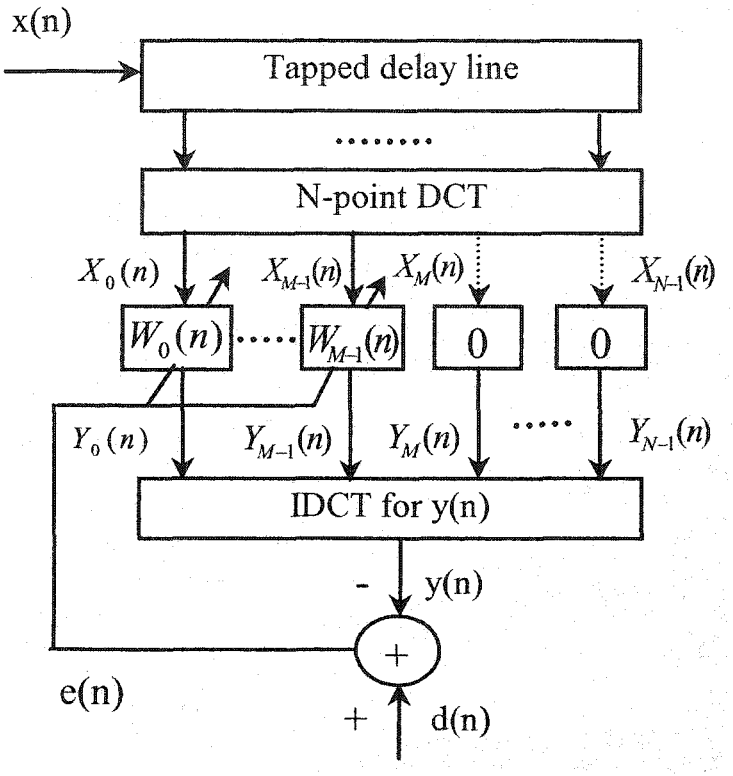



Figure 3.8 Selective adaptation of the adaptive algorithm in the frequency domain.

interference in the residual error can be avoided. Note that the IDCT for y(n) can be replaced by a pure summation because the coefficients required to calculate *y(n)* by

$$y(n) = \frac{1}{\sqrt{2}} \sum_{k=0}^{N-1} \cos \frac{k\pi}{2N} Y(k) \tag{3.35}$$

can be absorbed by the corresponding filter weights $W_k$. It should be noted that the DCT transform in the frequency domain method serves as a preprocessing step in the adaptive filtering process. It transforms an N-point time domain vector ***x(n)*** into an equivalent frequency domain vector *X(n)*. Therefore, the DCT transform does not result in signal path delay in the feedback control system.

Figure 3.9 shows the constructive interference alleviation for the real HDD vibration signal when the last three weights of an $8^{th}$-order adaptive filter are discarded. For comparison purposes, the active control using the same LMS adaptive parameters, but without discarding the weights is also given. Figure 3.10 gives the same information for an *AR(2)* process where the last three weights of a $10^{th}$-order adaptive filter are discarded. It can be seen from Figure 3.9 and Figure 3.10 that the constructive interferences are alleviated by several *dB* at the high frequencies at the cost of some degradation in performance at the neighboring frequency band. The degradation at this boundary band results from the leakage of the DCT transform. The DCT is not a perfect decorrelator but an approximation. When the LMS algorithm is implemented in the frequency domain using the DCT, the DCT acts like *N* band-pass filters. Because of the presence of the side lobes of these band-pass filters, there is some leakage from each frequency bin to the others. Figure 3.11 shows the magnitude response of the $2^{nd}$ transfer function of a 10-point DCT. This kind of leakage has two undesirable effects on the selective adaptation. First, some energy from the frequency bins corresponding to the destructive interference leaks into the frequency bins corresponding to the constructive interference. When the weights corresponding to the constructive interference are discarded, so is the leaked energy from the desired frequency bins. This degrades the performance of the active control system in reducing the desired destructive interference. Second, the energy of the frequency bins corresponding to the constructive interference leaks into the frequency bins corresponding to the destructive interference. Hence, the constructive interference cannot be reduced completely by discarding the weights corresponding to the constructive interference. The length of the

DCT transform directly impacts the performance. As the length increases, the relative sidelobe level and the width of the lobe decreases (Figure 3.12 shows the magnitude response of the 2nd transfer function of a 16-point DCT). Consequently, it is more flexible to shape the frequency coefficients for performance improvement. One limitation is that we cannot increase the length of the DCT transform at will. The length of the DCT transform is the order of the control filter that should be determined by the nature of the primary disturbance and the computational resource available.

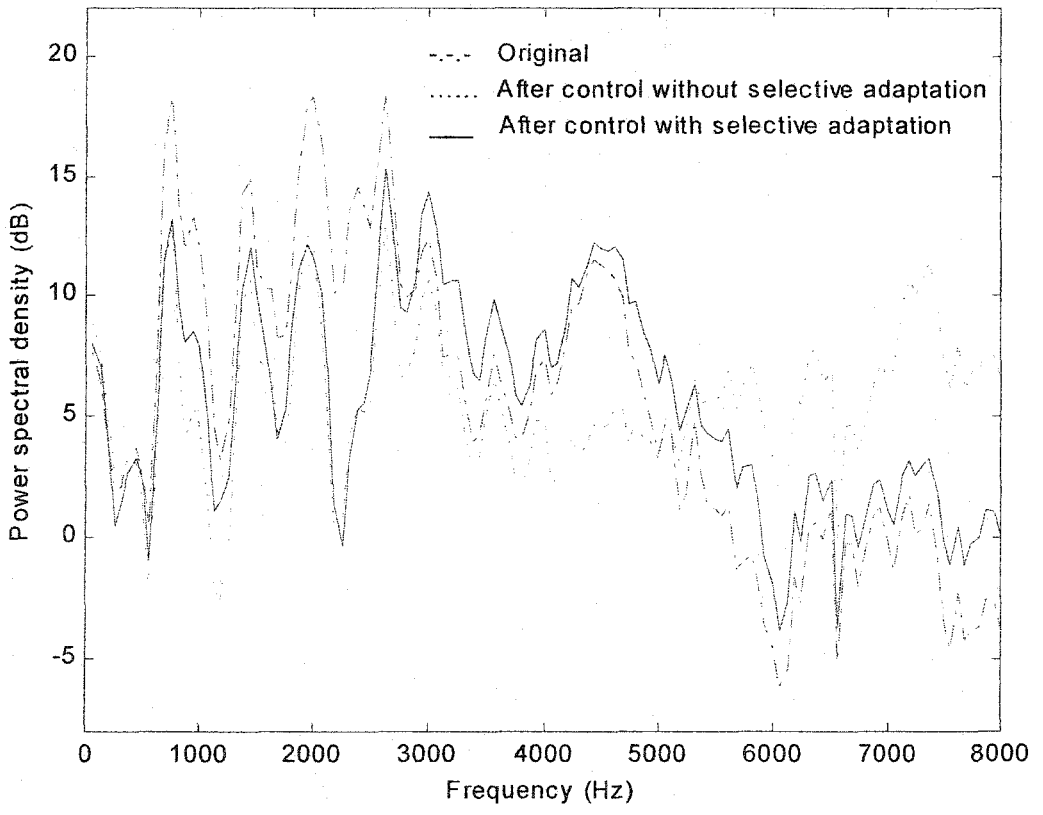



Figure 3.9 Effect of alleviating the constructive interference by the selective adaptation in the frequency domain for the real HDD vibration signal.

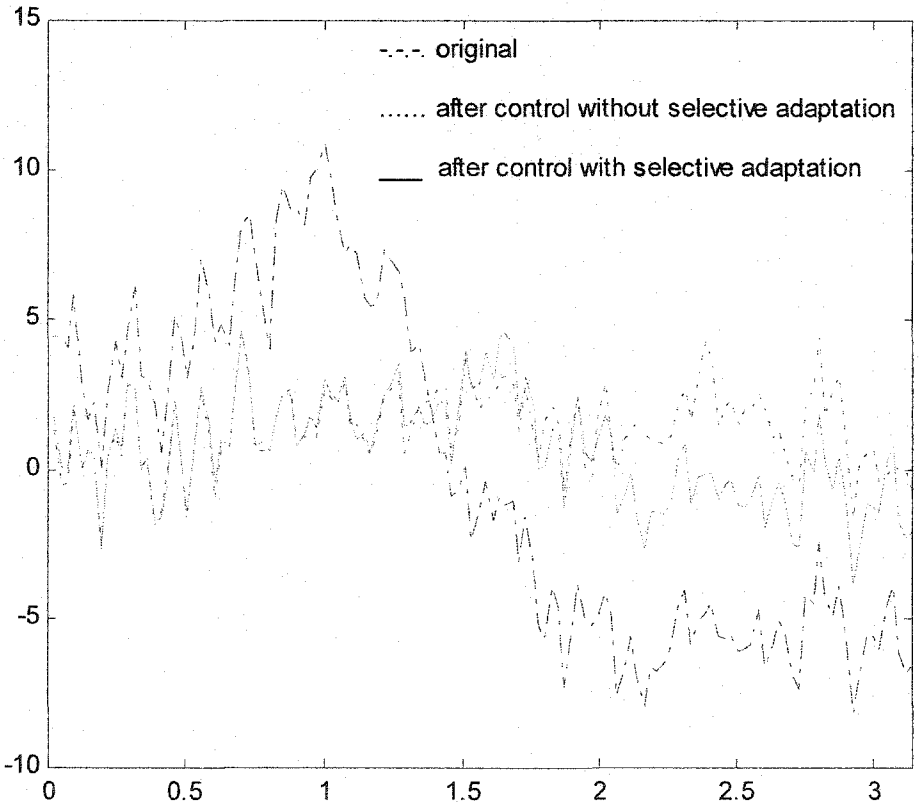



Figure 3.10 Effect of alleviating the constructive interference by the selective adaptation in the frequency domain for an AR(2) process.

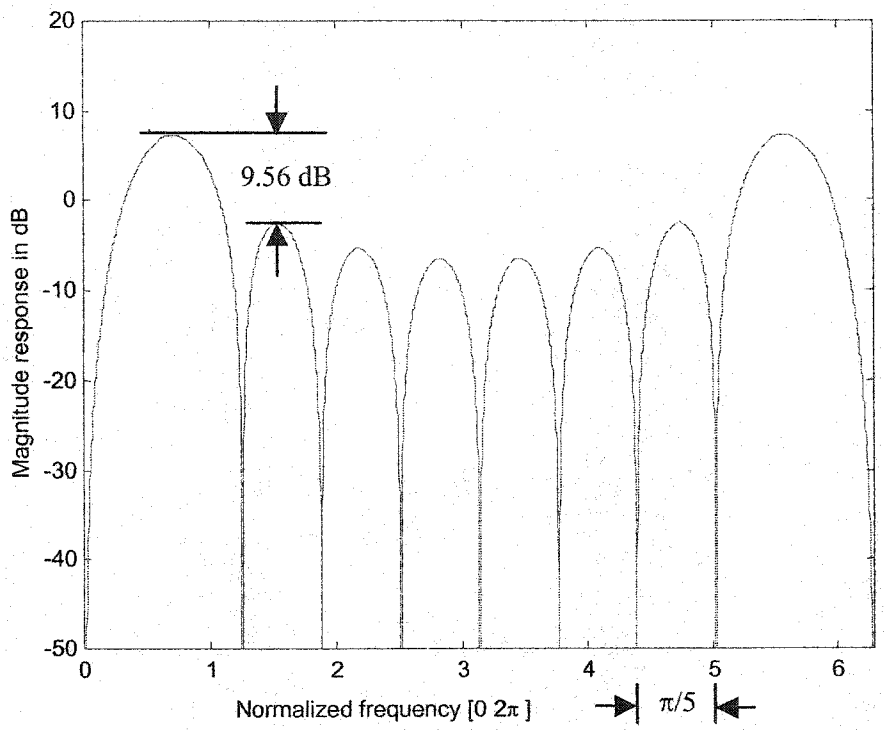



Figure 3.11 Magnitude response of the 2nd transfer function of a 10-point DCT.

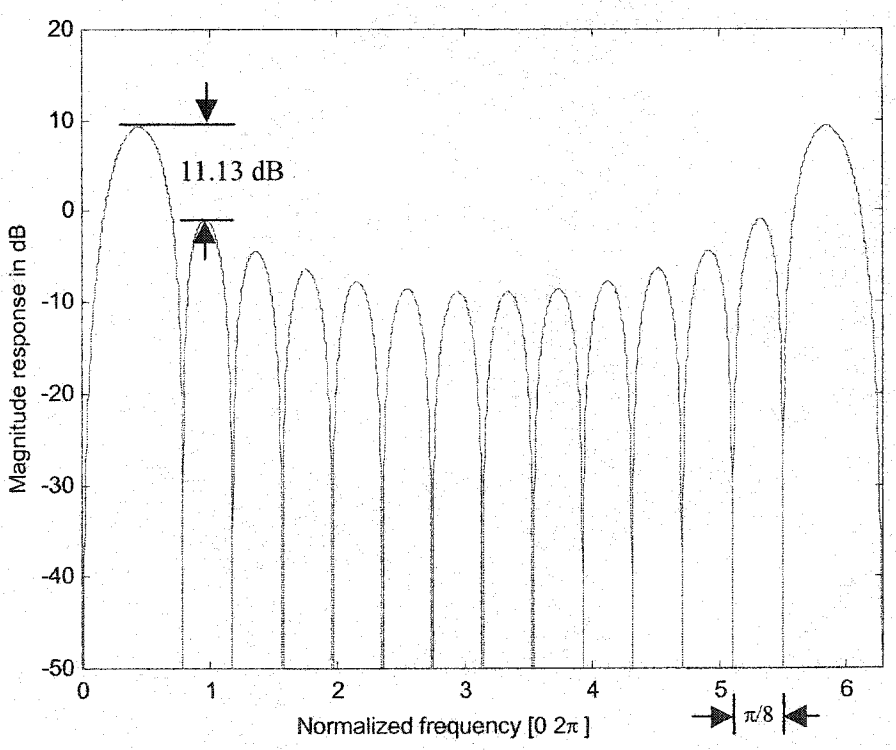



Figure 3.12 Magnitude response of the 2nd transfer function of a 16-point DCT.

# Chapter 4

# Implementing the adaptive algorithm in sub-bands

Chapter 3 described our methods for improving the convergence rate of the LMS algorithm in the frequency domain. Recently, the sub-band technique has also been developed to improve the convergence rate. It has been successfully used in adaptive filtering for system identification and echo cancellation [24]-[28]. In these applications, both the reference signal and the ideal signal are available and are decomposed into sub-bands to form the sub-band error signals. The full-band residual error signal is then synthesized from the sub-band error signals through the synthesis filter bank. In these applications, all adaptation is performed using the sub-bands.

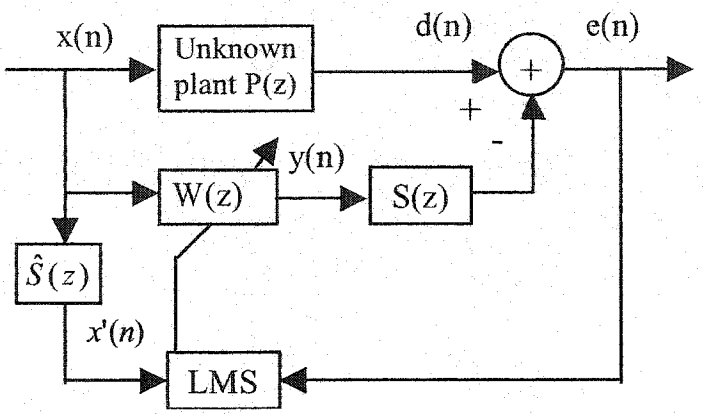
In the application of active control of noise and vibration, the ideal signal in terms of the adaptive filtering is generally not accessible. Furthermore, active control systems generally cannot tolerate extra delay along the signal path, *i.e.,* the path from the reference signal to the error signal, especially for the feedback active control of noise and vibration. To avoid the signal path delay, Morgan ([29], [30]) proposed a delayless sub-band adaptive filter architecture in which the adaptive weights are computed in the sub-bands but collectively transformed into an equivalent set of full-band filter coefficients before generating the control signal. Hirayama [31] employed a different transform to obtain the full-band filter coefficients from the sub-band counterparts. This dissertation proposes a different sub-band adaptive architecture in which the full-band

filter coefficients are updated directly based on the sub-band reference signals and sub-band error signals [32], [33]. Even though the signal path delay is avoided in both architectures, the group delay associated with the analysis filter bank is still added to the error path (the weight updating path) and will decrease the convergence region of the step size. The convergence region of the step size is defined as the upper stability bounds of the convergence factor. This dissertation also proposes a delay compensation method by modifying the sub-band adaptive algorithm to compensate for the error path delay, hence increasing the convergence region of the step size.

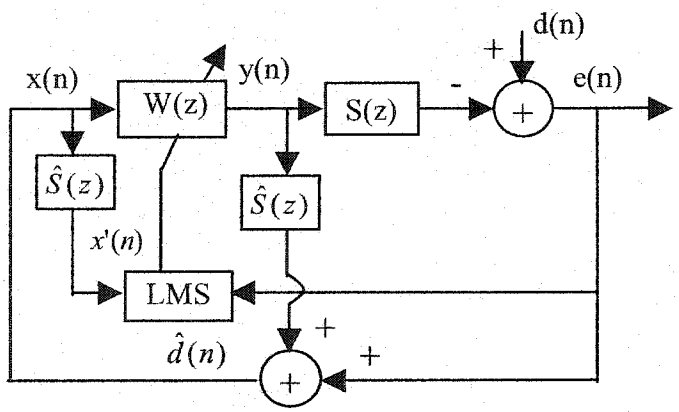
Section 4.1 derives the sub-band adaptive algorithm using the gradient descent method. Section 4.2 discusses the delay compensation methods of increasing the convergence region of the step size. Computer simulations are performed in Section 4.3 to illustrate the efficiency of the sub-band algorithm. Section 4.4 discusses the combination of the sub-band decomposition with the frequency domain technique for performance improvement. Section 4.5 summaries the computational complexities of different adaptive algorithms.

## 4.1 Sub-band adaptive filtering without signal path delay

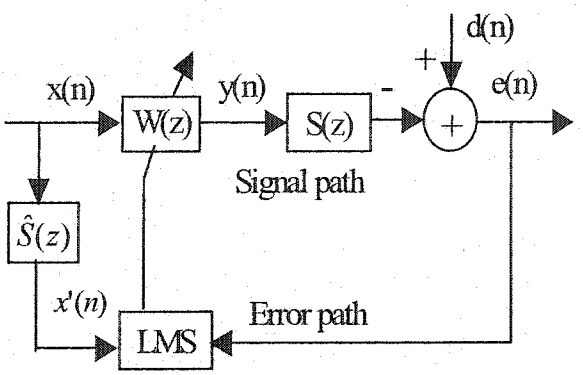
The feed-forward active control system shown in Figure 4.1(a) and the feedback active control system shown in Figure 4.1(b) can be viewed as a unified structure in adaptive filtering theory as shown in Figure 4.1(c). It should be noted that even though the adaptive filter structure in Figure 4.1(c) is the same for both the feed-forward and feedback control, the philosophy of the noise cancellation is different. For the feed-forward active control system in Figure 4.1(a), the noise reduction is achieved by




(a)




(b)




(c)

Figure 4.1 Block diagram of the active control system: (a) feed-forward; (b) feedback; (c) unified diagram from the viewpoint of adaptive filtering.

modeling the unknown plant $P$ with the control filter $W$. Hence, the performance depends on how well the unknown plant $P$ can be modeled by a linear digital filter. For the feedback control system in Figure 4.1(b), the primary disturbance is reduced by adaptive prediction. Consequently, the performance depends on the predictability of the primary disturbance filtered by the estimate of the secondary path transfer function, $\hat{S}(z)$. Besides, the accuracy of representing $S(z)$ by $\hat{S}(z)$ will also affect the overall performance.

Figure 4.2 shows the sub-band adaptive filter structure where the ideal signal $d(n)$ is accessible. Since the ideal signal $d(n)$ in the active noise or vibration control systems is not available or accessible, the sub-band structure used for system identification or echo cancellation shown in Figure 4.2 cannot be applied to the active control systems. Furthermore, the active control system generally cannot tolerate extra delay along the signal path, especially for the feedback control system. This is because the performance of the feedback active control system depends on the predictability of the primary disturbance filtered by the estimated secondary path transfer function. Any delay along the signal path will increase the requirement of the forward prediction and hence, dramatically degrade the performance [13].

To avoid the signal path delay, this dissertation proposes a delayless sub-band architecture shown in Figure 4.3, which updates the full-band filter coefficients based on the sub-band reference signals and sub-band error signals. To derive an adaptive algorithm that updates the full-band weight vector based on the sub-band error signals requires a new cost function that can be determined from the sub-band error signals. We define the new cost function as the sum of the mean square of the sub-band errors as

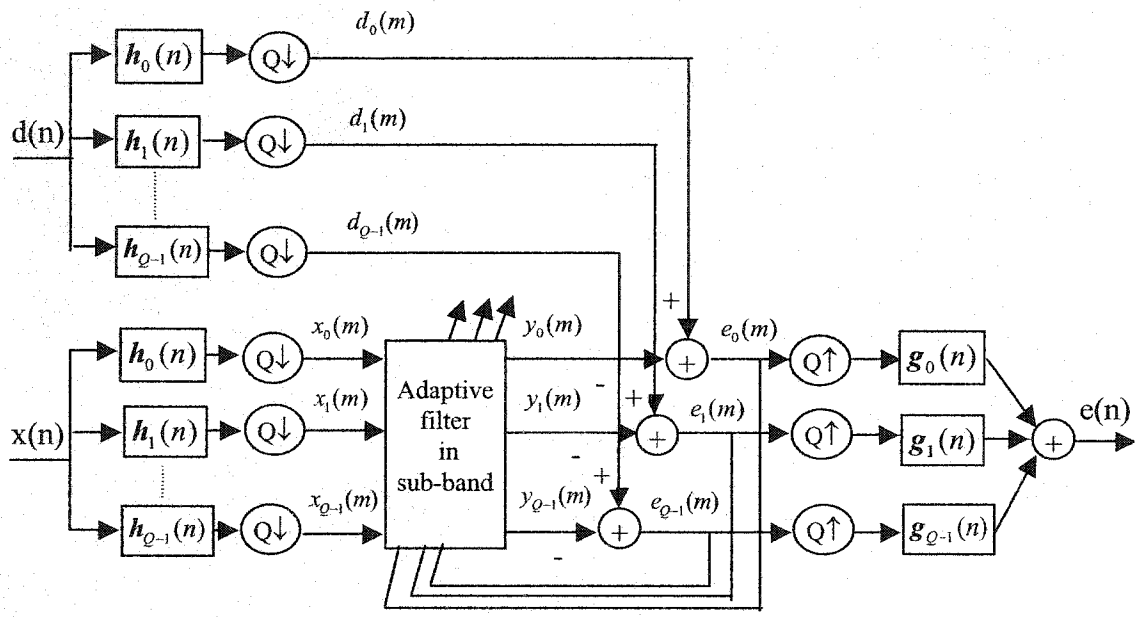



Figure 4.2 Sub-band adaptive filter structure used in system identification or echo cancellation where the ideal signal is accessible.

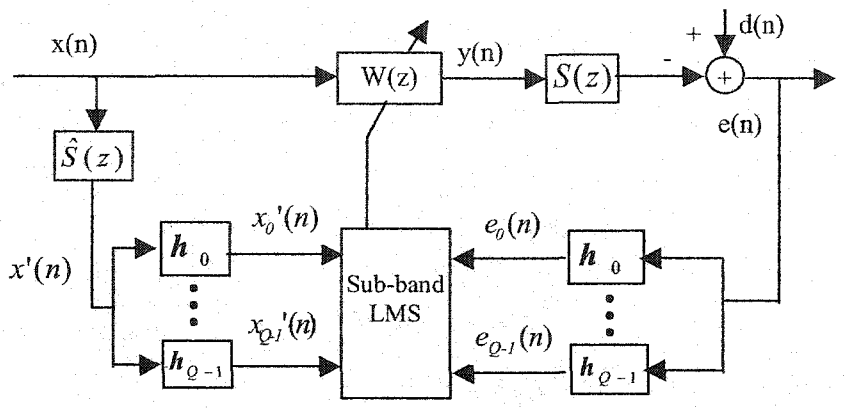



Figure 4.3 The sub-band adaptive filter architecture without signal path delay.

$$\xi_{sub}(n) = \sum_{q=0}^{Q-1} E\{|e_q(n)|^2\}, \tag{4.1}$$

where $Q$ is the number of sub-bands. The residual error signal in sub-band $q$ is designated as $e_q(n) = \boldsymbol{h}_q^T \boldsymbol{e}(n)$. $\boldsymbol{e}(n) = [e(n), e(n-1), \cdots, e(n-L)]$, is the full-band residual error. $L$ is the order of the analysis filter $\boldsymbol{h}_q = h_q(0)\delta(n) + h_q(1)\delta(n-1) + \cdots + h_q(L)\delta(n-L)$. $E\{.\}$ is the expectation operator. Provided that the analysis filter bank satisfies the power complementary property, *i.e.*, provided $\sum_{q=0}^{Q-1} |H_q(e^{j\omega})|^2 = c$, minimizing the new cost function is equivalent to minimizing the mean square of the full-band error, $E\{|e(n)|^2\}$. This can be justified using the property that the power spectrum of the output signal is the power spectrum of the input signal modified by the filter spectrum. That is, let $S_e(\omega)$ denote the power

spectrum of the full-band error signal e(n) and let $S_{e_q}(\omega)$ denote the power spectrum of $e_q(n)$, the error signal in sub-band $q$. Then,

$$\sum_{q=0}^{Q-1} E\{|e_q(n)|^2\} = \sum_{q=0}^{Q-1} \frac{1}{2\pi} \int_{-\pi}^{\pi} S_{e_q}(\omega) d\omega$$

$$= \sum_{q=0}^{Q-1} \frac{1}{2\pi} \int_{-\pi}^{\pi} S_e(\omega) |H_q(e^{j\omega})|^2 d\omega$$

$$= \frac{1}{2\pi} \int_{-\pi}^{\pi} S_e(\omega) \sum_{q=0}^{Q-1} |H_q(e^{j\omega})|^2 d\omega$$

$$= c \frac{1}{2\pi} \int_{-\pi}^{\pi} S_e(\omega) d\omega = cE\{|e(n)|^2\}. \quad (4.2)$$

The weight updating equation for the sub-band adaptive filter shown in Figure 4.3 is derived as follows.

The full-band error signal at time instant $n$ in Figure 4.3 is

$$e(n) = d(n) - \sum_{j=0}^{J} \sum_{k=0}^{K} x(n-j-k) w_{n-k}(j) s(k), \quad (4.3)$$

where $J$ is the order of the control filer $W(z)$ and $K$ is the length of the MA transfer function $S(z)$. The residual error signal in sub-band $q$ at time instant $n$ is

$$e_q(n) = \boldsymbol{h}_q^T \boldsymbol{e}(n) = \sum_{l=0}^{L} d(n-l) h_q(l) - \sum_{j=0}^{J} \sum_{k=0}^{K} \sum_{l=0}^{L} x(n-j-k-l) w_{n-k-l}(j) s(k) h_q(l),$$

$$q=0,1,...,Q-1. \quad (4.4)$$

The full-band filter coefficients are updated to minimize the sum of the instantaneous square of the sub-band errors, *i.e.*, $\sum_{q=0}^{Q-1} e_q^2(n)$. Thus, the stochastic gradient algorithm for updating $w_n(i)$ at time instant $n$ is

$$w_{n+1}(i) = w_n(i) - \mu \frac{\partial}{\partial w_n(i)} \sum_{q=0}^{Q-1} e_q{}^2(n)$$

$$= w_n(i) - 2\mu \sum_{q=0}^{Q-1} e_q(n) \frac{\partial e_q(n)}{\partial w_n(i)}, \; i = 0,1,...,J, \tag{4.5}$$

where $\mu$ is the step size that determines the speed of adaptation. Substitution of Equation (4.4) into Equation (4.5) yields the update recursion

$$w_{n+1}(i) = w_n(i) + 2\mu \sum_{q=0}^{Q-1} e_q(n) \frac{\partial}{\partial w_n(i)} \sum_{j=0}^{J} \sum_{k=0}^{K} \sum_{l=0}^{L} x(n-j-k-l) w_{n-k-l}(j) s(k) h_q(l),$$

$$i = 0,1,...,J. \tag{4.6}$$

If we assume $w_{n-k-l}(i) = w_n(i)$ for all $k$ and $l$, then Equation (4.6) can be evaluated as

$$w_{n+1}(i) = w_n(i) + 2\mu \sum_{q=0}^{Q-1} e_q(n) \sum_{k=0}^{K} \sum_{l=0}^{L} x(n-i-k-l) s(k) h_q(l), \; i = 0,1,...,J. \tag{4.7}$$

It is assumed that $S(z)$ can be estimated accurately in the discussion. That is, $S(z) = \hat{S}(z)$. Let us denote the reference signal filtered by $\hat{S}(z)$ as $x'(n)$, *i.e.*,

$$x'(n) = \sum_{k=0}^{K} x(n-k) \hat{s}(k) \tag{4.8}$$

and $x'(n)$ in sub-band $q$ as $x'_q(n)$, *i.e.*,

$$x'_q(n) = \sum_{k=0}^{K} \sum_{l=0}^{L} x(n-k-l) \hat{s}(k) h_q(l), \; q = 0,1,...,Q-1. \tag{4.9}$$

Then, the updating recursion can be simplified by substituting Equation (4.9) into Equation (4.7) as

$$w_{n+1}(i) = w_n(i) + 2\mu \sum_{q=0}^{Q-1} e_q(n) x'_q(n-i), \; i = 0,1,...,J. \tag{4.10}$$

It should be noted that the assumption of $w_{n-k-l}(i) = w_n(i)$ for all $k$ and $l$ used to derive the update recursion is not strictly correct because of the time-varying nature of the adaptive filter. Hence, the adaptation given by Equation (4.7) or (4.10) may not always converge. This assumption can only be justified if the time-varying nature of the adaptive filter is a slow rate or when the time delay associated with the secondary path transfer function and the analysis filter bank is negligible.

## 4.2 Increasing the convergence region of the step size

The advantage of the sub-band adaptive filter derived in Section 4.1 is that it has the flexibility to assign different step sizes to different sub-bands based on the proportionate signal energy present in each sub-band. Hence, a better convergence rate results when the algorithm is compared to the full-band counterpart. On the other hand, the analysis filter bank used to decompose the full band signal does bring extra delay into the error path. Long ([34], [35]) showed that the delay in the error path has only a slight influence on the steady-state behavior of the LMS algorithm when the step size in the coefficient updating is within a certain bound. However, the delay in the error path reduces the convergence region of the step size. For a full-band FXLMS algorithm, the error path delay only comes from the secondary path transfer function *S(z)*. For the sub-band FXLMS algorithm proposed in this work, the error path delay comes from both *S(z)* and the analysis filter bank. In general, it is very difficult to examine the stability of the FXLMS algorithm. Snyder [36] derived the region of $\mu$ in the full-band FXLMS that makes the controllers stable in a specific case where the secondary path is a pure $k$-step sample delay and the signals are assumed to be stationary as follows:

$$0 < \mu < (1/\lambda_{\max})\sin[\pi/2(2k+1)]. \tag{4.11}$$

Here, $\lambda_{\max}$ is the maximum eigenvalue of the autocorrelation matrix of the reference input signal. Kim [37] proposed a constrained filtered-x algorithm to compensate for the error path delay in the full-band LMS. We now derive the compensation methods for our proposed sub-band FXLMS algorithm.

Notice the expression for the error signal in sub-band $q$ in Equation (4.4). At the time instant $n$ when $\boldsymbol{W}_n$ is already available, $e_q(n)$ is still based on the old coefficients, $\boldsymbol{W}_{n-k-l}$, due to the error path delay resulting from *S(z)* and the analysis filter bank. It is these old coefficients that result in the decrease of the convergence region. If we generate a different set of sub-band error signals $\hat{\varepsilon}_q(n)$ by replacing $w_{n-k-l}(j)$ with $w_{n-k}(j)$ in Equation (4.4), that is,

$$\hat{\varepsilon}_q(n) = \sum_{l=0}^{L} d(n-l)h_q(l) - \sum_{j=0}^{J}\sum_{k=0}^{K}\sum_{l=0}^{L} x(n-j-k-l)w_{n-k}(j)\hat{s}(k)h_q(l),\ q = 0,1,...,Q-1 \tag{4.12}$$

and replace $e_q(n)$ in Equation (4.10) with $\hat{\varepsilon}_q(n)$ to update the weights, *i.e.*,

$$w_{n+1}(i) = w_n(i) + 2\mu\sum_{q=0}^{Q-1}\hat{\varepsilon}_q(n)x'_q(n-i),\ i = 0,1,...,J, \tag{4.13}$$

then the delay resulting from the analysis filter bank has been compensated. Further, if we generate another set of sub-band errors $\tilde{\varepsilon}_q(n)$ by replacing $w_{n-k-l}(j)$ with $w_n(j)$ in Equation (4.4), that is

$$\tilde{\varepsilon}_q(n) = \sum_{l=0}^{L} d(n-l)h_q(l) - \sum_{j=0}^{J}\sum_{k=0}^{K}\sum_{l=0}^{L} x(n-j-k-l)w_n(j)\hat{s}(k)h_q(l),\ q = 0,1,...,Q-1 \tag{4.14}$$

and update the filter coefficients using $\tilde{\varepsilon}_q(n)$ as

$$w_{n+1}(i) = w_n(i) + 2\mu \sum_{q=0}^{Q-1} \tilde{\varepsilon}_q(n) x'_q(n-i),\ i = 0,1,...,J, \tag{4.15}$$

then the error path delay resulting from $S(z)$ and the analysis filter bank has been compensated.

$\hat{\varepsilon}_q(n)$ and $\tilde{\varepsilon}_q(n)$ are not directly available but can be derived from $e_q(n)$ and other known signals. Comparing Equation (4.4) to Equation (4.12), we have

$$\begin{aligned}\hat{\varepsilon}_q(n) &= e_q(n) + \sum_{j=0}^{J}\sum_{k=0}^{K}\sum_{l=0}^{L} x(n-j-k-l) w_{n-k-l}(j) \hat{s}(k) h_q(l) \\ &\quad - \sum_{j=0}^{J}\sum_{k=0}^{K}\sum_{l=0}^{L} x(n-j-k-l) w_{n-k}(j) \hat{s}(k) h_q(l) \\ &= e_q(n) + \sum_{k=0}^{K}\sum_{l=1}^{L} y(n-k-l) \hat{s}(k) h_q(l) \\ &\quad - \sum_{j=0}^{J}\sum_{k=0}^{K}\sum_{l=1}^{L} x(n-j-k-l) w_{n-k}(j) \hat{s}(k) h_q(l),\ q = 0,1,...,Q-1,\end{aligned} \tag{4.16}$$

where $y(n-k-l) = \sum_{j=0}^{J} x(n-j-k-l) w_{n-k-l}(j)$ is the output of the controller at time instant *n-k-l*.

Similarly, comparing Equation (4.4) to Equation (4.14) enables $\tilde{\varepsilon}_q(n)$ to be given as

$$\begin{aligned}\tilde{\varepsilon}_q(n) &= e_q(n) + \sum_{j=0}^{J}\sum_{k=0}^{K}\sum_{l=0}^{L} x(n-j-k-l) w_{n-k-l}(j) \hat{s}(k) h_q(l) \\ &\quad - \sum_{j=0}^{J}\sum_{k=0}^{K}\sum_{l=0}^{L} x(n-j-k-l) w_n(j) \hat{s}(k) h_q(l) \\ &= e_q(n) + \sum_{k=0}^{K}\sum_{l=0}^{L} y(n-k-l) \hat{s}(k) h_q(l)\end{aligned}$$

$$-\sum_{j=0}^{J}\sum_{k=0}^{K}\sum_{l=0}^{L} x(n-j-k-l)w_n(j)\hat{s}(k)h_q(l),\ q=0,1,...,Q-1. \qquad (4.17)$$

We refer to our approach, shown in Equations (4.13) and (4.16), as delay compensation method I. This method compensates the error path delay resulting from the analysis filter bank only. We refer to our approach, shown in Equations (4.15) and (4.17), as delay compensation method II. This method compensates the error path delay resulting from both the analysis filter bank and the secondary path transfer function. The efficiency of the delay compensation methods will be illustrated in the next section by computer simulations.

## 4.3 Computer Simulations

Computer simulations are performed to illustrate the efficiency of the proposed sub-band algorithm, for both the feed-forward control and the feedback control systems. Throughout the simulations, only a 2-band case is considered using an $8^{th}$-order Daubechies filter as the base filter of the analysis filter bank.

### 4.3.1 Feed-forward active control system

To simulate the feed-forward active control system shown in Figure 2.2 on page 7, the same example used in [37] is adopted. That is, the reference input signal *x(n)* is a white noise process with uniform distribution with zero mean and unit variance. The plant *P(z)* is assumed to be a fourth order FIR filter as $P(z) = 1.0z^{-2} - 0.3z^{-3} + 0.2z^{-4}$. *S(z)* was assumed to be a unit gain system and *R(z)* was assumed to be a pure 5-sample delay for simplicity. Since the control filter *W* models the plant *P* in the feed-forward

control system, coefficients of the controller need to converge to the optimal value, $W^*(z) = 1.0z^{-2} - 0.3z^{-3} + 0.2z^{-4}$.

The proposed sub-band adaptive filter can achieve a better convergence rate by assigning different step sizes to different sub-bands. The typical one is the normalized FXLMS. For the full-band FXLMS, the step size is normalized as $\mu_f = \frac{2\mu}{\|\boldsymbol{x}'\|^2 + \delta}$, $0 < \delta << 1$ and $\boldsymbol{x}' = [x'(n), x'(n-1), \cdots, x'(n-J)]$. For the sub-band FXLMS, the step size in sub-band $q$ is normalized as $\mu_q = \frac{2\mu}{\|\boldsymbol{x}'_q\|^2 + \delta}$, $q=0,1,...,Q-1$, and $\boldsymbol{x}'_q = [x'_q(n), x'_q(n-1), \cdots, x'_q(n-J)]$. To compare the performance fairly, all the parameters are set to be the same for the Full-band FXLMS and the Sub-band FXLMS. The step size $\mu$ is set to 0.06 for both cases such that the weight vector converges to its optimal value within several hundred samples. Figure 4.4 shows the trajectories of the FIR filter coefficients $\boldsymbol{w}$ with the initial values set to zero. The sub-band filter outperforms the full-band counterpart, because it has the flexibility to normalize the step size in each sub-band separately.

The performances of the sub-band FXLMS algorithms, shown in Figure 4.5, are similar when the step size for the coefficient update is within certain bounds. The merit of the delay compensation methods is that they restore the convergence region of the step size decreased by the secondary path transfer function and the analysis filter bank. Figure 4.6 through Figure 4.9 show the effects of the error path delay on the convergence region of the step size and illustrate the efficiency of delay compensation. The FXLMS rather than the normalized FXLMS is employed in Figure 4.6 through

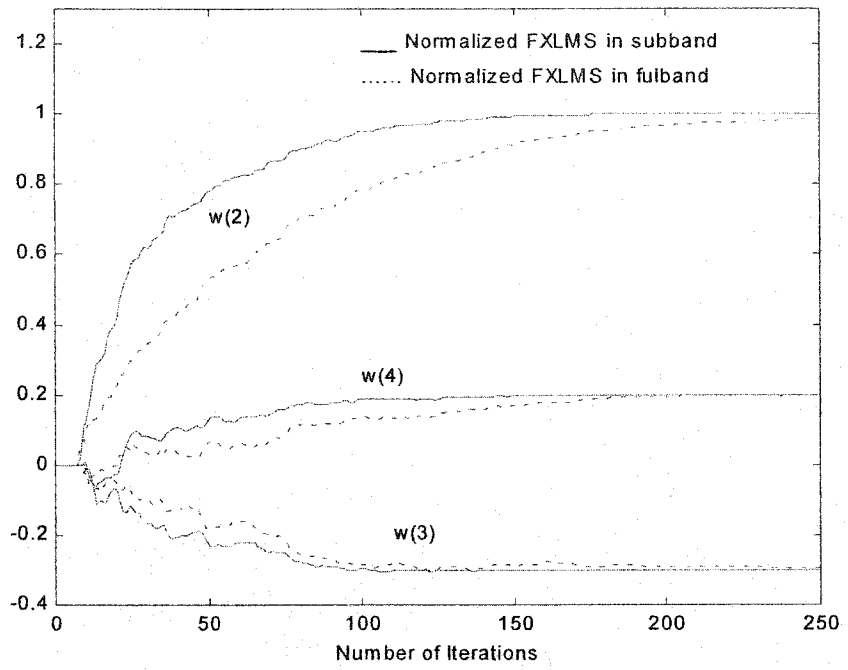



Figure 4.4 Trajectories of $w$ using the normalized FXLMS in full-band (dotted line) and in sub-band (solid line) with the step size $\mu$=0.06.

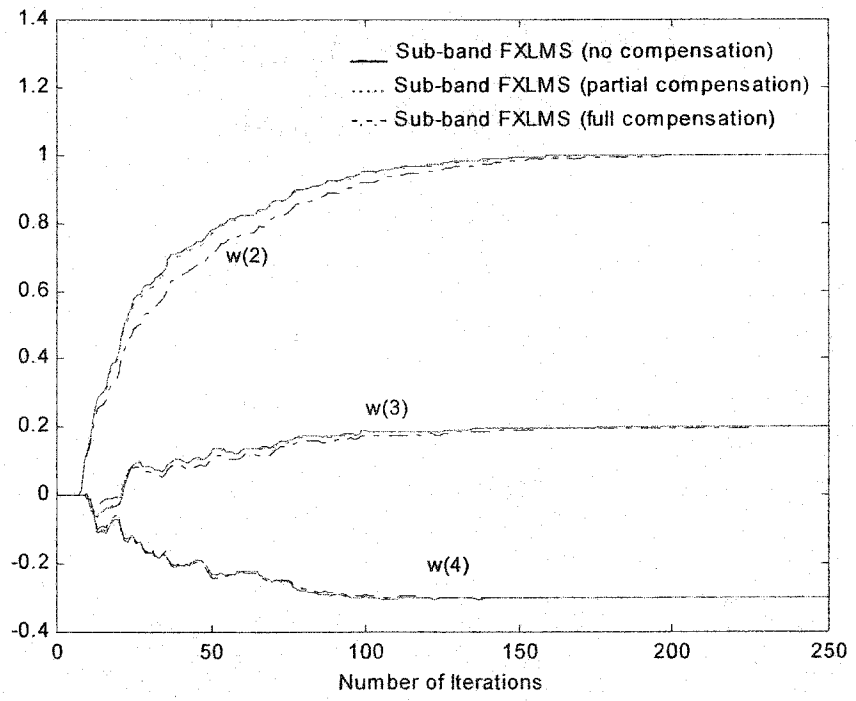



Figure 4.5 Trajectories of $w$ using the sub-band FXLMS without delay compensation and with delay compensation by method I and by method II ($\mu$=0.06).

Figure 4.9 to exclude the effect of normalization. In particular, Figure 4.6 shows the trajectories of the magnitude of the full-band error and the filter coefficients with the full-band FXLMS where the step size $\mu$ is selected as 0.05, so that obvious variance occurs when the filter coefficients converge. Figure 4.7 shows the same information for the sub-band FXLMS without delay compensation. Since the group delay of the analysis filter bank reduces the convergence region of the step size, the trajectories show more variance under the same step size. Figure 4.8 shows the trajectories of |e(n)| and $\boldsymbol{w}$ of the sub-band FXLMS with delay compensation by method I. The variance is similar to that in Figure 4.6, because method I only compensates the error path delay resulting from the analysis filter bank. Figure 4.9 shows the same information of the sub-band FXLMS with full delay compensation by method II. Method II compensates not only the error path delay resulting from the analysis filter but also the error path delay resulting from the secondary path transfer function. Hence, it increases the convergence region of the step size compared to the full-band FXLMS algorithm. Consequently, the trajectories of the filter coefficients compensated by method II show very slight variance under the same step size.

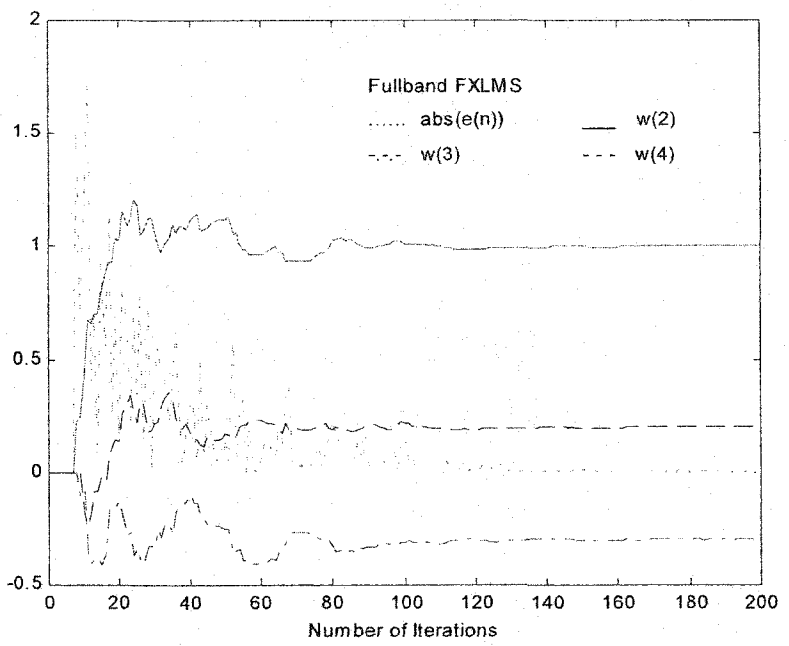



Figure 4.6 Trajectories of the magnitude of the full-band error |e(n)| and the filter coefficients using the full-band FXLMS with $\mu$=0.05.

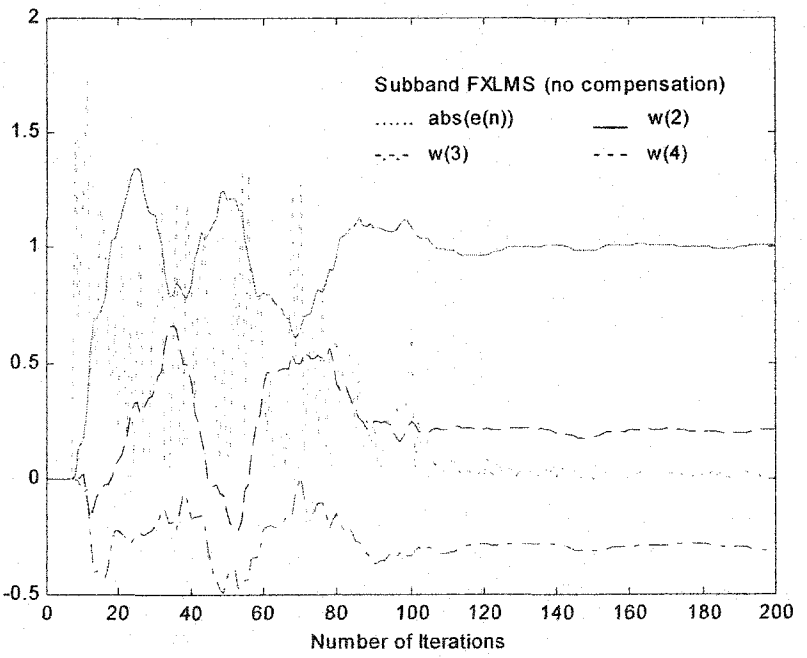



Figure 4.7 Trajectories of the magnitude of the full-band error |e(n)| and the filter coefficients using the sub-band FXLMS (no delay compensation) with $\mu$=0.05.

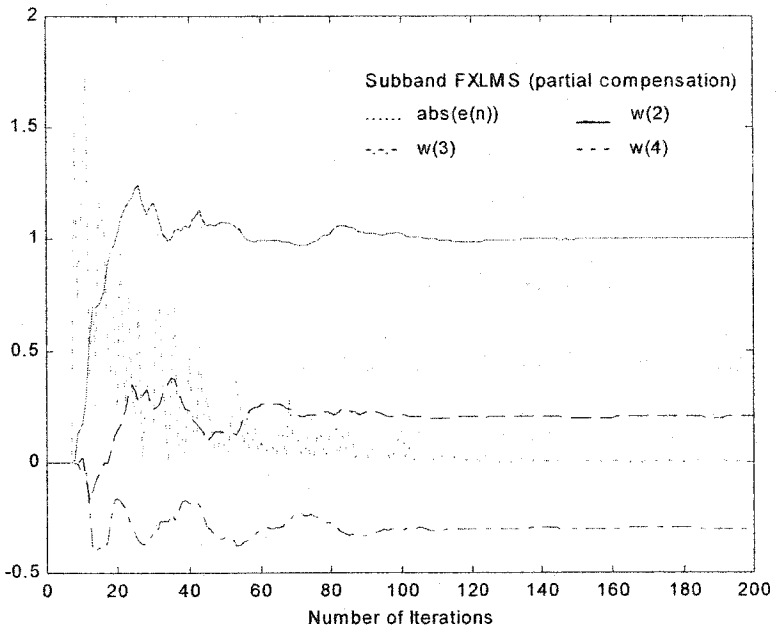



Figure 4.8 Trajectories of the magnitude of the full-band error |e(n)| and the filter coefficients using the sub-band FXLMS (partial delay compensation by method I) with $\mu$=0.05.

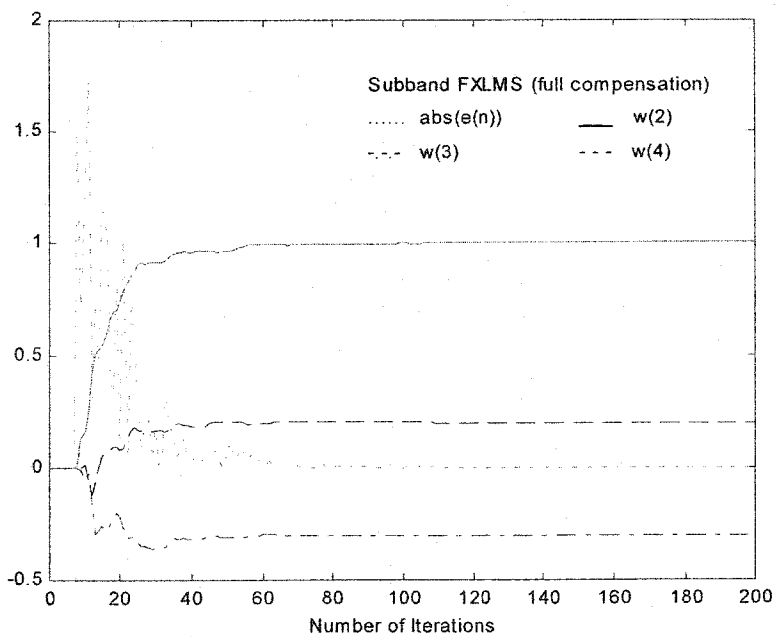



Figure 4.9 Trajectories of the magnitude of the full-band error |e(n)| and the filter coefficients using the sub-band FXLMS (full delay compensation by method II) with $\mu$=0.05.

### 4.3.2 Feedback active control system with an AR(2) process

To simulate the performance for the feedback control system shown in Figure 2.5 on page 12, a unit variance *AR(2)* process in [13] is adopted as the primary disturbance *d(n)*, where $a_1 = -0.975$, $a_2 = 0.95$ and the eigenvalue spread equals 3. Note that the feedback control system (shown in Figure 2.5) is equivalent to a one-step forward prediction error filter even when *S(z)* is a unit gain system. This is because the error signal *e(n)* is obtained first at each time instant, then the primary disturbance *d(n)* is restored to serve as the reference signal *x(n)*. Figure 4.10 shows the learning curves of the normalized FXLMS in the full-band and sub-band algorithms when $\mu$=0.02 and *S(z)* is a unit gain system. Again, the algorithms implemented in the sub-band outperform the algorithm implemented in full-band because they can normalize the step size in each sub-band separately. All the ensemble averaging in this section is performed over 100 independent trails of the experiments.

Figures 4.11 through Figure 4.13 show the effects of error path delay on the convergence region of the step size and illustrate the efficiency of the delay compensation methods when *S(z)* is assumed to be a 5 sample delay. The step size $\mu$ is chosen as 0.013 (no normalization) so that the learning curve of the full-band FXLMS shows large variance, as shown by the dotted line in Figure 4.11. The learning curve of the sub-band FXLMS with the same step size shows larger variance (the solid line in Figure 4.11) because of the extra error path delay added by the analysis filter bank. The dotted line in Figure 4.12 shows the learning curve of the sub-band FXLMS compensated by the delay compensation method I. The variance of the learning curve is

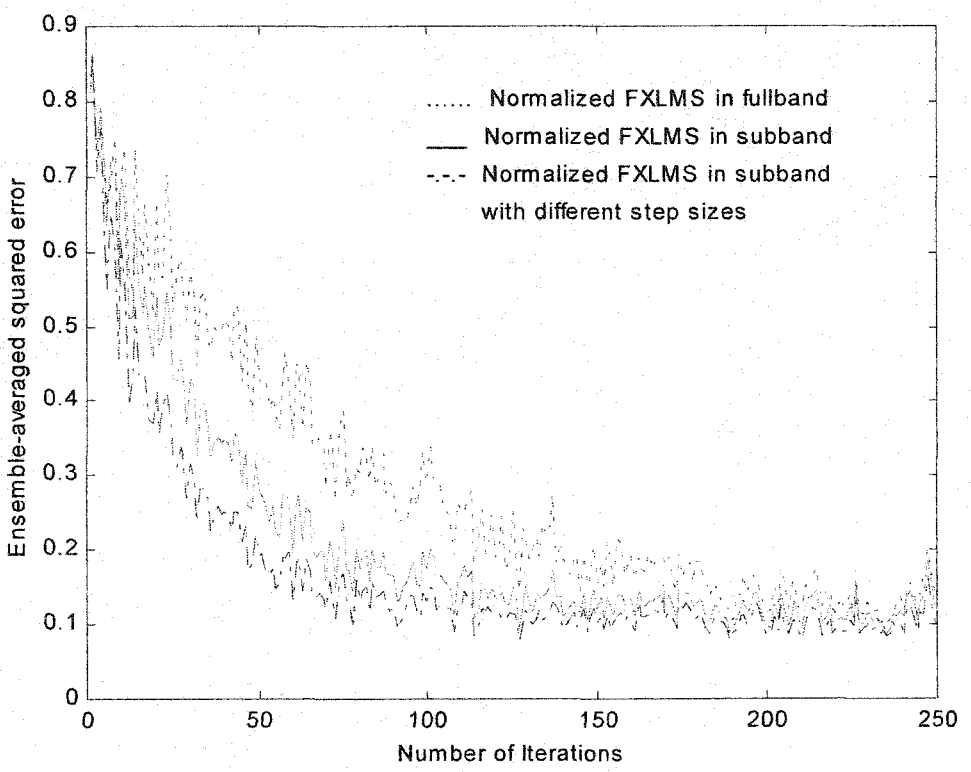



Figure 4.10 Experimental learning curves of the normalized FXLMS in full-band (dotted line) and in sub-band (solid line) with $\mu$=0.02. The dashdot line shows the learning curve of the sub-band FXLMS when the step size of the low-frequency sub-band is doubled and the step size of the high-frequency sub-band is reduced to its half value.

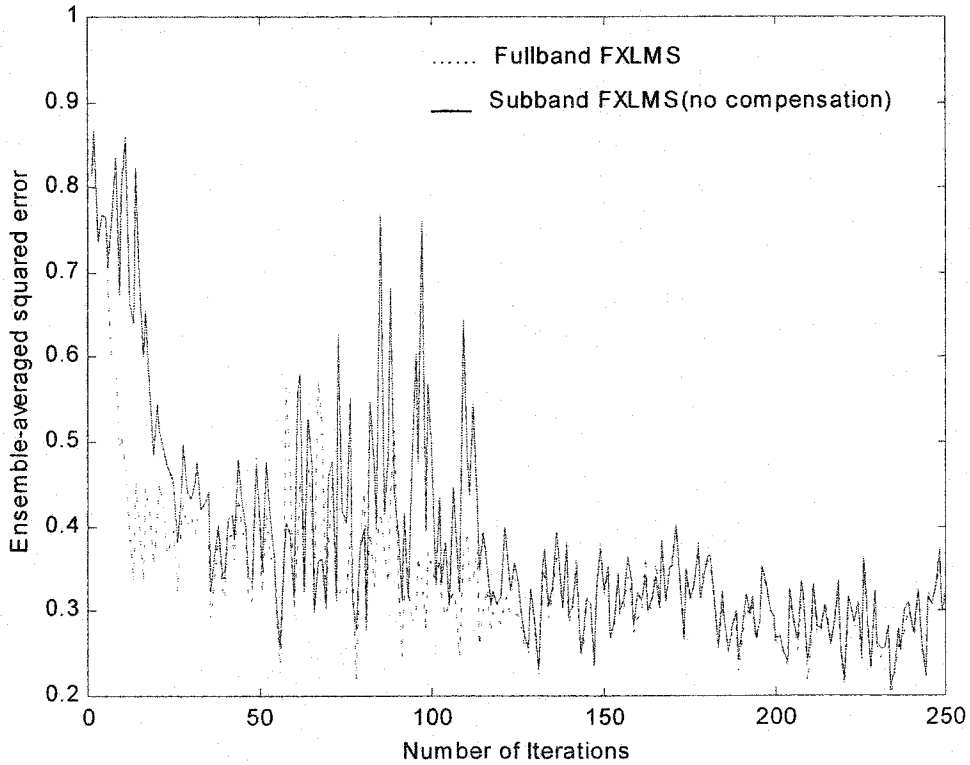



Figure 4.11 Learning curves of the FXLMS in full-band (dotted line) and in sub-band (solid line) with $\mu$=0.013. *S(z)* is assumed to be a pure 5 sample delay.

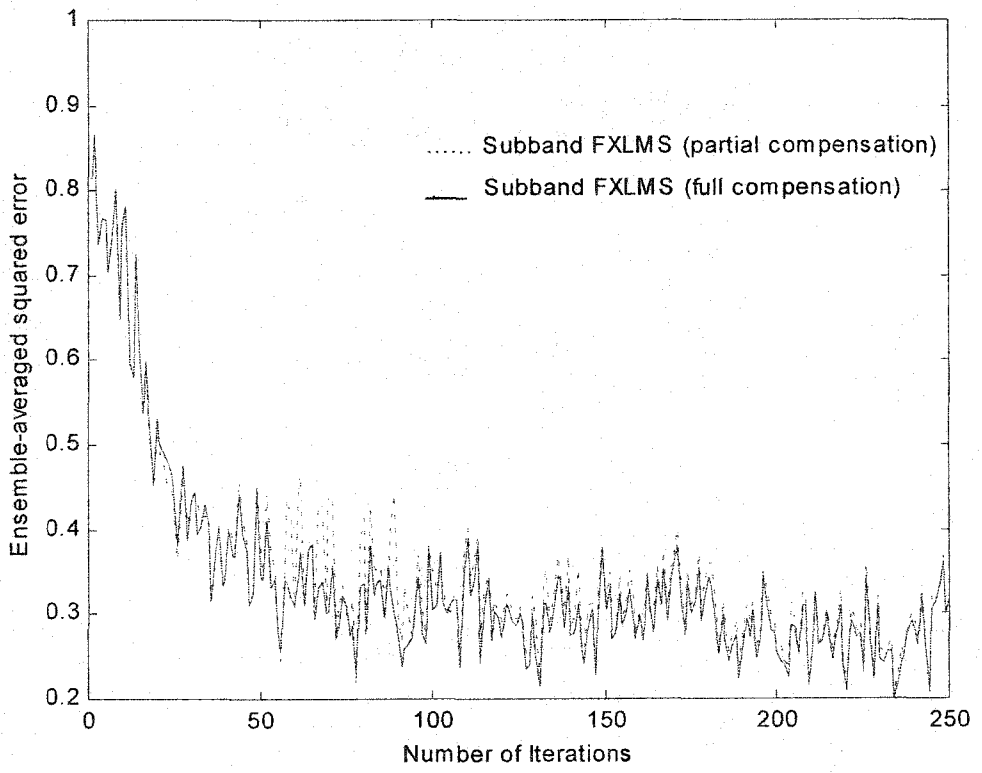



Figure 4.12 Learning curves of the FXLMS in sub-band with partial delay compensation by method I (dotted line) and full delay compensation by method II (solid line) ($\mu$=0.013).

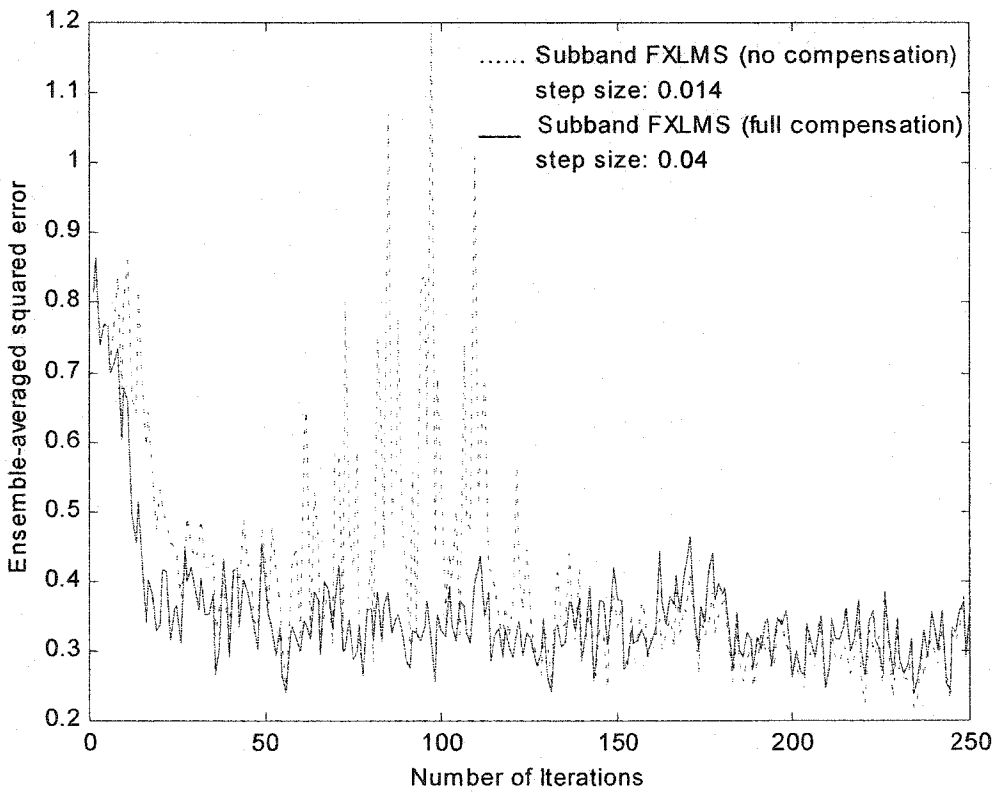



Figure 4.13 Learning curves of the FXLMS in sub-band without delay compensation at $\mu$=0.014 (dotted line) and with delay compensation by method II at $\mu$=0.04 (solid line)

decreased compared to the one without delay compensation. The solid line in Figure 4.12 shows the learning curve of the sub-band FXLMS when the delay compensation method II is used to compensate the error path delay resulting from the analysis filter bank and *S(z)*. The variance is much smaller with the same step size $\mu$=0.013. Actually, the critical step size of the sub-band FXLMS after delay compensation with method II can go as far as $\mu$=0.04 (the solid line in Figure 4.13), while $\mu$=0.014 is unacceptable for the sub-band FXLMS without delay compensation (the dotted line in Figure 4.13). These simulations verify the better convergence performance the sub-band FXLMS can achieve when compared to its full-band counterpart and the efficiency of the delay compensation methods.

### 4.3.3 Feedback active control system with the real vibration signals

The sub-band FXLMS algorithm is also applied to the HDD vibration control case to see the performance improvement. Again, the extra computational requirements associated with the signal decomposition and weight updating reduce the sampling rate in real time. To compare the performance fairly, simulations are performed to compare the performances of the full-band FXLMS and the sub-band FXLMS in reducing the vibration sampled at 16 *kHz*. Figure 4.14 gives the average power spectrum density of the original vibration in 0.5 seconds (*i.e.,* 8000 samples), and the power spectrum densities when the active control systems using the full-band FXLMS and the sub-band FXLMS are operating. It can be seen that the sub-band method outperforms the full-band method slightly on the vibration reduction in the destructive interference range. Another merit of the sub-band algorithm is that it has the flexibility to trade-off the

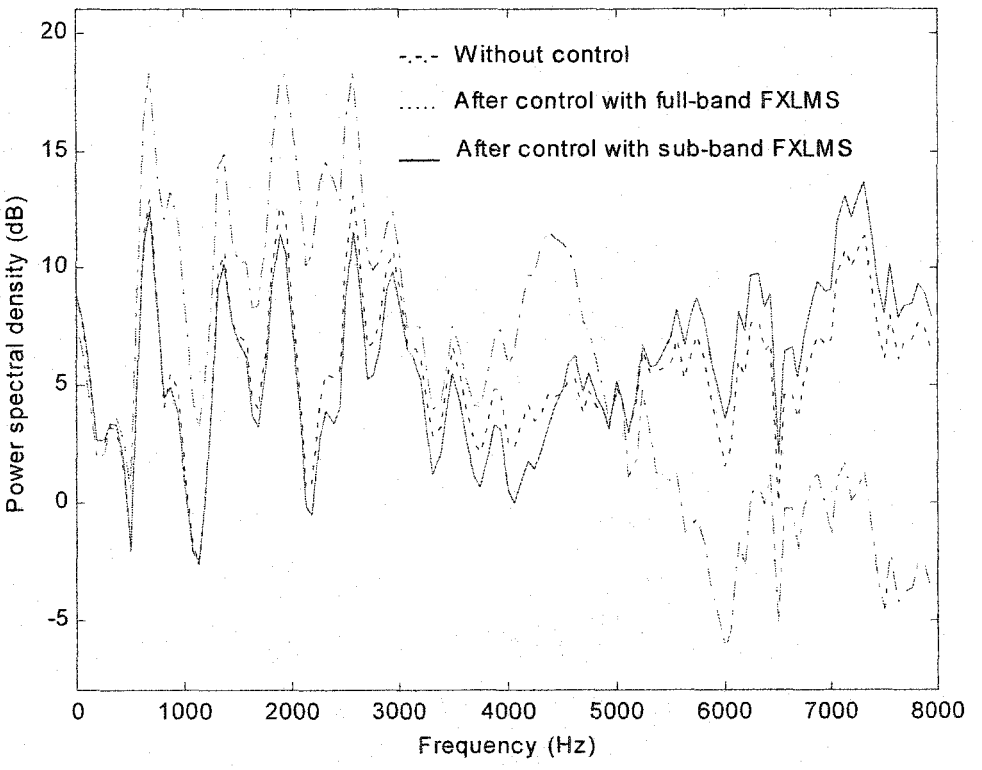



Figure 4.14 Simulation result of vibration reduction using the full-band FXLMS (dotted line) and sub-band FXLMS (solid line) with the real vibration signal sampled at 16 *kHz*.

performance from the various sub-bands. To look at this merit experimentally, let us assume that the secondary path S(z) is a pure one-sample delay. Then, the adaptive feedback control system is equivalent to an adaptive forward prediction-error filter. Consequently, the filter weight $w_k$ converges to $-a_k$ of an *AR(N)* process. This *AR(N)* process models the original disturbance in the sense of minimizing the mean square error. Since the vibration reduction of a feedback control system depends on the predictability of the original vibration, the better the original disturbance can be modeled the more the vibration can be reduced. If the vibration reduction in one specific frequency sub-band interests the users more, more weight can be put to that sub-band in the full-band weight vector updating step. Doing so, the filter weight $w_k$ converges to $-a_k$ of a new *AR(N)* process and this new *AR(N)* process models the original disturbance more accurately in the sub-band that interests the users. Figure 4.15 shows the change of the magnitude responses of the resulting *AR(N)* processes in a 2 sub-band case when the weight is put to the low frequency sub-band. When more weight is put to the low frequency band, the resulting *AR(N)* process models the low frequency band more accurately at the cost of modeling the high frequency band less accurately. The dashed line shows the extreme case where the full-band controller vector is updated using the low frequency band reference signal and low frequency band error signal only. Figure 4.16 shows the opposite scenario when more weight is given to the high frequency band. It can be seen that the more weighting placed on the high frequency band, the better the resulted *AR(N)* process models the original disturbance in the high frequency band. The dashed line shows the extreme case where

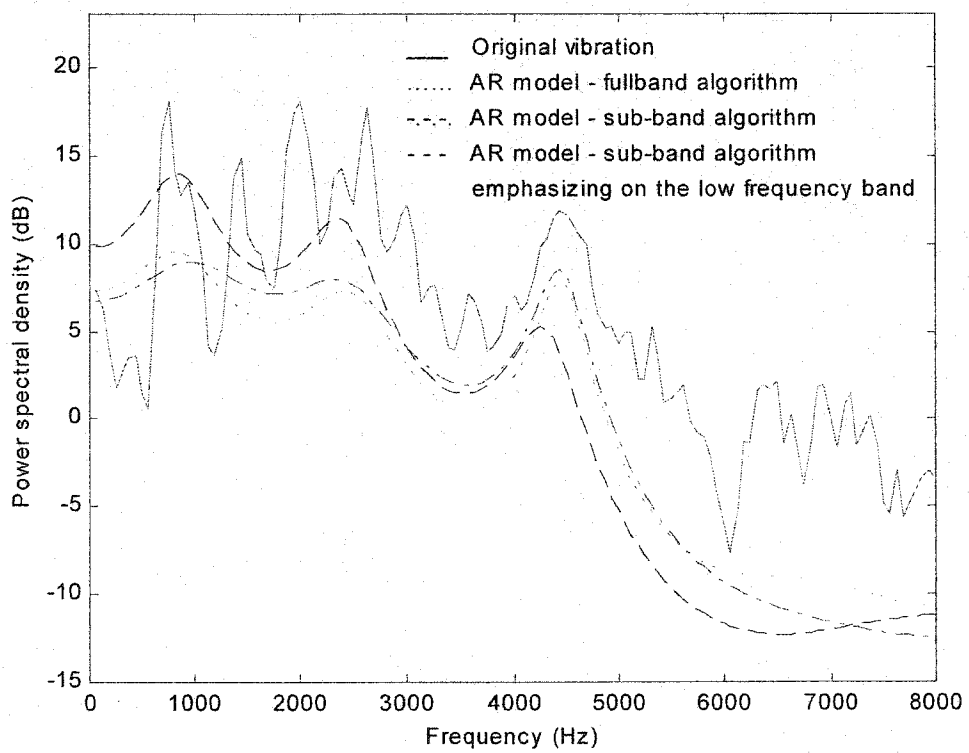



Figure 4.15 Magnitude responses of the *AR(N)* processes resulting from the controller vector with and without putting more weight to the low frequency band.

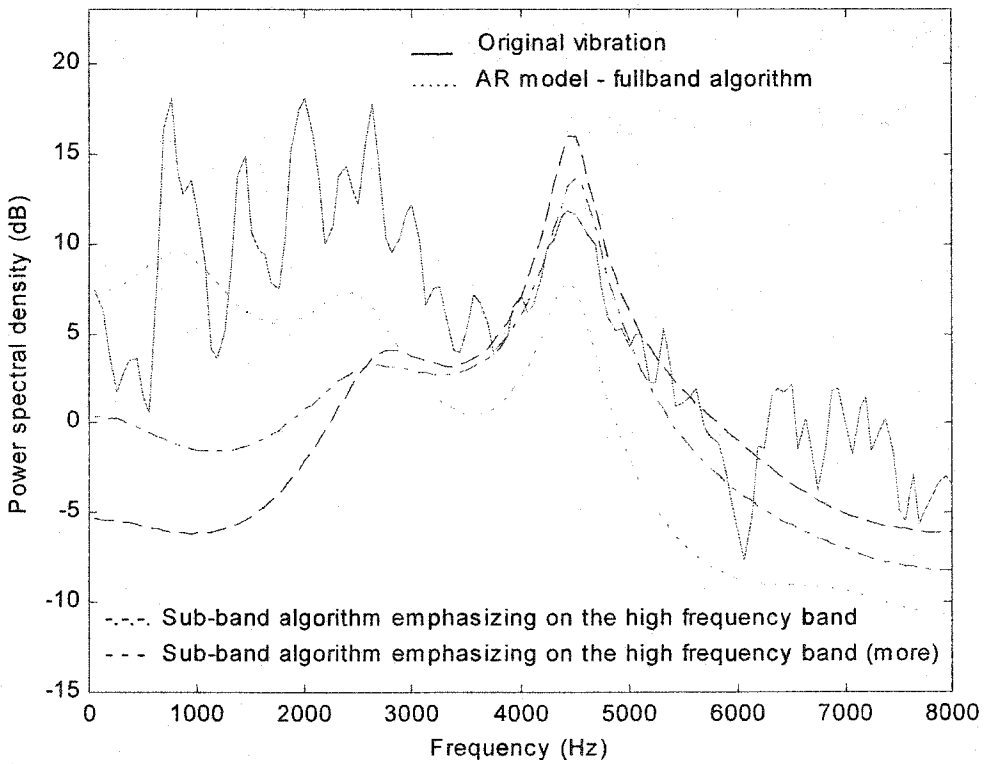



Figure 4.16 Magnitude responses of the *AR(N)* processes resulting from the controller vector when more weight is put to the high frequency band.

the full-band controller vector is updated using the high frequency band reference signal and high frequency band error signal only. Figure 4.17 shows the vibration reduction of these two extreme cases. It can be seen that more vibration reduction is achieved at the lower frequencies, but more constructive interference occurs at the higher frequencies when the controller vector is updated using only the low frequency sub-band signals. Similarly, more vibration reduction is achieved at the higher frequencies (or at least less constructive interference occurs at the higher frequencies), but no vibration reduction is achieved at the lower frequencies when the controller vector is updated using only the higher frequency sub-band signals.

## 4.4 Combining the frequency domain technique with the sub-band architecture

When we use the sub-band algorithm to concentrate on the reduction of the vibration at the low frequencies, more constructive interference occurs at the higher frequencies as shown by the dotted line in Figure 4.17. To reduce the constructive interference at the higher frequencies while keeping or improving the destructive interference performance at the lower frequencies, we can combine the frequency domain technique with the sub-band decomposition structure as shown in Figure 4.18. Here, $x_q'(n)$ is the filtered reference signal in sub-band $q$ and $X_q'$ is its counterpart in the transform domain. Then, the selective adaptation technique proposed in Chapter 3 can be applied to alleviate the constructive interference. Figure 4.19 compares the performances of the frequency domain LMS with the combined frequency domain/sub-band algorithm when the selective adaptation technique is used to alleviate the

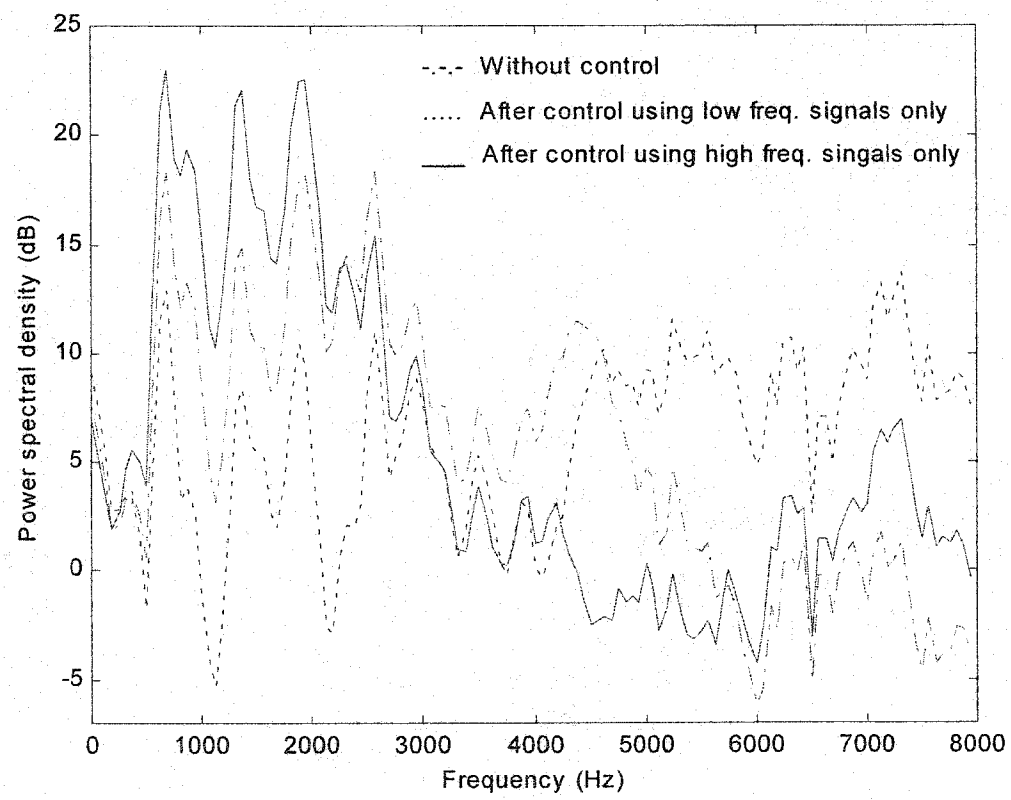



Figure 4.17 Simulation result of the sub-band FXLMS algorithm when the weight vector is updated using the low frequency band signals only (dotted line) and using the high frequency band signals only (solid line).

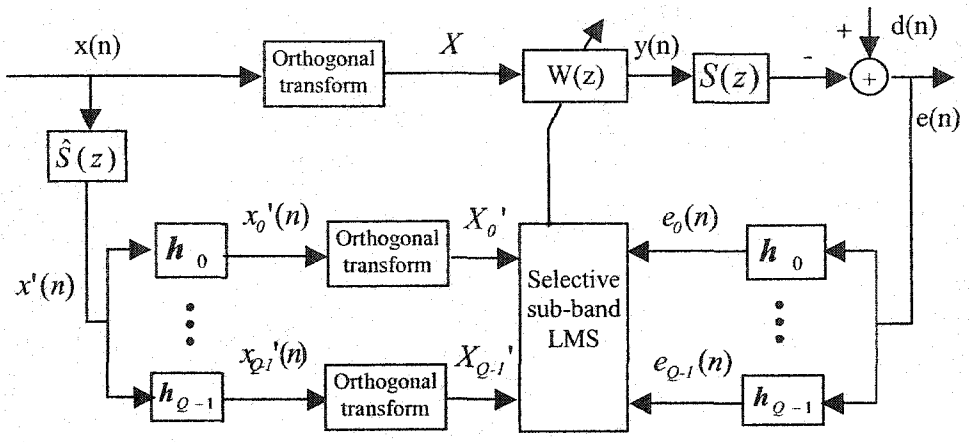



Figure 4.18 Block diagram of the combined frequency domain and sub-band decomposition structure.

constructive interference at the higher frequencies. In the combined frequency domain/sub-band algorithm, the reference signal and the error signal are decomposed into two sub-bands and the weight vector is updated using only the low frequency sub-band signals. Doing so, the combined frequency domain/sub-band algorithm models the primary disturbance at the low frequency band better, hence achieves better vibration reduction at the low frequency band while the constructive interference at the high frequency band is alleviated by the selective adaptation technique. It should be noted that this combined structure is less effective when the number of the sub-bands $Q$ is large. The effectiveness is reduced because the eigenvalue spread of the sub-band signal $x_q'(n)$ decreases as $Q$ increases. Consequently, the orthogonal transform of $x_q'(n)$ cannot improve the convergence.

The sub-band decomposition and orthogonal transform on the filtered reference signal in Figure 4.18 are essentially linear operations. Therefore, it is possible to swap

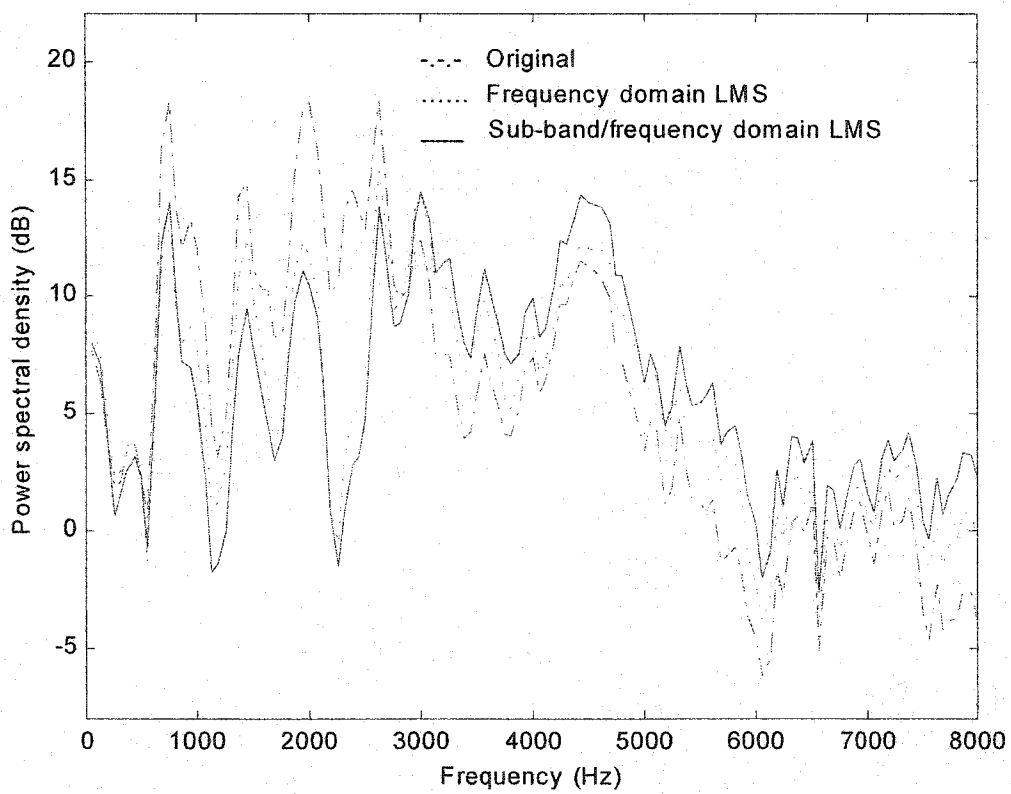



Figure 4.19 Simulation result of the frequency domain LMS(dotted line) and the combined frequency domain/sub-band LMS (solid line) when the selective adaptation technique is used to alleviate the constructive interference at the high frequency band.

the order of the sub-band decomposition and orthogonal transform to obtain a more computationally efficient structure. We cannot simply swap the order (Appendix C proves the direct swap does not work). Instead, some other kind of implementation structures must be employed. We will leave this as a further research direction.

The combined frequency domain/sub-band algorithm can also achieve a better convergence rate since it not only can reduce the eigenvalue spread in the frequency domain, but also can normalize the step size in each sub-band as well. Figure 4.20 shows the learning curves of the frequency domain LMS, sub-band LMS, and the combined frequency domain/sub-band LMS using the AR(2) process specified in Section 4.3.2. The combined frequency domain/sub-band LMS achieves the fastest convergence rate as expected.

## 4.5 Computational complexity

The computational complexity of the sub-band LMS depends on the order of the adaptive filter ($N$), the number of sub-bands ($Q$) and the order of the analysis filter ($L$). The number of multiplications required for each sample is $Q*(2L+N+1)+N$. $2L$ multiplications are used to decompose the reference signal and the error signal, respectively. Each sub-band requires $N+1$ multiplications for weight updating and step size mixing. $N$ multiplications are used to form the full-band control signal. The combined sub-band and frequency domain algorithm requires $2N$ more multiplications to transform the sub-band reference signal in each sub-band and another $2N$ multiplications for the full-band reference signal transform. For comparison purposes, Table 4.1 summarizes the computational requirements of the common adaptive

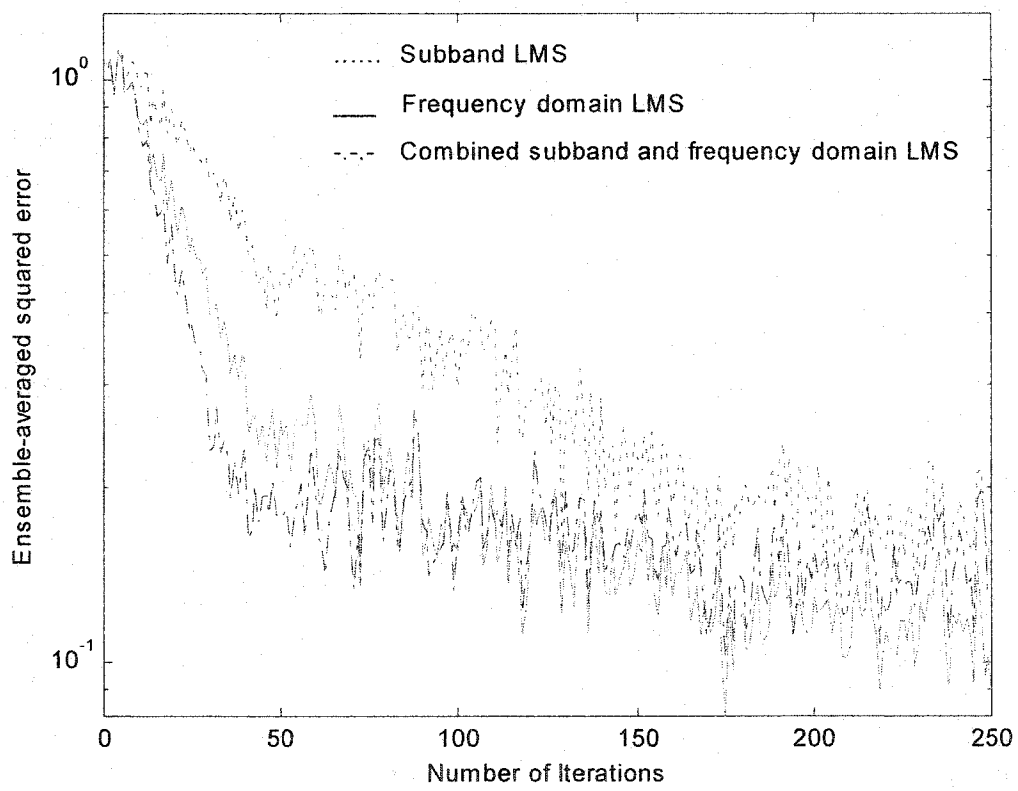



Figure 4.20 Experimental learning curves of the sub-band LMS (dotted line), frequency domain LMS (solid line), and the combined frequency domain/sub-band LMS (dashdot line) with $\mu$=0.01.

algorithms. The fast affine projection (FAP) [38]-[41] has a property that lies between those of the LMS and the recursive least-squares (RLS) algorithm, *i.e.*, less computational complexity than RLS but much faster convergence than LMS.

Table 4.1 Comparison of the computational complexity of different adaptive algorithms

| ***Algorithm*** | ***Number of multiplications per sample*** |
|---|---|
| LMS | $2N+1$ |
| RLS [42] | $3(N+1)^2+3(N+1)$ |
| Frequency domain LMS (freq. sampling structure) | $4N+1$ |
| Sub-band LMS | $Q*(2L+N+1)+N$ |
| Combined sub-band and freq. domain LMS | $Q*(2L+3N+1)+3N$ |
| FAP (embedded fast RLS algorithm [39]) | $2N+20M$ |
| FAP (efficient approximate implementations [41]) | $2N+10M+0.5\log_2 N$ |

$N$: order of the adaptive filter
$L$: order of the analysis filter
$Q$: number of sub-bands in sub-band LMS
$M$: number of projections in FAP

# Chapter 5

# Multiple-channel active control systems

In active noise control systems, it is desirable to reduce the acoustic noise inside the enclosure. In active vibration control systems for complex mechanical structures such as the hard disk drives where different areas vibrate in different modes, the vibration needs to be reduced in several places. These applications require the single-channel active control system to be expanded to a multiple-channel case that uses several secondary sources (actuators) as well as error sensors. This chapter discusses the multiple-channel adaptive feedback control systems.

Section 5.1 develops the FXLMS adaptive algorithm for the multiple-channel systems. Multiple-channel secondary path transfer function modeling techniques are discussed in Section 5.2. Section 5.3 derives the optimal performance that a multiple-channel feedback control system can achieve. The regular control system, the simplified control system, and the decentralized control system are discussed separately. Section 5.4 performs some simulations for a 2×2 control system. Section 5.5 discusses how to improve the stability of the control system.

## 5.1 Multiple-channel FXLMS algorithm

For a general $K$ actuators and $M$ error sensors multiple-channel system, there are $K$ control signals, $y_k(n)$, which drive the corresponding actuators, and $M$ residual signals,

$e_m(n)$, which are the outputs of the $M$ error sensors. Generally, each control signal will contribute to each residual error signal. Consequently, there are $M \times K$ secondary paths, $S_{mk}(z)$ from the $k^{th}$ actuator to the $m^{th}$ error sensor. These paths are estimated by the corresponding digital filters $\hat{S}_{mk}(z)$. The reference signal synthesizer uses the $K$ control signals $y_k(n)$, the $M$ residual error signals $e_m(n)$, and the $M \times K$ secondary path estimates $\hat{S}_{mk}(z)$ to generate the $M$ reference signals $x_m(n)$. Since there are $M$ reference signals, $x_m(n)$, and $K$ actuators, we require $K \times M$ adaptive filters, $W_{km}(z)$, to generate the control signal for each combination ($W_{km}(z)$ uses $x_m(n)$ as the reference signal and the output goes to the $k^{th}$ actuator). The synthesized reference signals, which are the restored primary disturbances at the $M$ points where the sensors are located, are expressed as

$$x_m(n) = e_m(n) + \sum_{k=1}^{K} \hat{s}_{mk}(n) * y_k(n), m = 1,2,...,M , \tag{5.1}$$

where $\hat{s}_{mk}(n)$ is the impulse response of the secondary path estimate $\hat{S}_{mk}(z)$. The $k^{th}$ control signal, $y_k(n)$, which drives the $k^{th}$ actuator, is the sum of the outputs from the $M$ adaptive filters connected to the $k^{th}$ actuator. It is expressed as

$$y_k(n) = \sum_{m=1}^{M} w_{km}(n) * x_m(n), k = 1,2,...,K , \tag{5.2}$$

where $w_{km}(n)$ is the impulse response of the adaptive filter $W_{km}(z)$. Each filter $W_{km}(z)$ is adapted to minimize the cost function $\xi(n) = \sum_{j=1}^{M} e_j^2(n)$, *i.e.*, the sum of the instantaneous squares of the $M$ residual errors based on its own reference signal, $x_m(n)$.

The cost function $\xi(n)$ is a quadratic function of each of the $K \times M$ filter weight vectors, $w_{km}(n)$ [43], [44] and the optimum set of the filter coefficients required to minimize $\xi(n)$ may be evaluated adaptively using the gradient descent method. That is,

$$w_{km}(n+1) = w_{km}(n) - \frac{\mu}{2}\nabla\xi(n) = w_{km}(n) - \mu\sum_{j=1}^{M}\frac{\partial e_j(n)}{\partial w_{km}(n)}e_j(n). \tag{5.3}$$

The $j^{th}$ residual error $e_j(n)$ is given by

$$\begin{aligned} e_j(n) &= d_j(n) - \sum_{p=1}^{K} s_{jp}(n) * y_p(n) \\ &= d_j(n) - \sum_{p=1}^{K} s_{jp}(n) * [\sum_{q=1}^{M} w_{pq}(n) * x_q(n)],\ j = 1,2,...,M, \end{aligned} \tag{5.4}$$

where $d_j(n)$ is the original disturbance at the point where the $j^{th}$ error sensor is located. The derivative of $e_j(n)$ with respect to $w_{km}(n)$ only has non-zero values when $p=k$ and $q=m$ in Equation (5.4). That is,

$$\frac{\partial e_j(n)}{\partial w_{km}(n)} = -s_{jk}(n) * x_m(n). \tag{5.5}$$

Again, the weight vector $w_{km}(n)$ is assumed to be time invariant as in Section 4.1 to evaluate the derivative. This assumption can only be justified if the time variation of the adaptive filter takes place with a very slow rate or when the time delay associated with the secondary path transfer function is negligible.

In practical active control systems, $s_{jk}(n)$ is not available and will be replaced with its estimate $\hat{s}_{jk}(n)$. Replacing $s_{jk}(n)$ with $\hat{s}_{jk}(n)$ in Equation (5.5) and substituting Equation (5.5) into Equation (5.3), the resulting multiple-channel FXLMS algorithm is

$$w_{km}(n+1) = w_{km}(n) + \mu \sum_{j=1}^{M} [\hat{s}_{jk}(n) * x_m(n)] e_j(n) \tag{5.6}$$

Figure 5.1 shows the details of a 2×2 adaptive feedback control system without on-line identification of $\hat{S}_{mk}(z)$. We discuss the on-line identification of the secondary paths in Section 5.2. Two control signals, $y_1(n)$ and $y_2(n)$ are generated as

$$y_1(n) = w_{11}(n) * x_1(n) + w_{12}(n) * x_2(n) \tag{5.7}$$

$$y_2(n) = w_{21}(n) * x_1(n) + w_{22}(n) * x_2(n), \tag{5.8}$$

where $w_{11}(n), w_{12}(n), w_{21}(n)$ and $w_{22}(n)$ are the impulse responses of the adaptive filters $W_{11}(z)$, $W_{12}(z)$, $W_{21}(z)$, and $W_{22}(z)$, respectively. The reference signals, $x_1(n)$ and $x_2(n)$ are synthesized as

$$x_1(n) = e_1(n) + \hat{s}_{11}(n) * y_1(n) + \hat{s}_{12}(n) * y_2(n) \tag{5.9}$$

$$x_2(n) = e_2(n) + \hat{s}_{21}(n) * y_1(n) + \hat{s}_{22}(n) * y_2(n), \tag{5.10}$$

where $\hat{s}_{11}(n), \hat{s}_{12}(n), \hat{s}_{21}(n)$, and $\hat{s}_{22}(n)$ are the impulse responses of the secondary path estimates $\hat{S}_{11}(z), \hat{S}_{12}(z), \hat{S}_{21}(z)$, and $\hat{S}_{22}(z)$, respectively. The weights of the four adaptive filters are updated using the multiple-channel FXLMS algorithm expressed as

$$w_{11}(n+1) = w_{11}(n) + \mu\{[\hat{s}_{11}(n) * x_1(n)] e_1(n) + [\hat{s}_{21}(n) * x_1(n)] e_2(n)\} \tag{5.11}$$

$$w_{21}(n+1) = w_{21}(n) + \mu\{[\hat{s}_{12}(n) * x_1(n)] e_1(n) + [\hat{s}_{22}(n) * x_1(n)] e_2(n)\} \tag{5.12}$$

$$w_{12}(n+1) = w_{12}(n) + \mu\{[\hat{s}_{11}(n) * x_2(n)] e_1(n) + [\hat{s}_{21}(n) * x_2(n)] e_2(n)\} \tag{5.13}$$

$$w_{22}(n+1) = w_{22}(n) + \mu\{[\hat{s}_{12}(n) * x_2(n)] e_1(n) + [\hat{s}_{22}(n) * x_2(n)] e_2(n)\}. \tag{5.14}$$

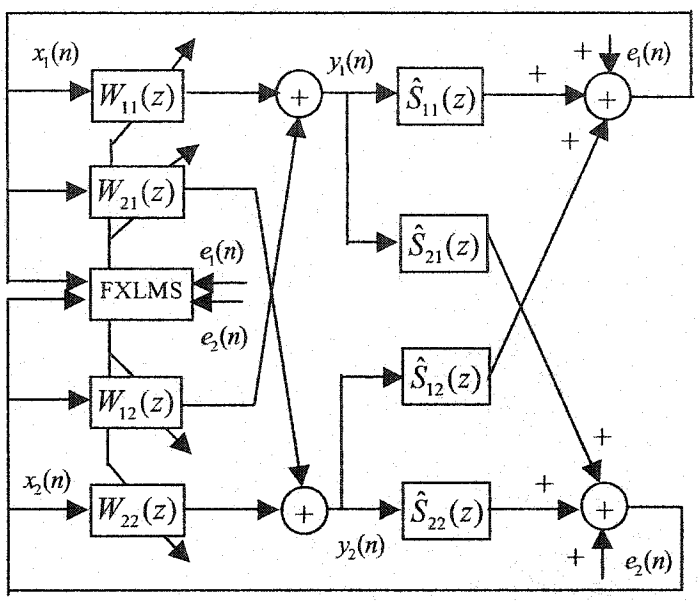



Figure 5.1 A 2×2 adaptive feedback active control system without on-line identification.

## 5.2 On-line identification of the multiple secondary paths

For a general multiple-channel system with K actuators and M error sensors, there are K×M secondary paths, $S_{mk}(z)$ from the $k^{th}$ actuator to the $m^{th}$ error sensor, which need to be identified. On-line modeling of the K×M secondary paths for a multiple-channel active control system is more difficult than in the single-channel case, because the error signal $e_m(n)$ from the $m^{th}$ error sensor is a mixture of the primary disturbance at point $m$ and the secondary signals from all secondary paths, $S_{mk}(z)$ for $k=1,2,...,K$. In order to simultaneously identify the K×M secondary path transfer functions $S_{mk}(z)$, we must have $K$ excitation signals driving each of the $K$ secondary sources. Because of the interchannel coupling, these $K$ excitation signals must be independent. Otherwise, the

estimates of these secondary path transfer functions are biased [14]. To explain the effect of the interchannel coupling, consider a 2×2 system, *i.e.,* a system with two actuators and two error sensors as illustrated in Figure 5.2, that only shows one of the two error signals $e_1(n)$, and uses one additive random noise *v(n)* for on-line secondary path modeling. The error signal $e_1(n)$ is the error signal measured by the first error sensor, which is the residual error of the primary disturbance $d_1(n)$ canceled by the control signals from both secondary sources. Adaptive filters $\hat{S}_{11}(z)$ and $\hat{S}_{12}(z)$ are used to model the secondary paths $S_{11}(z)$ and $S_{12}(z)$ on-line, respectively.

For the adaptation of $\hat{S}_{11}(z)$, *v(n)* is the input signal and $f_1(n)$ is the error signal used for updating the weights. The desired signal for modeling $S_{11}(z)$ is

$$u(n) = s_{11}(n) * [y_1(n) + v(n)] + s_{12}(n) * [y_2(n) + v(n)] - d_1(n) - \hat{s}_{12}(n) * v(n). \qquad (5.15)$$

The adaptive filter $\hat{S}_{11}(z)$ converges to its Wiener solution as

$$\hat{S}_{11}^{o}(z) = \frac{S_{uv}(z)}{S_{vv}(z)}, \qquad (5.16)$$

where $S_{vv}(z)$ is the autopower spectrum of *v(n)* and $S_{uv}(z)$ is the cross-power spectrum between the desired signal *u(n)* and the input signal *v(n)*. Assuming that the excitation signal *v(n)* is zero-mean and is uncorrelated with $y_1(n)$, $y_2(n)$ and $d_1(n)$, $S_{uv}(z)$ can be determined from Equation (5.15) as

$$S_{uv}(z) = [S_{11}(z) + S_{12}(z) - \hat{S}_{12}(z)]S_{vv}(z). \qquad (5.17)$$

Substituting Equation (5.17) into Equation (5.16), the optimum solution of $\hat{S}_{11}(z)$ becomes

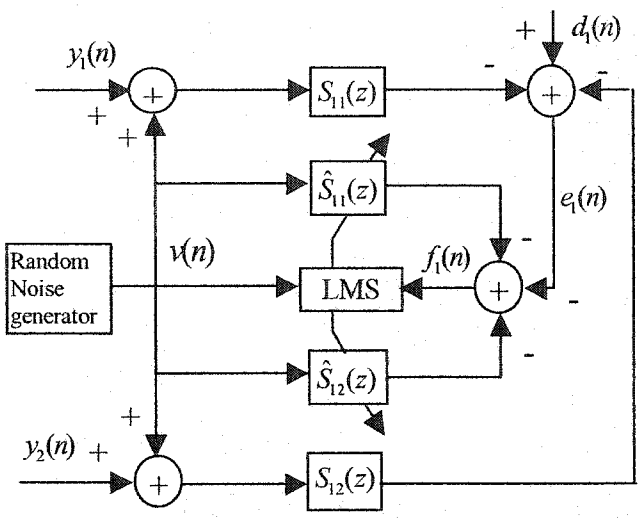



Figure 5.2 On-line identification of the secondary paths using one random noise generator.

$$\hat{S}_{11}^{o}(z) = S_{11}(z) + [S_{12}(z) - \hat{S}_{12}(z)]. \tag{5.18}$$

Equation (5.18) shows that when random noise components are picked up by the first error sensor through multiple secondary paths ($S_{11}(z)$ and $S_{12}(z)$, in this case), the estimate $\hat{S}_{11}(z)$ is biased by the cross-coupled secondary paths $S_{12}(z)$ and $\hat{S}_{12}(z)$. The desired result $\hat{S}_{11}(z) = S_{11}(z)$ occurs only if $\hat{S}_{12}(z) = S_{12}(z)$. Since $\hat{S}_{12}(z)$ itself is being simultaneously adapted with $\hat{S}_{11}(z)$, there can be no unique solution for either filter.

To remove this interchannel coupling associated with the multiple-channel systems, $K$ random noise generators can be employed such that the $K$ random noises used to drive the $K$ actuators are mutually uncorrelated. For a 2×2 system, two random noise generators as shown in Figure 5.3 are employed to generate the random noises $v_1(n)$

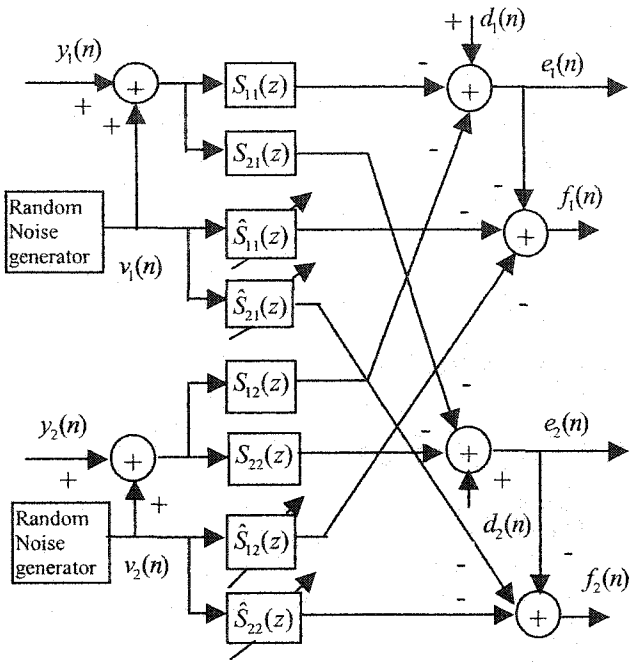



Figure 5.3 On-line identification of the secondary paths for a 2×2 system using two random noise generators.

and $v_2(n)$, which are mutually uncorrelated and also uncorrelated with $y_1(n), y_2(n), d_1(n)$ and $d_2(n)$. Then, the desired signal for modeling $S_{11}(z)$ becomes

$$u(n) = s_{11}(n) * [y_1(n) + v_1(n)] + s_{12}(n) * [y_2(n) + v_2(n)] - d_1(n) - \hat{s}_{12}(n) * v_2(n) \quad (5.19)$$

and Equation (5.16) changes to

$$\hat{S}_{11}^{o}(z) = \frac{S_{uv_1}(z)}{S_{v_1v_1}(z)}. \quad (5.20)$$

Equation (5.17) is simplified to

$$S_{uv_1}(z) = S_{11}(z) S_{v_1v_1}(z) \quad (5.21)$$

because $v_1(n)$ and $v_2(n)$ are uncorrelated. Then, the optimum solution of $\hat{S}_{11}(z)$ is correctly obtained as

$$\hat{S}_{11}^{o}(z) = S_{11}(z). \tag{5.22}$$

The same symmetric analysis applies to the adaptation of $\hat{S}_{12}(z)$.

For a K×M system, $K$ independent random noise generators are required to remove the interchannel coupling. When $K$ is large, the cost may be too high for some real time systems. An alternative is to use a single noise source with inter-channel delay to decorrelate the excitation signals instead of the multiple random noise generators [45]. This technique allows on-line modeling of the secondary paths using a single random noise generator, hence reduces the cost of on-line identifications.

## 5.3 Optimal performances of the multiple-channel control systems

This section uses a unified way to formulate the optimal performances of the three variants of the multiple-channel feedback control system, and explicitly show the dependence of the optimal performance on the correlation coefficients of the primary disturbances and the impulse response of the secondary paths. It is assumed that there are $M$ secondary sources and $M$ error sensors in the multiple-channel system and the $M \times M$ secondary paths can be estimated accurately in our discussion. We also assume that all the signals are real valued for simplicity of derivation.

### 5.3.1 Regular control system

The regular multiple-channel feedback control system can be illustrated as in Figure 5.4, in which:

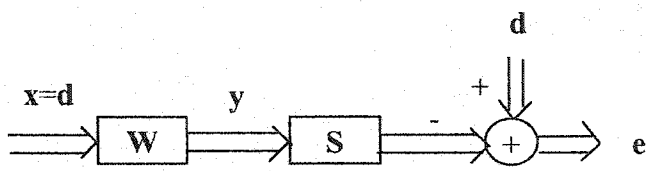



Figure 5.4 Block diagram of the multiple-channel feedback control system where the secondary paths can be estimated accurately.

**W** M×M matrix of responses of the control filters

**S** M×M matrix of responses of the secondary paths

**d** M×1 vector of the primary disturbances

**e** M×1 vector of the residual errors

**y** M×1 vector of the control signals

**x** M×1 vector of the reference signals

If the control filters are implemented as FIR filters of order J and the secondary paths are modeled as FIR filters of order K, the output of the $i^{th}$ error sensor at time instant $n$ can be written as

$$e_i(n) = d_i(n) - \sum_{m=1}^{M} y_m(n) * s_{im} = d_i(n) - \sum_{m=1}^{M}\sum_{k=0}^{K} s_{im}(k) y_m(n-k), i = 1,2,...,M, \quad (5.23)$$

where $d_i(n)$ is the primary disturbance at the $i^{th}$ error sensor and $\mathbf{s}_{im} = [s_{im}(0), s_{im}(1), \cdots, s_{im}(K)]^T$ is the impulse response vector of the secondary path from the $m^{th}$ secondary source to the $i^{th}$ error sensor. The $m^{th}$ control signal $y_m(n)$, *i.e.*, the input to the $m^{th}$ secondary source, is the sum of the outputs of those M control filters that aim at the $m^{th}$ secondary source, and can be written as

$$y_m(n) = \sum_{l=1}^{M} x_l(n) * w_{ml} = \sum_{l=1}^{M}\sum_{j=0}^{J} w_{ml}(j)x_l(n-j),\ m = 1,2,...,M\ , \tag{5.24}$$

where $x_l(n)$ is the $l^{th}$ reference signal and $\boldsymbol{w}_{ml} = [w_{ml}(0), w_{ml}(1),..., w_{ml}(J)]^T$ is the weight vector of the control filter $W_{ml}(z)$, which uses $x_l(n)$ as the input signal and the output goes to the $m^{th}$ secondary source. Substituting Equation (5.24) into (5.23), we have

$$\begin{aligned} e_i(n) &= d_i(n) - \sum_{m=1}^{M}\sum_{l=1}^{M}\sum_{j=0}^{J} w_{ml}(j)\sum_{k=0}^{K} s_{im}(k)x_l(n-j-k) \\ &= d_i(n) - \sum_{m=1}^{M}\sum_{l=1}^{M}\sum_{j=0}^{J} w_{ml}(j)u_{iml}(n-j),\ i = 1,2,...,M\ , \end{aligned} \tag{5.25}$$

where $u_{iml}(n)$ is the filtered reference signal $x_l(n)$ by the secondary path $s_{im}$. Equation (5.25) illustrates the linear relationship between the error signal and the filter coefficients and can be rewritten in matrix form as [43], [47]

$$\boldsymbol{e}(n) = \boldsymbol{d}(n) - \boldsymbol{U}(n)\boldsymbol{w} \tag{5.26}$$

in which

$$\boldsymbol{e}(n) = [e_1(n), e_2(n),..., e_M(n)]^T \tag{5.27}$$

$$\boldsymbol{d}(n) = [d_1(n), d_2(n),..., d_M(n)]^T \tag{5.28}$$

$$\boldsymbol{U}(n) = \begin{bmatrix} \boldsymbol{u}_1{}^T(n), \boldsymbol{u}_1{}^T(n-1),....., \boldsymbol{u}_1{}^T(n-J) \\ \boldsymbol{u}_2{}^T(n), \boldsymbol{u}_2{}^T(n-1),....., \boldsymbol{u}_2{}^T(n-J) \\ \vdots \\ \boldsymbol{u}_M{}^T(n), \boldsymbol{u}_M{}^T(n-1),..., \boldsymbol{u}_M{}^T(n-J) \end{bmatrix} \tag{5.29}$$

where

$$\boldsymbol{u}_i(n) = [u_{i11}(n), u_{i12}(n),..., u_{i1M}(n), u_{i21}(n),..., u_{iMM}(n)]^T \tag{5.30}$$

and

$$\boldsymbol{w} = [\boldsymbol{w}^T(0), \boldsymbol{w}^T(1), ..., \boldsymbol{w}^T(J)]^T \tag{5.31}$$

where

$$\boldsymbol{w}(i) = [w_{11}(i), w_{12}(i), ..., w_{1M}(i), w_{21}(i), ..., w_{MM}(i)]^T . \tag{5.32}$$

We define the cost function $\xi(n)$ as the expectation of the sum of the squared errors

$$\xi(n) = E[\sum_{m=1}^{M} e_m^{\,2}(n)] = E[\boldsymbol{e}^T(n)\boldsymbol{e}(n)] . \tag{5.33}$$

Then, using Equation (5.26), $\xi(n)$ can be expressed in the general matrix form as

$$\begin{aligned} \xi(n) &= E[\boldsymbol{d}^T(n) - \boldsymbol{w}^T\boldsymbol{U}^T(n)][\boldsymbol{d}(n) - \boldsymbol{U}(n)\boldsymbol{w}] \\ &= \boldsymbol{w}^T\boldsymbol{R}\boldsymbol{w} - 2\boldsymbol{w}^T\boldsymbol{p} + \sigma , \end{aligned} \tag{5.34}$$

where $\boldsymbol{R} = E[\boldsymbol{U}^T(n)\boldsymbol{U}(n)]$, $\boldsymbol{p} = E[\boldsymbol{U}^T(n)\boldsymbol{d}(n)]$, and $\sigma = E[\boldsymbol{d}^T(n)\boldsymbol{d}(n)]$. The Wiener solution minimizing Equation (5.34) is given by

$$\boldsymbol{w}_{opt} = \boldsymbol{R}^{-1}\boldsymbol{p} , \tag{5.35}$$

which results in the optimal value of the mean square error

$$\xi_{\min} = \sigma - \boldsymbol{p}^T\boldsymbol{R}^{-1}\boldsymbol{p} . \tag{5.36}$$

When the secondary paths can be estimated accurately, the reference signal $x_l(n)$ equals the primary disturbance $d_l(n)$. Consequently, the filtered reference signal $u_{iml}(n)$ is the filtered version of $d_l(n)$ by the secondary path $s_{im}$. Therefore, $\boldsymbol{R}$ and $\boldsymbol{p}$ in Equation (5.36) can be expressed in terms of the correlation coefficients of the primary disturbances and the impulse responses of the secondary paths. Specifically, let $r_{ql}(k)$ be the correlation between the primary disturbance $d_q(n)$ and $d_l(n)$ with lag $k$, *i.e.*,

$$r_{ql}(k) = E[d_q(n)d_l(n-k)],\ q,l = 1,2,...,M\ , \tag{5.37}$$

then the crosscorrelation between $d_q(n)$ and $u_{iml}(n)$ can be derived as $E[d_q(n)u_{iml}(n-k)] = r_{ql}(k) * s_{im} = \sum_{j=0}^{K} s_{im}(j)r_{ql}(k-j)$. Using Equation (5.28) and (5.29), $\boldsymbol{p}$ can be expressed as

$$\boldsymbol{p} = E[\boldsymbol{U}^T(n)\boldsymbol{d}(n)] = [f_{11}(0), f_{12}(0),..., f_{MM}(0), f_{11}(1),..., f_{11}(J),..., f_{MM}(J)]^T\ , \tag{5.38}$$

where $f_{ij}(k) = \sum_{m=1}^{M} r_{mj}(k) * s_{mi} = \sum_{m=1}^{M}\sum_{l=0}^{K} s_{mi}(l)r_{mj}(k-l)$.

Similarly, define the correlation between $u_{ijl}(n)$ and $u_{mqt}(n)$ as $v_{ijlmqt}(k)$, *i.e.*,

$$\begin{aligned} v_{ijlmqt}(k) &= E[u_{ijl}(n)u_{mqt}(n-k))] \\ &= E\{[s_{ij} * d_l(n)][s_{mq} * d_t(n-k)]\} \\ &= \sum_{h=0}^{K}\{s_{mq}(h)\sum_{p=0}^{K}[s_{ij}(p)r_{lt}(k+h-p)]\}. \end{aligned} \tag{5.39}$$

Then,

$$\boldsymbol{R} = E[\boldsymbol{U}^T(n)\boldsymbol{U}(n)] = \begin{bmatrix} \boldsymbol{g}(0) & \boldsymbol{g}(1) & \cdots & \boldsymbol{g}(J) \\ \boldsymbol{g}(-1) & \boldsymbol{g}(0) & \cdots & \boldsymbol{g}(J-1) \\ \vdots & \vdots & \ddots & \vdots \\ \boldsymbol{g}(-J) & \boldsymbol{g}(-J+1) & \cdots & \boldsymbol{g}(0) \end{bmatrix}, \tag{5.40}$$

where the $M^2 \times M^2$ matrix $\boldsymbol{g}(k)$ is defined as

$$\boldsymbol{g}(k) = \sum_{i=1}^{M} \begin{bmatrix} v_{i1i1i1}(k) & v_{i1i1i2}(k) & \cdots & v_{i1i1i21}(k) & \cdots & v_{i1i1iMM}(k) \\ v_{i1i2i1}(k) & v_{i1i2i2}(k) & \cdots & v_{i1i2i21}(k) & \cdots & v_{i1i2iMM}(k) \\ \vdots & \vdots & \ddots & \vdots & \ddots & \vdots \\ v_{iMMi11}(k) & v_{iMMi12}(k) & \cdots & v_{iMMi21}(k) & \cdots & v_{iMMiMM}(k) \end{bmatrix}. \tag{5.41}$$

Using Equation (5.36)-(5.41), the minimum mean square of the regular multiple-

channel feedback control system can be calculated with the knowledge of the correlation coefficients of the primary disturbances and the secondary paths.

### 5.3.2 Simplified control system

In the simplified feedback control system with M secondary sources and M error sensors as shown in Figure 5.5, only M control filters are employed and each secondary source is driven by the output from one control filter only. Each control filter is still adjusted to minimize the sum of the squared output from all the error sensors. The input to the $m^{th}$ secondary source, $y_m(n)$, is now the output of the control filter $W_m(z)$ only, *i.e.*,

$$y_m(n) = x_m(n) * w_m = \sum_{j=0}^{J} w_m(j) x_m(n-j),\ m = 1,2,...,M\ , \tag{5.42}$$

where $\boldsymbol{w}_m = [w_m(0), w_m(1),..., w_m(J)]^T$ is the weight vector of the $m^{th}$ control filter and $x_m(n)$ is the corresponding input signal. Using Equation (5.23), the output of the $i^{th}$ error sensor at time instant $n$ changes to

$$\begin{aligned} e_i(n) &= d_i(n) - \sum_{m=1}^{M}\sum_{j=0}^{J} w_m(j) \sum_{k=0}^{K} s_{im}(k) x_m(n-j-k) \\ &= d_i(n) - \sum_{m=1}^{M}\sum_{j=0}^{J} w_m(j) u_{imm}(n-j),\ i = 1,2,...,M\ , \end{aligned} \tag{5.43}$$

where $u_{imm}(n)$ is the filtered reference signal $x_m(n)$ by the secondary path $s_{im}$.

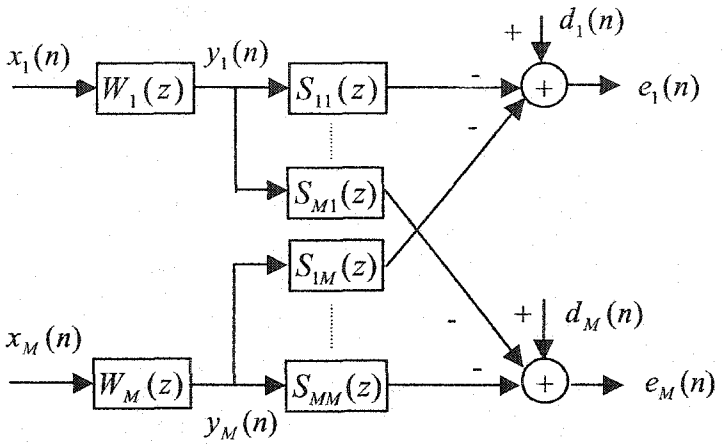



Figure 5.5 Simplified multiple-channel feedback control system where each secondary source is driven by the output of one control filter only.

The error signals of the simplified control system can still be written in matrix form as Equation (5.26), but $\boldsymbol{u}_i(n)$ in Equation (5.30) changes to

$$\boldsymbol{u}_i(n) = [u_{i11}(n), u_{i22}(n), \ldots, u_{iMM}(n)]^T \tag{5.44}$$

and $\boldsymbol{w}(i)$ in Equation (5.32) changes to

$$\boldsymbol{w}(i) = [w_1(i), w_2(i), \ldots, w_M(i)]^T . \tag{5.45}$$

The minimum mean square error of the simplified control system is still expressed as in Equation (5.36), but $\boldsymbol{p}$ now changes to

$$\boldsymbol{p} = E[\boldsymbol{U}^T(n)\boldsymbol{d}(n)] = [f_1(0), f_2(0), \ldots, f_M(0), f_1(1), \ldots, f_1(J), \ldots, f_M(J)]^T , \tag{5.46}$$

where $f_i(k) = \sum_{m=1}^{M} r_{mi}(k) * s_{mi} = \sum_{m=1}^{M}\sum_{l=0}^{K} s_{mi}(l) r_{mi}(k-l)$. The correlation matrix $\boldsymbol{R}$ of the simplified control system remains the same expression as given in Equation (5.40), but the matrix $\boldsymbol{g}(k)$ in Equation (5.41) changes to an M×M matrix

$$g(k)=\sum_{i=1}^{M}\begin{bmatrix} v_{i11i11}(k) & v_{i11i22}(k) & \cdots & v_{i11iMM}(k) \\ v_{i22i11}(k) & v_{i22i22}(k) & \cdots & v_{i22iMM}(k) \\ \vdots & \vdots & \ddots & \vdots \\ v_{iMMi11}(k) & v_{iMMi22}(k) & \cdots & v_{iMMiMM}(k) \end{bmatrix}. \tag{5.47}$$

Using Equation (5.36), (5.37), (5.39), (5.40), (5.46) and (5.47), the minimum mean square of the simplified multiple-channel feedback control system can be calculated with the knowledge of the correlation coefficients of the primary disturbances and the secondary paths.

### 5.3.3 Decentralized control system

Both the regular control system and the simplified control system can be described as being fully coupled since each secondary source is being adjusted in response to the output of all the error sensors. The fully coupled control system may require considerable processing power to implement and generally has a relatively complicated model of the system under control, which accounts for all the interactions between each of the secondary sources and each of the error sensors. One way of avoiding these problems is to decentralize the control system. That is, each secondary source is adjusted to minimize the sum of a smaller number of error sensors. The limit of this approach would be when there were as many secondary sources as error sensors, and the input to each secondary source is adjusted to minimize the output of one error sensor only. This is equivalent to M (the number of error sensors or secondary sources) isolated single-channel systems, and it is called fully decentralized control [48]. Figure 5.5 can still be used to illustrate the fully decentralized control system with M secondary sources and M error sensors. Each control filter $W_m(z)$ in the fully

decentralized control system is now updated to minimize the squared output of the $m^{th}$ error sensor only. Unlike the simplified control system where all the M×M secondary paths have to be estimated, the decentralized control system only estimates the M direct paths $s_{mm}$ *(m=1,2,...,M).* The fully decentralized control system differs from the simplified control system in that the $m^{th}$ reference signal $x_m(n)$ no longer is equal to the $m^{th}$ primary disturbance $d_m(n)$. The $m^{th}$ control filter $W_m(z)$ generates its reference signal $x_m(n)$ by adding its output at the summing point to the output from the $m^{th}$ error sensor, *i.e.*,

$$x_m(n) = e_m(n) + \sum_{k=0}^{K} s_{mm}(k) y_m(n-k)$$

$$= d_m(n) - \sum_{i=1, i\neq m}^{M} \sum_{j=0}^{J} \sum_{k=0}^{K} w_i(j) s_{mi}(k) x_i(n-j-k) . \qquad (5.48)$$

Let $r'_{im}(k)$ denote the correlation between $d_i(n)$ and $x_m(n)$ with lag $k$, *i.e.*,

$$r'_{im}(k) = E[d_i(n) x_m(n-k)], i, m = 1,2,...,M . \qquad (5.49)$$

In the steady state, $r'_{im}(k)$ can be completely determined by the correlation between the primary disturbance $r_{ql}(k)$ defined in Equation (5.37) as well as the responses of the control filters and the secondary paths. Equation (5.43) is still the expression for $e_i(n)$ and Equation (5.36) is still the minimum mean square error for the fully decentralized control system. The correlation vector $\boldsymbol{p}$ in (5.46) changes to

$$\boldsymbol{p} = E[\boldsymbol{U}^T(n)\boldsymbol{d}(n)] = [f_1'(0), f_2'(0), ..., f_M'(0), f_1'(1), ..., f_1'(J), ..., f_M'(J)]^T , \qquad (5.50)$$

where $f_i'(k) = \sum_{m=1}^{M} r_{mi}'(k) * s_{mi} = \sum_{m=1}^{M} \sum_{l=0}^{K} s_{mi}(l) r_{mi}'(k-l)$.

The correlation matrix $\boldsymbol{R}$ still takes the form of Equation (5.40) but the M×M matrix $\boldsymbol{g(k)}$ changes to

$$\boldsymbol{g}(k)=\sum_{i=1}^{M}\begin{bmatrix} v'_{i11i11}(k) & v'_{i11i22}(k) & \cdots & v'_{i11iMM}(k) \\ v'_{i22i11}(k) & v'_{i22i22}(k) & \cdots & v'_{i22iMM}(k) \\ \vdots & \vdots & \ddots & \vdots \\ v'_{iMMi11}(k) & v'_{iMMi22}(k) & \cdots & v'_{iMMiMM}(k) \end{bmatrix}, \tag{5.51}$$

where

$$\begin{aligned} v'_{ijill}(k) &= E[u_{ijj}(n)u_{ill}(n-k))] \\ &= E\{[s_{ij} * x_j(n)][s_{il} * x_l(n-k)]\} \\ &= \sum_{h=0}^{K}\{s_{il}(h)\sum_{p=0}^{K}[s_{ij}(p)r_{jl}''(k+h-p)]\}, i,j,l=1,2,...,M. \end{aligned} \tag{5.52}$$

$r''_{jl}(k)$ in Equation (5.52) is the correlation between the reference signal $x_j(n)$ and $x_l(n)$. Like $r'_{im}(k)$, $r''_{jl}(k)$ can be completely determined by the correlation between the primary disturbance $r_{ql}(k)$ as well as the responses of the control filters and the secondary paths.

The formulas derived above are useful for analytic comparisons of the three variants of the feedback control system and can be used to guide the selection of the appropriate control scheme. These formulas will be used to compare the theoretical values for a 2×2 system in the next section.

## 5. 4 Computer simulations for a 2×2 system

In this section, we will simulate the performances of the three feedback control systems discussed in the last section for a 2×2 case and compare them with the theoretic values. For simplicity of calculation on the theoretical values, a unit variance AR(2) process with $a_1 = -0.975$ and $a_2 = 0.95$ is employed as the primary disturbance at point 1, *i.e.*, $d_1(n)$ and another unit variance AR(2) process with $a_1 = -1.5955$ and $a_2 = 0.95$ is employed as the primary disturbance at point 2, *i.e.*, $d_2(n)$. It is easy to show that the autocorrelation coefficients of $d_1(n)$ are $\boldsymbol{r}_{11}(k) = [1, \ 0.5, \ -0.4625, \ -0.9259, \ \cdots]$ and the autocorrelation coefficients of $d_2(n)$ are $\boldsymbol{r}_{22}(k) = [1, \ 0.8182, \ 0.3554, \ -0.2102, \ \cdots]$. $d_1(n)$ and $d_2(n)$ are almost uncorrelated and $\boldsymbol{r}_{12}(k)$ and $\boldsymbol{r}_{21}(k)$ are assumed to be zeros to simplify the calculation. It should be noted that we assume the primary disturbances in the simulations are already AR processes without considering the errors of modeling the primary disturbances by AR processes. In real applications, this modeling error is one of the main sources of the residual error.

In the first simulation, let the direct paths be $\boldsymbol{s}_{11} = \boldsymbol{s}_{22} = [0, \ 0.5, \ -0.5]^T$ to exhibit the high pass property and let the cross-coupled path be $\boldsymbol{s}_{21} = \boldsymbol{s}_{12} = [0, \ 0.2, \ 0.2]^T$ to exhibit the low pass property. Since both $d_1(n)$ and $d_2(n)$ have strong energy in the low frequency band (the pole of $d_1(n)$ is at $0.33\pi$ and the pole of $d_2(n)$ is at $0.19\pi$), the regular control system (refer to Figure 5.1 on page 86) is expected to outperform the simplified control system as shown in Figure 5.6. This is

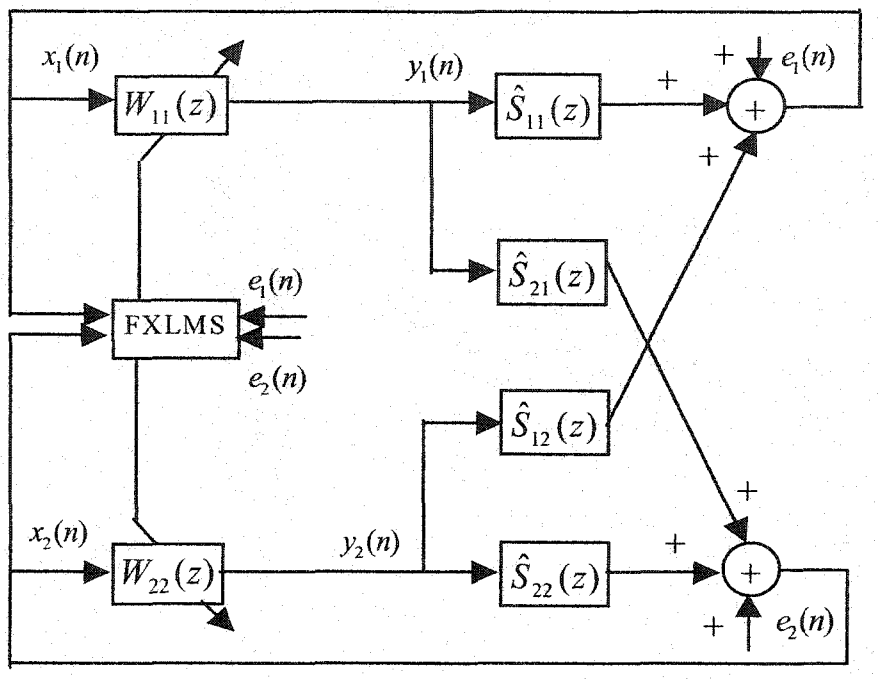



Figure 5.6 Simplified 2×2 adaptive feedback control system with only two control filters.

because $d_1(n)$ can be reduced by the output of $W_{21}(z)$ and $d_2(n)$ can be reduced by the output of $W_{12}(z)$ in the regular control system. Figure 5.7 shows the squared residual errors obtained by the regular control system and Figure 5.8 shows the same information obtained by the simplified control system. All the curves in the simulations are the ensemble average of 100 independent trails of the experiments. It can be seen that the average square error achieved by the regular control system is around *0.15+0.19=0.34* and the averaged square error achieved by the simplified control system is around *0.5+0.8=1.3*.

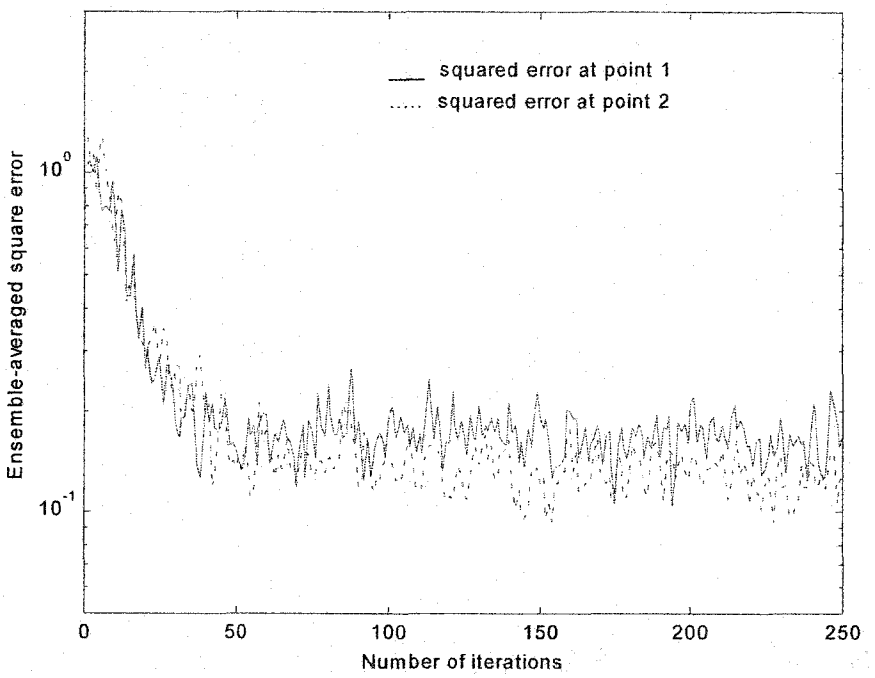



Figure 5.7 The averaged square errors achieved by the regular control system with $\boldsymbol{s}_{11} = \boldsymbol{s}_{22} = [0, \quad 0.5, \quad -0.5]^T$ .

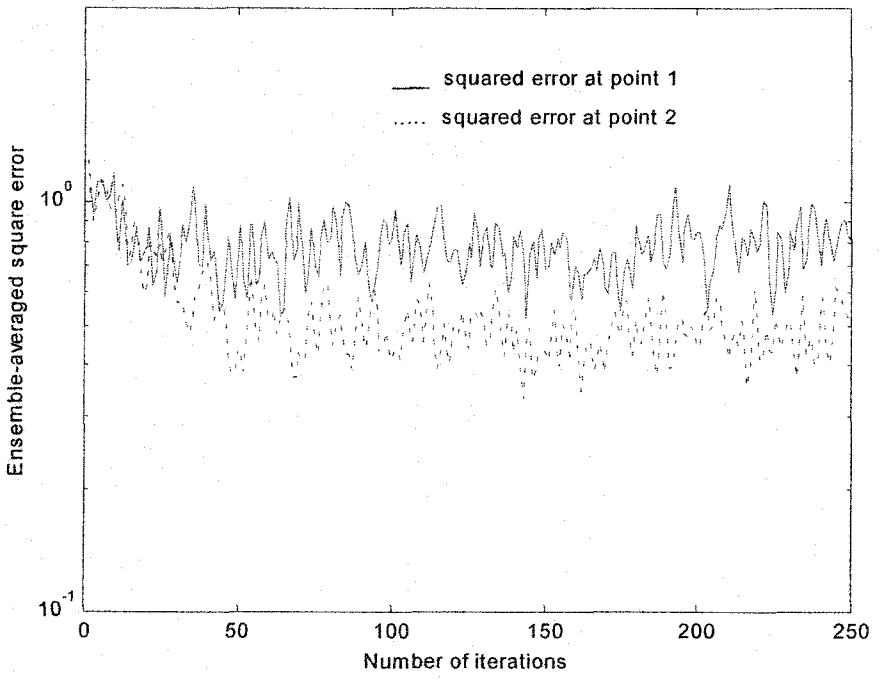



Figure 5.8 The averaged square errors achieved by the simplified control system with $\boldsymbol{s}_{11} = \boldsymbol{s}_{22} = [0, \quad 0.5, \quad -0.5]^T$ .

Using the correlation coefficients and the impulse responses of the secondary paths in the equations given in the last section, the theoretical minimum mean square error that the regular control system can achieve is calculated as $\xi_{\min-regular} = 2 - 1.875 = 0.125$ and the theoretical minimum mean square error that the simplified control system can achieve is calculated as $\xi_{\min-simplified} = 2 - 1.022 = 0.978$. Both the theoretical values and the experimental values confirm that the simplified control system is not attractive using the current frequency responses of the secondary paths. It should be noted that the calculated theoretical minimum *mean* square is the optimal value obtained by the steepest descent algorithm (the Wiener solution) and the experimental result is the value obtained by the LMS algorithm (the stochastic gradient descent algorithm). The difference is called the excess mean square error that results from the noisy estimate for the gradient vector in the LMS algorithm. The excess mean square error increases linearly with the filter length and is directly proportional to the step size of the LMS algorithm.

In the second simulation, we consider the case when the secondary paths are consistent with the frequency responses of the low pass property. Hence, let the direct paths be $\boldsymbol{s}_{11} = \boldsymbol{s}_{22} = [0, \quad 0.5, \quad 0.5]^T$ and let the cross-coupled paths remain the same at $\boldsymbol{s}_{21} = \boldsymbol{s}_{12} = [0, \quad 0.2, \quad 0.2]^T$. Since the secondary paths exhibit similar frequency responses, we should not expect the regular control system to outperform the simplified control system as much as in the first simulation. Using the correlation coefficients and the new impulse responses of the secondary paths in the equations given in the last section, the theoretical minimum mean square error that the regular control system can

achieve changes to $\xi_{\min-regular} = 2 - 1.882 = 0.118$ and the theoretical minimum mean square error that the simplified control system can achieve is reduced to $\xi_{\min-simplified} = 2 - 1.719 = 0.281$. These values are much closer to that of the regular control system. Figure 5.9 shows the experimental results obtained by the regular control system and the simplified control system. The performance of the regular control system is worse under the current setting for the secondary paths.

Figure 5.10 shows the squared residual errors obtained by the decentralized control system. It can be seen that the decentralized control system achieves a performance better than the simplified control system under the current setting for the cross-coupled paths ($\boldsymbol{s}_{12} = \boldsymbol{s}_{21} = [0, \quad 0.2, \quad 0.2]^T$). The frequency responses of the cross-coupled secondary paths directly affect the overall performance. When the responses of the cross-coupled paths become weaker, the performance that the decentralized control system can achieve is expected to improve. On the other hand, when the responses of the cross-coupled paths become stronger, the algorithm tends to diverge. Figure 5.11 shows the cases when the cross-coupled paths change to [0, 0.45, 0.45] (upper set curves) and to [0, 0.05, 0.05] (lower set curves), respectively.

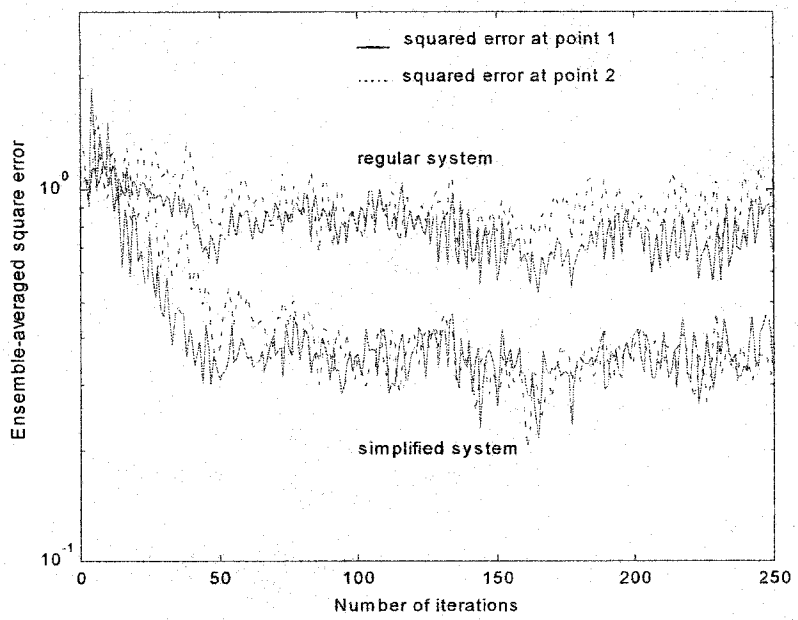



Figure 5.9 The averaged square errors achieved by the regular control system and the simplified control system with $\boldsymbol{s}_{11} = \boldsymbol{s}_{22} = [0, \quad 0.5, \quad 0.5]^T$ .

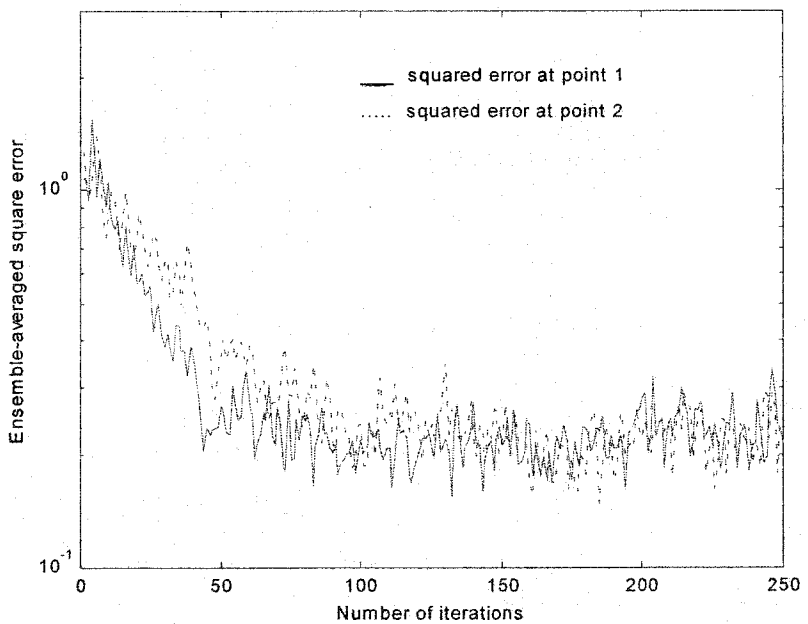



Figure 5.10 The averaged square errors achieved by the fully decentralized control system with $\boldsymbol{s}_{11} = \boldsymbol{s}_{22} = [0, \quad 0.5, \quad 0.5]^T$ .

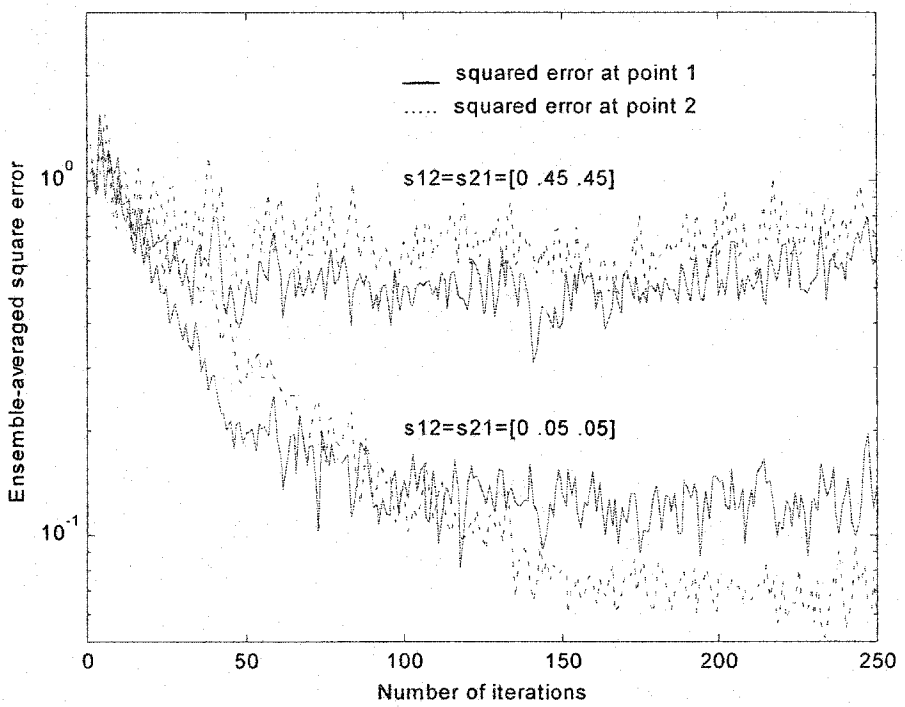



Figure 5.11 The average square errors achieved by the fully decentralized control system with $s_{12} = s_{21} = [0, \quad 0.45, \quad 0.45]^T$ and $s_{12} = s_{21} = [0, \quad 0.05, \quad 0.05]^T$, respectively.

## 5.5 Improving the stability of the feedback control systems

The LMS algorithm updates the control filters to minimize the instantaneous squared output of the error sensors. One side effect of reducing the squared errors only is that the system may obtain very small reductions in the errors at the expense of very large control signals. Large control signals in turn may affect the stability of the feedback control system. The inaccurate estimation of the secondary paths and/or the cross coupling of the secondary paths may also result in the instability of the control system. One way to improve the stability of the control system is to penalize the control signals in the cost function. That is, we might include a term in the cost function that is

proportional to the sum of the squared control signals as in [49], [50]. For a system with K actuators and M error sensors, we define the new cost function as

$$\xi(n) = \sum_{m=1}^{M} e_m{}^2(n) + \alpha \sum_{k=1}^{K} y_k{}^2(n), \tag{5.53}$$

where

$$y_k(n) = \sum_{m=1}^{M} w_{km}(n) * x_m(n), \; k=1,2, \#, K$$

and $\alpha$ is a real, positive weighting coefficient used to balance the control error (first term) and the control effort (second term). Following the procedure of the development for the gradient descent algorithm, the weight updating equations of the K×M adaptive filters can be derived as

$$w_{km}(n+1) = w_{km}(n) + \mu \sum_{j=1}^{M} [\hat{s}_{jk} * x_m(n)] e_j(n) - u\alpha y_k(n) x_m(n), \tag{5.54}$$

where $\hat{s}_{jk}$ is the estimated impulse response of the secondary path from the $k^{th}$ secondary resource to the $j^{th}$ error sensor. Specifically, the weight updating equations for the regular 2×2 control system are

$$w_{11}(n+1) = w_{11}(n) + \mu\{[\hat{s}_{11}(n) * x_1(n)] e_1(n) + [\hat{s}_{21}(n) * x_1(n)] e_2(n)\} - \mu\alpha y_1(n) x_1(n) \tag{5.55}$$

$$w_{21}(n+1) = w_{21}(n) + \mu\{[\hat{s}_{12}(n) * x_1(n)] e_1(n) + [\hat{s}_{22}(n) * x_1(n)] e_2(n)\} - \mu\alpha y_2(n) x_1(n) \tag{5.56}$$

$$w_{12}(n+1) = w_{12}(n) + \mu\{[\hat{s}_{11}(n) * x_2(n)] e_1(n) + [\hat{s}_{21}(n) * x_2(n)] e_2(n)\} - \mu\alpha y_1(n) x_2(n) \tag{5.57}$$

$$w_{22}(n+1) = w_{22}(n) + \mu\{[\hat{s}_{12}(n) * x_2(n)] e_1(n) + [\hat{s}_{22}(n) * x_2(n)] e_2(n)\} - \mu\alpha y_2(n) x_2(n). \tag{5.58}$$

Equations (5.55) and (5.58) are the weight updating equations of the simplified 2×2 control system except that $y_1(n)$ is now the output of $W_{11}(z)$ only and $y_2(n)$ is the

output of $W_{22}(z)$ only. The weight updating equation of the decentralized 2×2 control system are then simplified to

$$w_{11}(n+1) = w_{11}(n) + \mu[\hat{s}_{11}(n) * x_1(n)]e_1(n) - \mu\alpha y_1(n)x_1(n) \tag{5.59}$$

$$w_{22}(n+1) = w_{22}(n) + \mu[[\hat{s}_{22}(n) * x_2(n)]e_2(n) - \mu\alpha y_2(n)x_2(n)\,. \tag{5.60}$$

Figure 5.12 shows the stability improvement of the decentralized system. When the cross-coupled paths and the direct paths are the same ($[0, \quad 0.5, \quad 0.5]^T$ here), the system that only minimizes the control error diverges as shown by the upper set of curves in Figure 5.12. On the other hand, the system that minimizes both the control error and the control effort can still achieve some error reduction as shown by the lower set of curves in Figure 5.12.

The cost of the stability improvement is clearly the decrease in the error reduction. Figure 5.13 shows the difference of the error reduction at point 1 using these two cost functions when the algorithm is stable. There is always a compromise between the performance and the robustness for feedback control systems and the decision as to where we compromise must be made based on the specific requirements of the real applications.

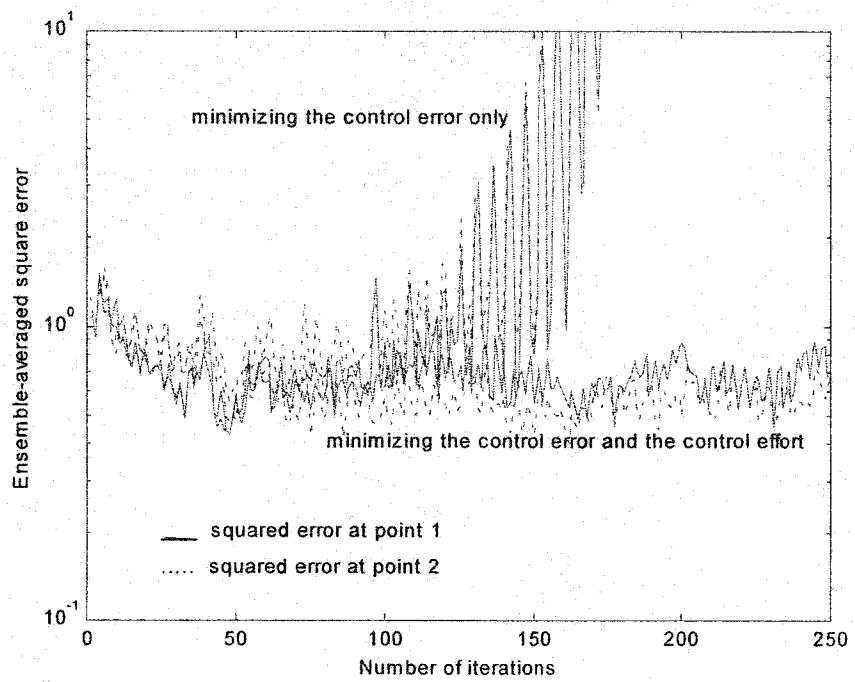



Figure 5.12 Stability improvement of the decentralized system by minimizing both the control error and the control effort ($\alpha$=*0.3*)

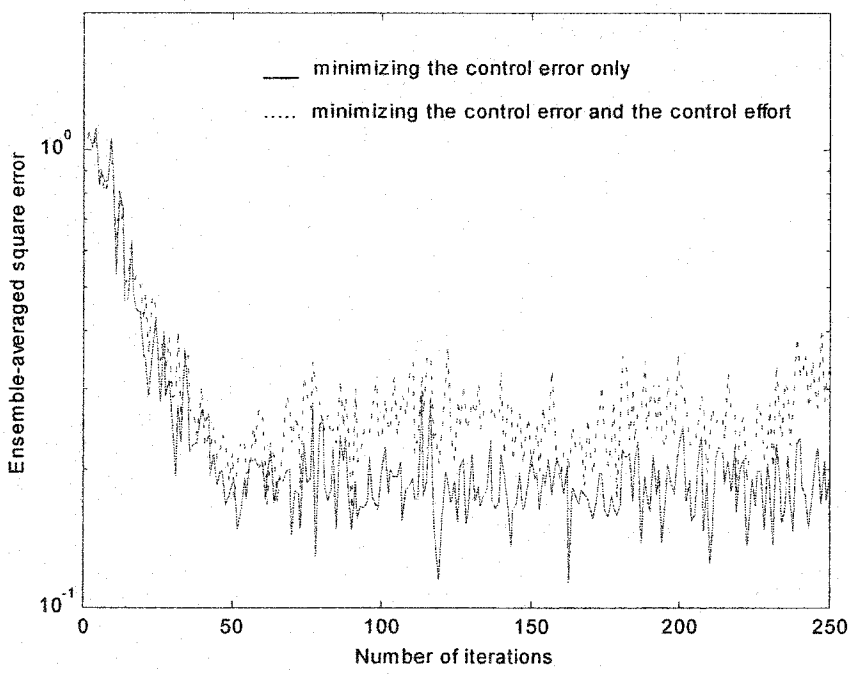



Figure 5.13 The square error at point 1 using the old cost function (the solid line) and the new cost function with $\alpha$=0.5 (the dotted line) in the steady state $\boldsymbol{s}_{11} = \boldsymbol{s}_{22} = [0, \quad 0.5, \quad -0.5]^T$ and $\boldsymbol{s}_{12} = \boldsymbol{s}_{21} = [0, \quad 0.2, \quad 0.2]^T$ )

# Chapter 6

# Summary and conclusion

This dissertation discusses the active control system and applies it to the vibration reduction of a complex mechanical structure, the hard disk drive assembly. Four problems associated with the active control system are analyzed, which are the convergence rate, the constructive interference, performance improvement and on-line identification of the secondary paths. Selective adaptation in the frequency domain is proposed to alleviate the constructive interference. A delayless sub-band algorithm is proposed to improve the convergence rate and trade off the performance from various sub-bands. Up to 10 *dB* of vibration reduction is achieved in the simulation and the real time implementation.

In Chapter 2 the basic technologies of the single-channel active control system is introduced. First, the principles and performance limitations of the feed-forward active control system and the feedback active control system are described. Then, on-line identification of the secondary path transfer and the effect of the estimate error are analyzed. The hybrid active control system is used to improve the overall performance when a reference signal is available.

Chapter 3 theoretically shows the improvement of the convergence rate by implementing the algorithm in the frequency domain. Simulations also demonstrated that the frequency domain LMS algorithm consistently achieves a faster convergence

rate than the time domain LMS algorithm for different input eigenvalue spreads. Then, this chapter explained why the modeling error due to the insufficient length of the controller or the primary disturbance itself results in the presence of constructive interference in feedback active control systems. A so-called selective adaptation in the frequency domain is proposed to alleviate the constructive interference while keeping the destructive interference that can be achieved by the active control systems. Simulation showed that the constructive interference can be alleviated by several dB in the constructive interference band with a slight degradation at the boundary band.

Chapter 4 discusses the implementation of the adaptive algorithm in the sub-band. It analyzed why the sub-band structure used in system identification or in echo cancellation cannot be directly applied to the active control system. This is because the ideal signal in the active control system is not directly available and the active control system generally cannot tolerate extra delay along the signal path. Then, a new delayless sub-band filter architecture was derived. The FXLMS implemented in the sub-band achieves better convergence and provides the flexibility to trade-off the performance from the various sub-bands. One side effect of the sub-band algorithm is the group delay associated with the analysis filter bank, which decreases the convergence region of the step size, accordingly. Compensation methods are proposed to increase the convergence region of the step size by generating a set of new sub-band error signals to update the filter coefficients. Combined structure of the frequency domain method and the sub-band decomposition technique are proposed to improve noise reduction in some sub-bands while the constructive interference occurring in other sub-bands can be alleviated at the same time. Computer simulations are performed for

feed-forward active control systems and feedback active control systems to verify the efficiency of the proposed sub-band algorithm.

Chapter 5 extends the single-channel feedback control system to the multiple-channel feedback control system in order to reduce the vibration of complex mechanical structures or the acoustic noise inside enclosures. Multiple-channel FXLMS is developed using the gradient descent method. Inter-channel coupling during the on-line identification of multiple secondary paths is analyzed in detail. Then on-line identification of multiple secondary path transfer functions using multiple independent white noise generators was discussed. We derived the optimal performances of the regular, simplified and decentralized multiple-channel feedback control systems, which are not reported in the literature. The formulas derived explicitly showed the dependence of the performance on the impulse responses of the secondary paths and the correlation coefficients of the primary disturbances. The theoretic values can be used to guide the selection of the appropriate control scheme in real applications. Finally, this chapter introduced techniques to improve the stability of the feedback control system by penalizing the control effort in the cost function.

The research conducted for this dissertation makes the following contributions:

1. Proposed the selective adaptation method in the frequency domain to alleviate the constructive interference.
2. Proposed a delayless sub-band algorithm to avoid signal path delay for the active control system.
3. Proposed a combined structure of the frequency domain method and the sub-band decomposition technique.

4. Derived the optimal performances of the feedback control system for three variants.

Further research can be conducted in the following directions:

1. Implement the active hybrid control system in real time. The vibration reduction that a feedback control system can achieve is limited. To improve the performance of the active control system, the feed-forward control scheme can be combined with the feedback scheme if a related reference signal is made available.
2. Develop a more computationally efficient structure for the combined structure shown in Figure 4.18. Since both the sub-band decomposition and orthogonal transform are essentially linear operations, it is possible to swap the order of these two operations to reduce the computational complexity.
3. Explore the possibility of using variable performance among the various sub-bands to alleviate the constructive interference using the frequency domain method only or using the sub-band decomposition technique only. There is a close relationship between the sub-band decomposition and the frequency domain implementation in that transforming an input vector $x(n)$ of length $N$ into the frequency domain can be viewed as decomposing $x(n)$ into $N$ sub-bands and down-sampling these sub-band signals by a factor of $N$. Therefore, it might be possible to achieve this goal using one technique only.
4. Analyze the effect of the errors in estimating the secondary path S(z) on the theoretic performance of the vibration reduction method. So far, only a few

papers ([15], [51]) deal with this issue and only preliminary results have been obtained.

5. Formulate the relationship between the *AR(N)* process resulting from the converged filter vector and the *AR(N)* process that models the original disturbance for a general secondary path S(z) in the feedback control system.

# References


[1] P. Lueg, Process of Silencing Sound Oscillations, US Patent No. 2043416, 1936.

[2] W. B. Cover, "Fighting noise with noise," *Noise Control,* Vol. 2, pp. 78-82,1956.

[3] S. J. Elliott and T.J. Sutton, "Performance of feedforward and feedback systems for active control," *IEEE Trans. on Speech and Audio Processing,* Vol. 4, No. 3, pp. 214-223, May 1996.

[4] S. J. Elliott and P.A. Nelson, "Active noise control," *IEEE Signal Processing Magazine*, Oct. 1993, pp.12-35.

[5] S. J. Elliott, "Active noise and vibration control," *Proceedings of the Third International Symposium on Methods and Models in Automation and Robotics,* Poland, 1996, pp. 41-59.

[6] E. F. Berkman and E. K. Bender, "Perspectives on active noise and vibration control," *Sound and Vibration*, Vol. 31, No. 1, pp. 80-94, Jan. 1997.

[7] R. Benning, M. Hodgins, and G. Zipfel, Jr., "Active control of mechanical vibrations," *Bell Labs Technical Journal,* Spring 1997, pp. 246-257;

[8] G. Diana, F. Cheli, M. Coppola, and D. Conrad, "Active control of vibrations of a metal panel by means of piezoelectric actuators and sensors," *Smart Structures and Materials 1997, Industrial and commercial applications of smart structures technologies*: 4-6 Mar. 1997, San Diego, pp.327-341.

[9] D. R. Morgan, "An analysis of multiple correlation cancellation loops with a filter in the auxiliary path," *IEEE Trans. on Acoustics, Speech and Signal Processing*

**AASP-28**, pp. 454-467, 1980.

[10] B. Widrow, D. Shur and S. Shaffer, "On adaptive inverse control," in *Proceedings of the 15th ASILOMAR Conference on Circuits, Systems and Computers*, pp.185-195, 1981.

[11] L. J. Eriksson, "Recursive algorithms for active noise control," in *Proc. Int. Symp. Active Control of Sound Vibration*, pp. 137-146, 1991.

[12] B. Widrow and S. D. Sterns, *Adaptive Signal Processing*, Englewood Cliffs, NJ: Prentice Hall, 1985

[13] S. Haykin, *Adaptive Filter Theory*, (3rd edition), Prentice Hall, 1996.

[14] S. M. Kuo and D. R. Morgan, *Active Noise Control Systems*, John Wiley & Sons, Inc., 1996.

[15] S. Snyder and C. Hansen, "The effect of transfer function estimation errors on the filtered-X LMS algorithm," *IEEE Trans. on Signal Processing*, Vol. 42, No. 4, pp. 950-953, Apr. 1994.

[16] S. Narayan, A. Peterson, and M. Narasimha, "Transform domain LMS algorithm," *IEEE Trans. on Acoust., Speech and Signal Processing*, Vol. ASSP-31, No. 3, pp. 609-615, Jun. 1983.

[17] F. Beaufays, "Transform-domain adaptive filters: an analytical approach," *IEEE Trans. on Signal Processing*, Vol. 43, No. 2, pp. 422-431, Feb. 1995.

[18] D. Marshall, W. Jenkins, and J. Murphy, "The use of orthogonal transforms for improving performance of adaptive filters," *IEEE Trans. on Circuits and Systems*, Vol. 36, No. 4, pp. 474-484, Apr. 1989.

[19] J. C. Lee and C. K. Un, "Performance of transform-domain LMS adaptive digital

filters," *IEEE Trans. on Acoust., Speech and Signal Processing,* Vol. ASSP-34, No. 3, pp. 499-510, Jun. 1986.

[20] S. Attallah, "The wavelet transform-domain LMS algorithm: a more practical approach," *IEEE Trans. on Circuit & Systems-II: Analog and Digital Signal Processing,* Vol. 47, No. 3, pp. 209-213, Mar. 2000.

[21] K. R. Rao, P. Yip, *Discrete Cosine Transform,* Academic Press, Inc., 1990.

[22] J. J. Shynk, "Frequency-Domain and Multirate Adaptive Filtering," *IEEE Signal Processing Magazine*, pp. 14-36, Jan. 1992.

[23] Longji Wang, V. DeBrunner, and L. DeBrunner, "Reducing the constructive interference by selective adaptation in the frequency domain," *ICECS 2001,* Malta, Sept., 2001, *to appear.*

[24] A. Gilloire and M. Vetterli, "Adaptive filtering in sub-bands," in *Proc. ICASSP'88*, New York, NY, pp. 1572-1575.

[25] A. Gilloire and M. Vetterli, "Adaptive filtering in subbands with critical sampling: analysis, experiments, and application to acoustic echo cancellation," *IEEE Transactions on Signal Processing,* Vol. 40, No. 8, pp. 1862-1875, Aug. 1992.

[26] K. Ashihara, K. Nishikawa and H. Kiya, "Improvement of convergence speed for subband adaptive digital filters using the multirate repeating method," in *Proc. ICASSP'95*, Detroit, MI, pp. 989-992.

[27] Y. Ono and H. Kiya, "Performance analysis of subband adaptive systems using an equivalent model," in *Proc. ICASSP'94,* Vol. 3, pp. 53-56, Adelaide, Australia.

[28] M. Courville and P. Duhamel, "Adaptive filtering in subbands using a weighted criterion," *IEEE Trans. on Signal Processing*, Vol. 46, No. 9, pp. 2359-2371, Sept.

1998.

[29] D. Morgan and J. Thi, "A delayless subband adaptive filter architecture," *IEEE Trans. on Signal Processing,* Vol. 43, No. 8, pp. 1819-1830, Aug. 1995.

[30] J. Thi and D. Morgan, "Delayless subband active noise control," in *Proc. ICASSP,* Vol. I, 1993, pp. 181-184.

[31] N. Hirayama, H. Sakai, and S. Miyagi, "Delayless subband adaptive filtering using the Hadamard transform," *IEEE Trans. on Signal Processing,* Vol. 47, No. 6, pp. 1731-1734, Jun. 1999.

[32] V. DeBrunner, L. DeBrunner and Longji Wang, "Sub-band adaptive filter architecture with delay compensation for active control," (to be published).

[33] V. DeBrunner, L. DeBrunner and Longji Wang, "A delayless sub-band structure without signal path delay," (to be published).

[34] G. Long, F. Ling, and J. Proakis, "The LMS algorithm with delayed coefficient adaptation," *IEEE Trans. Acoust., Speech, signal Processing.* Vol. 37, No. 9, pp. 1397-1405, Sept. 1989.

[35] G. Long, F. Ling, and J. Proakis, "Corrections to 'The LMS algorithm with delayed coefficient adaptation,'" *IEEE Trans. on Signal Processing*, Vol. 40, No. 1, pp. 230-232, Jan. 1992.

[36] S. Snyder and C. Hansen, "The influence of transducer transfer functions and acoustic time delays on the implementation of the LMS algorithm in active noise control systems," *J. Sound Vib.* **141**(3), pp. 409-424, 1990.

[37] I. Kim, H. Na, K. Kim, and Y. Park, "Constraint filtered-x and filtered-u least-mean-square algorithm for the active control of noise in ducts," *J. Acoust. Soc.*

*Am.*, Vol. 95, No. 6, pp. 3397-3389, Jun. 1994.

[38] S. Gay and S. Tavathia, "The fast affine projection algorithm," in *Proc. ICASSP'95*, Vol. 5, pp. 3023-3026.

[39] M. Tanaka et al., "Fast projection algorithm and its step size control," in *Proc. ICASSP'95*, Vol. 2, pp. 945-948.

[40] M. Tanaka, S. Makino, and J. Kojima, "A block exact fast affine project algorithm," *IEEE Trans. on Speech and Audio Processing,* Vol. 7, No. 1, pp. 79-86, Jan. 1999.

[41] S. Douglas, "Efficient approximate implementations of the fast affine projection algorithm using orthogonal transforms," in *Proc. ICASSP'96*, Vol. 3, pp. 1656-1659.

[42] M. Hayes, *Statistical Digital Signal Processing and Modeling*, John Wiley & Sons, Inc., 1996.

[43] S. Elliott, I. Stothers, and P. Nelson, "A multiple error LMS algorithm and its application to the active control of sound and vibration," *IEEE Trans. on Acoust., Speech and Signal Processing,* Vol. ASSP-35, No. 10, pp. 1423-1433, Oct. 1987.

[44] S. Elliott and P. Nelson, "Multiple active sound control using adaptive filtering," in *Proc. ICASSP'88*, pp. 2590-2593.

[45] S. Kuo and J. Luan, "Multiple-channel error path modeling with the inter-channel decoupling algorithm," in *Proc. Recent Advances in Active Control of Sound Vib.*, 1993, pp. 767-777.

[46] G. Newton, L. Gould, and J. Kaiser, *Analytical Design of Feedback Controls*, New York: Wiley, 1957.

[47] S. Elliott and T. Sutton, "Performance of feedforward and feedback for active control," *IEEE Trans. on Speech and Audio Processing*, Vol. 4, No. 3, pp. 214-223, May 1996.

[48] P. Grosdidier and M. Morari, "Interaction measures for systems under decentralized control," *Automatica* Vol. 22, pp. 309-319, 1986.

[49] S. Elliott, C. Boucher, and P. Nelson, "The behavior of a multiple channel active control system," *IEEE Trans. on Signal Processing*, Vol. 40, No. 5, pp. 1041-1052, May 1992.

[50] J. Minkoff, "The operation of multiple feedforward adaptive systems," *IEEE Trans. on Signal Processing*, Vol. 45, No. 12, pp. 2993-3005, Dec. 1997.

[51] C. Boucher, S. Elliot, and P. Nelson, "Effect of errors in the plant model on the performance of algorithms for adaptive feedforward control," in *Proc. Inst. Elec. Eng., pt. F,* vol. 138, pp. 313-319, 1991.

[52] S. Elliott and C. Boucher, "Interaction between multiple feedforward active control systems," *IEEE Trans. on Speech and Audio Processing*, Vol. 2, No. 4, pp. 521-530, Oct. 1994.

[53] S. Snyder and C. Hansen, "Design considerations for active noise control systems implementing the multiple input, multiple output LMS algorithm," *Journal of Sound and Vibration*, **159**(1), pp. 157-174, 1992.

[54] S. Elliott, "Optimal controllers and adaptive controllers for multichannel feedforward control of stochastic disturbances," *IEEE Trans. on Signal Processing*, Vol. 48, No. 4, pp. 1053-1060, Apr. 2000.

[55] S. Kuo and D. Vijayan, "Adaptive algorithms and experimental verification of

feedback active noise control systems," *Noise Control Eng. J.*, Vol. 42, No. 2, pp. 37-46, 1994.

[56] S. Douglas, "Adaptive filters employing partial updates," *IEEE Trans. on Circuit & Systems-II: Analog and Digital Signal Processing,* Vol. 44, No. 3, pp. 209-216, Mar. 1997.

[57] A. Gonzalez, A. Albiol, and S. Elliott, "Minimization of the maximum error signal in active control," *IEEE Trans. on Speech and Audio Processing*, Vol. 6, No. 3, pp. 268-281, May 1998.

[58] S. Douglas, "Analysis and implementation of the max-NLMS adaptive filter," in *Proceedings of ASILOMAR-29*, pp.659-663, 1996.

[59] M. Rupp, "Saving complexity of modified filtered-X-LMS and delayed update LMS algorithms," *IEEE Trans. on Circuit & Systems-II: Analog and Digital Signal Processing,* Vol. 44, No. 1, pp. 57-60, Jan. 1997.

[60] M. Rupp and A. Sayed, "Modified FxLMS algorithms with improved convergence performance," in *Proceedings of ASILOMAR-29*, pp.1255-1259, 1996.

[61] R. Poltmann, "Conversion of the delayed LMS algorithm into the LMS algorithm," *IEEE Processing Letters,* Vol. 2, No. 12, pp. 223, Dec. 1995.

[62] P. Darlington and S. Elliott, "Synchronous adaptive filters with delayed coefficient adaption," in *Proc. ICASSP'88*, pp. 2586-2589.

[63] Y. Yang, N. Cho, S. Lee, "On the performance analysis and applications of the subband adaptive digital filter," *Signal Processing 41*, pp. 295-307, 1995.

[64] M. Petraglia and S. Mitra, "Adaptive FIR filter structure based on the generalized subband decomposition of FIR filters," *IEEE Trans. on Circuit & Systems-II:*

*Analog and Digital Signal Processing,* Vol. 40, No. 6, pp. 354-362, Jun. 1993.

[65] S. Mitra, A. Mahalanobis, and T. Saramaki, "A generalized structure subband decomposition of FIR filters and its application in efficient FIR filter design and implementation," *IEEE Trans. on Circuit & Systems-II: Analog and Digital Signal Processing,* Vol. 40, No. 6, pp. 363-374, Jun. 1993.

[66] A. Mahalanobis, S. Song, S. Mitra, and M. Petraglia, "Adaptive FIR filters based on structure subband decomposition for system identification problems," *IEEE Trans. on Circuit & Systems-II: Analog and Digital Signal Processing,* Vol. 40, No. 6, pp. 375-381, Jun. 1993.

[67] P. Vaidyanathan, "Multirate digital filters, filter banks, polyphase networks, and applications: a tutorial," *Proceedings of the IEEE*, Vol. 78, No. 1, pp. 56-93, Jan., 1990.

[68] M. Halfin and G. Coutu, "Adaptive frequency selective filters," in *Proceedings of ASILOMAR-27*, pp.1579-1283, 1994.

[69] P. Feintuch, N. Bershad, and A. Lo, "A frequency domain model for 'filtered' LMS algorithms-stability analysis, design, and elimination of the training mode," *IEEE Trans. on Signal Processing*, Vol. 41, No. 4, pp. 1518-1531, Apr. 1993.

[70] A. Wang and W. Ren, "Convergence analysis of the multi-variable filter-X LMS algorithm with application to active noise control," *IEEE Trans. on Signal Processing*, Vol. 47, No. 4, pp. 1166-1169, Apr. 1999.

[71] E. Bjarnason, "Analysis of the filtered-X LMS algorithm," *IEEE Trans. on Speech and Audio Processing*, Vol. 3, No. 6, pp. 504-514, Nov. 1995.

[72] S. Douglas and W. Pan, "Exact expectation analysis of the LMS adaptive filter,"

*IEEE Trans. on Signal Processing*, Vol. 43, No. 12, pp. 2863-2871, Dec. 1995.

[73] B. Widrow, J. Glover, Jr., J. Mccool, J. Kaunitz, C. Williams, R. Hearn, J. Zeidler, E. Dong, E. Dong, Jr., R. Goodlin, "Adaptive noise canceling: principles and applications," *Proceedings of the IEEE*, Vol. 63, No. 12, pp. 1692-1716, Dec., 1975.

[74] G. Glentis, "Efficient least squares adaptive algorithms for FIR transversal filtering," *IEEE Signal Processing Magazine*, pp. 13-41, Jul. 1999.

# Appendix A

# Experimental environment

Appendix A introduces the main equipment in the experimental system and gives the technical specifications.

## A.1 M44

The M44 from Innovative Integration, Inc. (http://www.innovative-dsp.com) is employed as the processor in the active control system. The M44 is a PCI bus-based, flexible I/O engine featuring a high-performance DSP and dual OMNIBUS module I/O expansion sites. It employs a TMS320C44 32-bit floating-point DSP as a data movement/data processing engine capable of up to 60 MFLOPS/30 MIPS. On-chip peripherals include two 32-bit counter/timers, six powerful DMA channels, 8 Kbytes of dual-access SRAM, four bi-directional comm.-ports and a prioritized interrupt controller. Table A.1 summaries the technical specifications.

Table A.1 Technical specifications of the M44

| | |
|---|---|
| Digital Signal Processor | TI TMS320C44 275 MOPS 32-bit floating-point DSP optimized instruction set for DSP. |
| Memory | 32M×32 total range. Expandable on-board to 512K×32 global, 128K×32 local. |
| Debug Port | JTAG 1149.1 port for emulation of multiple 'C44's. Supports C/Assembly source level debugging with Code Hammer. |
| Host PC Interface | PCI bus master/slave 32-bit 5V; consumes 256 bytes of host I/O space, 1 Mbyte host memory space, 1 interrupt. |
| Comm. Port Connections | Two buffered comm. ports for system expansion. Two comm. port to OMNIBUS module I/O slots. |
| Digital I/O | 32-bit TTL input, output or bi-directional with real back, 64 mA sink/32 mA source drive capacity. |
| Timers/Counters | One direct digital synthesizer(DDS) 0.02 Hz resolution. Three 16-bit timers driven by DDS. |
| Connectors | Two DB 15 female for I/O; IDC 80 for 4XBUS expansion. |

## A.2 A4D4

An A4D4 OMNIBUS module is employed to provide the A/D and the D/A channels. The A4D4 accommodates 4 analog input channels and 4 D/A channels. The four analog input channels on the A4D4 module are successive approximation type A/D converters, which allows for low data latency critical in control applications and multiple channel configurations. Each input and output channel is calibrated for gain and offset errors allowing accurate measurements for a variety of applications. Table A.2 summaries the key specifications.

Table A.2 Technical specifications of the A4D4

| | |
|---|---|
| Bus Type | Compatible with all OMNIBUS Innovative products, 32-bit. Consume one interrupt to host DSP. |
| A/D Converters | Analog devices AD976AA. Success approximation architecture for low data latency. |
| Resolution | 16-bit |
| Setting Time | 5 us (no filtering) @ 10 V step to 0.0008% |
| Update Rate | 200 kHz |
| Analog Input range | +/- 10 V |
| Input Type | Differential |
| Programmable Gain | 1,2 ,4,8 |
| Conversion Trigger Sources | DSP, timers or externally triggered. |
| Interface to DSP | Memory-mapped 32-bit result returned for each A/D pair. |
| D/A converters | Analog devices AD7846. Each D/A channel has independent filtering, gain and trims. |
| Resolution | 16-bit |
| Setting Time | 7 us (unfiltered) to 0.003% |
| Output Range | +/- 10 V |
| Interface to DSP | Memory-mapped, 16-bit interface to DSP. |

## A.3 PCB 353B15 accelerometer

Two PCB 353B15 piezoelectric accelerometers from PCB Piezotronics Inc. (http://www.pcb.com) are used as the residual error sensors in the experimental system.

These are powered by a constant-current signal conditioner and have fixed voltage sensitivity. Table A.3 provides the primary performance characteristics of the PCB 353B15.

Table A.3 Main features of the PCB 353B15 accelerometer

| | |
|---|---|
| Frequency Range (±5%) | 1 to 10000 Hz |
| Voltage Sensitivity | 10.27 mV/g |
| Resonant Frequency | 75.5 kHz |
| Amplitude Range | -500 pk/500 pk g |
| Resolution | 0.01 g |
| Constant Current Excitation | 2 to 20 mA |
| Output Impedance | <100 ohms |
| Temperature Range | -65 to +250 F |
| Weight | 0.07 oz (2 gram) |

## A.4 PCB 713A01 patch actuator

Two PCB 713 A01 patch actuators are used as the actuators to generate the canceling vibration in the active control system. The technical specifications of the PCB 713A01 patch actuator is summarized in Table A.4.

Table A.4 Main features of PCB 713A01 patch actuator

| | |
|---|---|
| Frequency Range | 0~50000 Hz |
| Maximum Voltage | +200 pk/-100pk volt |
| Piezoceramic Type | PZT 5A |
| Capacitance (at constant stress) | 32 nF |
| Clamped Force | 0.047 lb/V [0.208N/V] |
| Free Expansion | 1.335exp(-6) in/V [3.4exp(-5) mm/V] |
| Ceramic thickness | 0.023 in [0.0584 mm] |
| Weight | 0.49 oz [14 gram] |
| Dimensions (L×W×T) | 109 x 21.3 x 1.27 mm |
| Operating Temperature | -13~185 F |

## A.5 482A04 line power supply

A 482A04 line power supply or called signal conditioner (four channel) is used to power the accelerometers. It contains four constant current circuits and provides

constant current excitation to the built-in transducer amplifier that decouples the signal from the DC bias voltage. Table A.5 gives the specifications of 482A04 line power supply.

Table A.5 Specifications of the 482A04 line power supply

| | |
|---|---|
| Channels | 4 |
| Supply Voltage | +24 V/Channel |
| ICP Sensor Excitation Current | 2-20 mA/Channel |
| Time Constant | 10 sec |
| Low Frequency Response | <0.1 Hz |
| High Frequency Response | >1000 kHz |
| DC Offset (maximum) | <30 mV |
| Noise Broadband (1 Hz-10 kHz) | <7.58 μV |
| Voltage Gain (all outputs) | 1 ±1% |
| Power Required (50-400 Hz) | 115 ±10% VAC/0.12 A |

## A.6 790A01 power amplifier

Two 790A01 power amplifiers are employed to drive the two 713A01 patch actuators in the experimental system. The 790A01 power amplifier can generate an output of up to ±200 V peak at 100 mA peak and features adjustable gain for flexibility. Table A.6 shows the specifications of the 790A01 power amplifier.

Table A.6 Specifications of the 790A01 power amplifier

| | |
|---|---|
| Channels | 1 |
| Output Voltage Range | 200 ±2.5% V pk |
| Output Current | ±100 ±5% mA pk |
| Calibration | Internal |
| Calibration Voltage | 1.00 ±2% VDC |
| Voltage Gain | 5 to 50 adjustable |
| Input Impedance | 10000 ±10% ohms |
| Maximum Capacitive Loading | 100-1000 nF |
| Power Requirements | 120/220 VAC, 60/50 Hz (selectable) |
| Weight | 7.5 lb |

# Appendix B

# Efficient Implementation of the DCT

The discrete cosine transform of an N-point sequence $x(n), n = 0,1,...,N-1$ is defined as [21]

$$X_0 = \frac{1}{\sqrt{N}} \sum_{n=0}^{N-1} x(n)$$

$$X_k = \sqrt{\frac{2}{N}} \sum_{n=0}^{N-1} x(n) \cos \frac{\pi(2n+1)k}{2N}, k = 1,2,...,N-1 \quad \text{(B.1)}$$

Without considering the gain constants, the $k^{th}$ DCT coefficient can be viewed as the output of an N-point digital filter, whose impulse response is

$$h_k(n) = \cos \frac{\pi(2n+1)k}{2N}, n = 0,1,...,N-1 \quad \text{(B.2)}$$

The corresponding z transform is

$$H_k(z) = \sum_{n=0}^{N-1} z^{-n} \cos \frac{\pi(2n+1)k}{2N} \quad \text{(B.3)}$$

Using the finite geometric sum relationship

$$\sum_{n=0}^{N-1} x^n = \frac{1-x^N}{1-x}, x \le 1 \quad \text{(B.4)}$$

and the Euler identity

$$\cos(x) = \frac{1}{2}(e^{-jx} + e^{jx}) \quad \text{(B.5)}$$

Equation (B.3) can be simplified to

$$H_k(z) = \frac{1}{2}[\sum_{n=0}^{N-1} z^{-n} e^{-j\frac{\pi(2n+1)k}{2N}} + \sum_{n=0}^{N-1} z^{-n} e^{j\frac{\pi(2n+1)k}{2N}}]$$

$$= \frac{1}{2}[e^{-j\frac{\pi k}{2N}} \sum_{n=0}^{N-1} (z^{-1} e^{-j\frac{\pi nk}{N}})^n + e^{j\frac{\pi k}{2N}} \sum_{n=0}^{N-1} (z^{-1} e^{j\frac{\pi nk}{N}})^n]$$

$$= \frac{1}{2} e^{-j\frac{\pi k}{2N}} \frac{1-(z^{-1}e^{-j\frac{\pi k}{N}})^N}{1-z^{-1}e^{-j\frac{\pi k}{N}}} + \frac{1}{2} e^{j\frac{\pi k}{2N}} \frac{1-(z^{-1}e^{j\frac{\pi k}{N}})^N}{1-z^{-1}e^{j\frac{\pi k}{N}}}$$

$$= \frac{1}{2} \frac{e^{-j\frac{\pi k}{2N}} - z^{-N} e^{-j\frac{\pi k}{2N}} e^{-j\pi k}}{1-z^{-1}e^{-j\frac{\pi k}{N}}} + \frac{1}{2} \frac{e^{j\frac{\pi k}{2N}} - z^{-N} e^{j\frac{\pi k}{2N}} e^{j\pi k}}{1-z^{-1}e^{j\frac{\pi k}{N}}}$$

$$= \frac{1}{2} \frac{[e^{-j\frac{\pi k}{2N}} - z^{-N} e^{-j(\frac{1}{2N}+1)\pi k}](1-z^{-1}e^{j\frac{\pi k}{N}}) + [e^{j\frac{\pi k}{2N}} - z^{-N} e^{j(\frac{1}{2N}+1)\pi k}](1-z^{-1}e^{-j\frac{\pi k}{N}})}{(1-z^{-1}e^{-j\frac{\pi k}{N}})(1-z^{-1}e^{j\frac{\pi k}{N}})}$$

$$= \frac{1}{2} \frac{2\cos\frac{\pi k}{2N} - 2z^{-1}\cos(\frac{1}{N}-\frac{1}{2N})\pi k - 2z^{-N}\cos(\frac{1}{2N}+1)\pi k + 2z^{-(N+1)}\cos(\frac{1}{2N}-1)\pi k}{1-2z^{-1}\cos\frac{\pi k}{N}+z^{-2}}$$

$$= \frac{\cos\frac{\pi k}{2N} - z^{-1}\cos\frac{\pi k}{2N} - z^{-N}\cos\frac{\pi k}{2N}\cos\pi k + z^{-(N+1)}\cos\frac{\pi k}{2N}\cos\pi k}{1-2z^{-1}\cos\frac{\pi k}{N}+z^{-2}}$$

$$= \cos\frac{\pi k}{2N} \frac{(1-z^{-1}) - (-1)^k[z^{-N} - z^{-(N+1)}]}{1-2\cos\frac{\pi k}{N}z^{-1}+z^{-2}} \qquad \text{(B.6)}$$

Including the gain constants in (B.1), we get

$$H_k(z) = c_k \frac{(1-z^{-1}) - (-1)^k[z^{-N} - z^{-(N+1)}]}{1-a_k z^{-1}+z^{-2}}$$

where

$$a_k = 2, c_k = \frac{1}{\sqrt{N}}, k = 0$$
$$a_k = 2\cos\frac{\pi k}{N}, c_k = \sqrt{\frac{2}{N}}\cos\frac{\pi k}{2N}, k = 1,2,...,N-1 \quad \text{(B.7)}$$

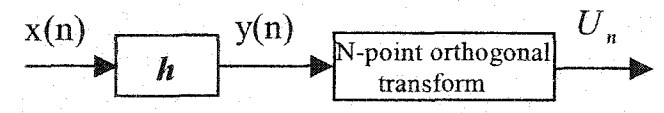
The $a_k$ and $c_k$ can be calculated in advance. Doing so, only *2N* multiplications are required for the N-point DCT. Consequently, only *4N+1* multiplications are required to implement the LMS in the frequency domain for each sample.

# Appendix C

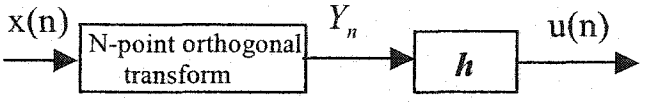
## Proof of the non-equivalency of the direct swap

Appendix C shows that the sub-band decomposition and the orthogonal transform in Figure 4.18 cannot be swapped without further change.

Figure C.1(a) shows the structure where the linear filtering (sub-band decomposition) comes first and Figure C.1(b) shows the structure where the orthogonal transform comes first.




(a)




(b)

Figure C.1 Swapped order of the sub-band decomposition and orthogonal transform.

Let us assume that the linear filter ***h(n)*** is an FIR filter with order $N$ and the orthogonal transform is also of order $N$ with the coefficients as

$$T = \begin{bmatrix} g_{0,0} & \cdots & g_{0,N-1} \\ \vdots & \ddots & \vdots \\ g_{N-1,0} & \cdots & g_{N-1,N-1} \end{bmatrix}. \qquad \text{(C.1)}$$

For the structure shown in Figure C.1(a),

$$y(n) = \sum_{i=0}^{N-1} h(i)x(n-i)\,. \tag{C.2}$$

Then, the output vector of length $N$ is

$$\begin{bmatrix} U_n(0) \\ \vdots \\ U_n(N-1) \end{bmatrix} = \begin{bmatrix} g_{0,0} & \cdots & g_{0,N-1} \\ \vdots & \ddots & \vdots \\ g_{N-1,0} & \cdots & g_{N-1,N-1} \end{bmatrix} \begin{bmatrix} y(n) \\ \vdots \\ y(n-N+1) \end{bmatrix}, \tag{C.3}$$

where

$$U_n(k) = \sum_{i=0}^{N-1} g_{k,i}\, y(n-i) = \sum_{i=0}^{N-1}\sum_{j=0}^{N-1} g_{k,i}\, h(j)x(n-i-j), \quad k = 0,1,\ldots,N-1\,. \tag{C.4}$$

For the structure shown in Figure C.1(b), we have

$$\begin{bmatrix} Y_n(0) \\ \vdots \\ Y_n(N-1) \end{bmatrix} = \begin{bmatrix} g_{0,0} & \cdots & g_{0,N-1} \\ \vdots & \ddots & \vdots \\ g_{N-1,0} & \cdots & g_{N-1,N-1} \end{bmatrix} \begin{bmatrix} x(n) \\ \vdots \\ x(n-N+1) \end{bmatrix}, \tag{C.5}$$

and the output vector of length $N$ is

$$[u(n)\, u(n-1) \cdots u(n-N+1)]^T, \tag{C.6}$$

where

$$u(n) = \sum_{i=0}^{N-1} h(i)Y_n(i) = \sum_{i=0}^{N-1}\sum_{j=0}^{N-1} h(i)g_{i,j}x(n-j)\,. \tag{C.7}$$

The output vectors of these two structures as given in Equations (C.3) and (C.6) are different. Therefore, the order of the sub-band decomposition and the orthogonal transform in Figure 4.18 cannot be commuted directly.

# Vita

Longji Wang was born in Sichuan, China on October 8, 1964. He received the B.S. and M.S. degrees in computer science from the Northwestern Polytechnical University, China, in 1985 and 1988, respectively and the M.S. and Ph.D. degrees in electrical engineering from the University of Oklahoma in 1999 and 2001, respectively.

From 1988 to 1996 he was with the Department of Automatic Control, Northwestern Polytechnical University, as an assistant professor and lecturer. He was with the School of Electrical and Computer Engineering at the University of Oklahoma as a visiting scholar from 1996 to 1997. During 1997 to 2001 he was a research assistant in the School of Electrical and Computer Engineering at the University of Oklahoma, where he was awarded as the outstanding graduate student in 2000.

His research interests include image/video processing and reliable transmission, adaptive filtering, active noise control, and computer networking.